Clinical applications of the Medipix detector

A thesis submitted in partial fulfilment of the requirements for the degree of Doctor of Philosophy in Medical Physics

By

ANAS ABDULHAMID M. SEDAYO

Department of Physics and Astronomy

University of Canterbury

Christchurch, New Zealand

2012

Contents

List of Figures

List of Tables

Acknowledgment

Pursuing a PhD. Project is a both painful and enjoyable experience. It's just like climbing a high peak, step by step, accompanied with bitterness, hardships, frustrations, encouragements and trust and with so many people's kind help. When I find myself at the top enjoying the beautiful scenery, I realized that it was in fact teamwork that got me there. Though it will not be enough to express my gratitude in words to all those people who helped me, I would like to give my many thanks to all these people.

First of all, I would like to give my sincere thanks to my honorific supervisor, Prof. Philip Butler, University of Canterbury, who accepted me as his PhD student without any hesitation when I presented him my research proposal. Thereafter, he offered me so much advice, patiently supervising me and always guiding me in the right direction. I have learned a lot from him, without his help I could not have finished my thesis successfully.

I would like to express the profound gratitude to Assoc. Prof. Dr. Lou Reinisch, as he was my supervisor before he resigned from the University of Canterbury, to become Head of Physical and Earth Sciences department, Jacksonville State University for his kind supervision, cooperation, illuminating discussions, stimulating suggestions, and for his unique exertion in carrying out this research work at the beginning of my research.

I would like to express my gratitude to Prof. Samir Abdul-Majid, the originator of the project and for the many ideas and methods upon which this work was based. Also, I would like to express my appreciation for his assistant supervision.

I would like to convey my thanks to Dr. Anthony Butler for his great support and help.

I would like to convey my thanks to Dr. Stephen Bell for his great help in editing and review my thesis.

Special thanks go to the former MARS lab managers, Alexandra Butler, Angela Moore and present MARS research facilitator, Peter Hilton for their great help and coordinating research activities. Thanks to Dr. Judy Mohr for her knowledge sharing. I also would like to convey thanks to my colleagues, Robert Doesburg, Raja Aamir Mallal, Rafidah Zainon, Syen Jien Nik, Michael Walsh and Niels de Ruiter for an inspiring and friendly environment.

I would like to convey my thanks to the members of the department of Physics and Astronomy, in particular MARS group.

The research has been funded under governmental scholarship from Saudi Arabia, ministry of health and I am grateful for this generous support from my country. Also, I'm grateful for the support from the Saudi cultural office in New Zealand and Australia which insured a very good educational environment during the period of study

I would like to dedicate this thesis to my beloved dad Abdulhamid Sedayo and mum Shefaa Erkesos for warm encouragement all the time to continue my postgraduate study and support me earlier in my life, all my wish they will receive my news and they feel happy about me. I would like to express my deepest gratitude and love to my wife Dr. Hanadi Katouah for being patient with me, providing entertainment and caring of me. My PhD would not have been possible

without her support. I also want to give my deepest love and thanks to my beloved children Eyad Sedayo, Lamer Sedayo and Obai Sedayo for giving me inspiration, making me happy, and accompanying me when I was under tremendous pressure. I also want to thank my brothers and sisters for always embracing me and believing that I could do it. I also express love and thanks to my family in law for encouraging me and giving me a moral support through my PhD. Lastly, I have been incredibly fortunate to be surrounded with such an amazing family.

Abstract

In this thesis a recently developed energy resolving x-ray detector (Medipix) is used to investigate potential medical applications of spectral x-ray imaging. Computed Tomography (CT) is one of the most important medical imaging modalities. Recent developments in CT techniques include dual-energy CT, where images are taken with two different x-ray spectra by either using two x-ray tubes operated at different voltages, or modulating the operating voltage of a single tube. These techniques provide spectral information in the CT dataset but are limited to what can be achieved by manipulating the x-ray source, since the detectors used in current CT systems are unable to provide spectral information about the detected x-rays.

A preliminary investigation of the use of the Medipix detectors for two different medical applications is presented. The first, applications is imaging of blood vessels for diagnosis of vascular diseases, and the second, characterising and measuring the energy dependence of x-ray attenuation in fat and liver tissue using the Medipix2 detector. This second investigation is part of work towards (eventually) quantifying the fat content of liver tissue *in vivo*, which is important for the early diagnosis of fatty liver disease.

While an early attempt to identify iron fluorescence x-rays in a Monte-Carlo simulation of blood vessel x-ray image was not successful, the potential for improving image contrast using the changes in x-ray attenuation at the iodine k-edge iodine have been investigated in a series of further simulations and appears to be feasible.

The potential use of spectral imaging to differentiate and quantify tissues without the need for added contrast material has been investigated by using a Medipix2 detector to measure the energy dependence of x-ray absorption in fat and liver tissue. The results of this experimental work show significant differences in x-ray attenuation between these two tissues that suggest this form of spectral imaging may be useful in practice.

Abbreviations

2D	*Two-dimensional*
3D	*Three-dimensional*
ASIC	*Application Specific Integrated Circuit*
Beamdp	*Graphical Plotting Module*
BH	*Bremsstrahlung*
CdTl	*Cadmium Telluride*
CERN	*European Organization for Nuclear Research*
CM	*Component Module*
CMOS	*Complementary Metal Oxide Semiconductor*
CPU	*Computer Processor Unit*
CT	*Computed Tomography*
DEA	*Dual Energy Angiography*
DECT	*Dual Energy CT*
DES	*Dual Energy Subtraction*
DICOM	*Digital Imaging and Communications in Medicine*
DSA	*Digital Subtraction Angiography*
ECUT	*Global electron cut-off energy-*
EGS	*Energy Gamma Shower*
fps	*Frames Per Second*
GaAs	*Gallium Arsenide*
GD	*Gadolinium*
GI	*Gastrointestinal*
GUI	*Graphical User Interface*
HU	*Hounsfield Unit*
HVL	*Half Value Layer*
kV	*Kilovoltage*
kVp	*Peak Kilovoltage*
MARS	*The Medipix All Resolution CT System*
Mo	*Molybdenum*
MRA	*Magnetic Resonance Angiography*

MRI	*Magnetic Resonance Imaging*
MUROS	*Medipix Readout Unit*
NAFLD	*Non-Alcoholic Fatty Liver Disease, Non-alcoholic fatty liver disease*
NASH	*Non-Alcoholic Steatohepatitis*
PCA	*Principle Component Analysis*
PCUT	*the Global Cut-off Energy for Photon Transport*
PI	*plane phantom with Iodine*
PP	*plane phantom*
PS	*Plane Spectra*
PWI	*Phantom with Iodine*
Rh	*Rhodium*
ROI	*Region of Interest*
Si	*Silicon*
THH	*High Threshold*
THL	*Low Threshold*

Chapter 1

1 Introduction

1.1 Overview

The Medipix detector is a new photon counting x-ray detector with energy discrimination capabilities. Developed in CERN with collaborating partners, the Medipix detector provides the potential to acquire spectral information in x-ray imaging applications. The Medipix All Resolution CT System (MARS-CT) is a compact CT system developed for preclinical research of spectral CT imaging applications using small biological samples (e.g. mouse, rat, and excised tissue). This thesis investigates clinical applications of x-ray imaging that may be improved in the future by incorporating spectral information of the detected x-rays.

Two potential clinical applications of spectral CT imaging are investigated. The first application, angiography, was studied theoretically using the Monte Carlo method to simulate the x-ray tube, a blood vessel and the detector. Simulated x-ray spectra from several different simulations were analysed to gain insight into how the various parameters of the imaging system affect the spectroscopic information collected in practical applications.

Further experimental investigations using the MARS CT system were carried out to study spectral imaging of non-alcoholic fatty liver disease (NAFLD). The techniques used in this study include the imaging protocol and the analysis methods. These investigations show the utility of the MARS-CT system for

preclinical spectral CT imaging and demonstrate the potential for this new scanner to lead to advances in medical imaging technology.

1.2 X-ray imaging

Conrad Wilhelm Roentgen discovered x-rays on the 8th of November 1895. A few weeks later, he published an image of his wife's hand, which is now famous as the first medical x-ray image. X-ray imaging was rapidly introduced into medical applications and is still important today (Roentgen, 1895).

Over recent decades, advances in computer technology have facilitated the development of new methods for x-ray imaging such as computed tomography (CT). CT was invented by Hounsfield in 1973 (Hounsfield, 1973, Bates and Peters, 1971, Hounsfield, 1980). In CT, 2D projections are acquired from different angles and using the inverse Radon transform, this dataset is transformed to obtain a 3D representation of the object. It is common practice to arrange the reconstructed data as images representing axial slices through the object.

In spite of the advances in CT, the x-ray detectors in current use are of the same basic type (integrated response radiation detector) as early CT systems, suggesting that improvements in detector technology may provide the best opportunities for revolutionary developments in CT imaging applications. Our research focuses on a new type of detector, the photon processing Medipix chip. In contrast to the commonly used integrating detector, where the registered signal is proportional to the deposited energy, Medipix is capable of processing each incoming x-ray photon individually, and allows the user to specify an energy window within which x-ray photons are counted. The latest version of the Medipix chip

(Medipix3RX: 3.x)[1] provides multiple counters so that up to seven energy ranges may be recorded in a single x-ray exposure. This energy information, which is not available from conventional detectors, enables the development of a new imaging mode: Spectral x-ray imaging.

1.3 The Medipix Detector and MARS-CT

The development of photon counting detectors such as the Medipix detector is enabling a new exciting evolution in CT technique. The photon counting detectors offer a lot of interesting advantages that are attractive for medical applications. These advantages include high efficiency, improved detectability of details (high spatial resolution), and the capability for discriminating between materials and different types of tissues.

The Medipix detectors are hybrid pixel detectors developed at European Organisation for Nuclear Research (CERN) (Medipix, 2011) in collaboration with other research groups that includes our research group based at the University of Canterbury, and University of Otago Canterbury. This detector known as hybrid because it consists of a semiconductor sensor layer bump-bonded to a readout application specific integrated circuit (ASIC) with the same pixel size. Bump bonding is the process that connects each ASIC pixel to the semiconductor layer. The basic operating principle of Medipix detectors is energy conversion, energy discrimination, processing and counting each single incident x-ray photon.

The hybrid implementation of the Medipix detector provides advantages over scintillation or gaseous detectors that include, high speed due to thousands of

[1] Medipix3RX was not yet available at the time the research in this thesis was carried out, although at the time of writing early prototypes are available to our research group.

counting circuits working parallel, individually adjustably pixel electronics and the capability to optimise the sensor material and the electronic layer independently.

The Medipix detector operates by directly converting individual x-ray photons into an ionisation cloud of electron and holes within the semi-conductor sensor. A depletion layer free from charge carriers is created in the detection layer by the reverse bias voltage applied to the semiconductor. Each incoming x-ray interacts with the sensor layer primarily through the photoelectric effect depositing its energy with an electron. This photo-electron deposits large kinetic energy through the creation of many electron-hole pair its path, which due to the applied electric field drift towards the anode or cathode where their charge is measured by the underlying ASIC layer and counted if above a pre-set threshold.

There are three different materials currently available for bump bonding on to the Medipix ASIC: Silicon (Si), Gallium arsenide (GaAs) and Cadmium Telluride (CdTe). The physical characteristics of these three semiconductor materials are very important to CT imaging applications because the energy dependent x-ray absorption coefficients of the material determine its intrinsic photon detection efficiency. This in turn influences the choice of x-ray source parameters and the energy range that can be imaged.

Silicon is chosen as a sensor material for its uniformity and availability but it has modest quantum efficiency up to around 35 keV. These characteristics allow hybrid detectors using a Si sensor layer to be used for preclinical imaging of soft tissues. GaAs at the same thickness has a higher absorption cross-section (probability), which makes it a reasonable choice for applications using x-ray

energies up to around 50 keV such as mammography. For detection of higher energy x-rays (up to 120 keV) high–Z materials such as CdTe are preferred as these materials have high quantum detection efficiency in this energy range (Mitschke, 2006).

1.4 Imaging vascular disease

In the 113 years since the discovery of x-rays, x-ray imaging has been a very important tool for medicine. An example is cardiovascular angiography where blood vessels are imaged, usually by fluoroscopy, while being infused with an iodine-based contrast agent. It is highly desirable to increase the image contrast of the blood vessels relative to the surrounding tissues so as to form a well-defined image. The x-ray images obtained show details of the blood vessel morphology that the clinician uses in diagnosis and treatment planning to look for signs of occlusion or stenosis in the blood vessels in order to make decisions for patient treatment (Santos *et al.*, 2001).

Typically, angiography is performed by injecting iodine contrast medium using a long catheter inserted into an artery, inserting the catheter in the correct position can take several minutes. After catheter insertion, several radiological images are acquired during the period of contrast injection. Small vessels require a high concentration of the contrast media. If the contrast media is injected into the veins, the procedure will be less invasive. However, due to higher blood flow, the concentration of contrast medium close to the injection site will be more dilute, and a higher x-ray exposure is required (Bae, 2010).

Angiography is one of the most invasive diagnostic techniques due to both the required contrast medium and the lengthy and numerous x-ray exposures. Dual energy angiography (DEA) is a technique used to improve image contrast (Baldazzi *et al.*, 2001b). The patient is imaged twice with two different energy spectra, obtained by applying a different x-ray tube voltage for each exposure. A category within this technology is k-edge subtraction imaging. Two energy spectra are chosen so one spectrum has a peak energy below the k-edge of the iodine contrast medium, and the other has a peak energy just above the k-edge. The angiogram image is obtained by subtraction imaging using these two images at the iodine k-edge.

Another common technique to improve visual contrast is digital subtraction angiography (DSA). In DSA, a "mask" image is acquired before the infusion of the iodine contrast agent (Mia *et al.*, 2002). This is subsequently subtracted from images with iodine contrast. In this way, the appearance of blood vessels is enhanced. However, the DSA technique may introduce artefacts that arise due to movement of the patient between the time the mask is acquired and the time the contrast images are acquired. Therefore, DSA is not usually used in coronary angiography as the coronary arteries are in constant motion due to the heart activity (Baldazzi *et al.*, 2001b).

Yet another technique to improve image contrast and differentiate better between the absorbing elements compositions is dual energy subtraction (DES). In this technique, the subject is imaged twice with two different x-ray energy spectra, which are obtained by applying different combinations of x-ray tube voltage, tube anode material, and beam filtering. A sub-category within the DES technique is

k-edge subtraction imaging. Where, the two x-ray spectra are chosen so that one spectrum has its peak energy below the iodine k-edge energy, and the peak energy of the other spectrum just above the k-edge energy. However, the time to alternate between the two x-ray beams is relatively long and consequently, does not allow for motion-artefact free image subtraction. Additionally, the two exposures required, doubles the radiation dose to the patient. Consequently, this technique is not suitable for cardiac angiography with conventional x-ray sources.

1.5 Non-alcoholic Fatty Liver Disease

Non-alcoholic Fatty Liver Disease (NAFLD) has become the most common form of liver disease in western communities, affecting an estimated 17-33% of American adults to varying degrees, (Farrell and Larter, 2006). Primary NAFLD is the liver component of the "metabolic syndrome", which is a collection of diseases associated with obesity (Lall *et al.*, 2008). The clinical spectrum of NAFLD ranges from simple fatty liver or steatosis to non-alcoholic steatohepatitis (NASH, which is fatty liver with inflammation and evidence of hepatocyte damage), cirrhosis, and hepatocellular carcinoma or liver failure (Farrell and Larter, 2006). Assessing the extent of hepatosteatosis is important to diagnosing and assessing prognosis and progression of the disease in patients.

Study of fatty liver NAFLD is traditionally diagnosed by invasive liver biopsy, with findings of macro-vesicular fat (Lall *et al.*, 2008). Although non-invasive techniques such as ultrasonography (USA), computed tomography (CT), dual energy CT (DECT), and magnetic resonance imaging (MRI) may be used, these have limitation for study of NAFLD (Karcaaltincaba and Akhan, 2007). For example, USA, can only detect moderately severe fatty liver (greater than 30%),

and fat content cannot be adequately quantified (Lall *et al.*, 2008). In CT studies, fatty liver has a decreased attenuation compared to normal liver, and a threshold value of 10 HU below the spleen is used to qualitatively diagnose fatty liver. However, this criteria is not quantitative and is not sensitive to mild or moderate (53%) fatty liver (Lall *et al.*, 2008); (Karcaaltincaba and Akhan, 2007). MRI is currently the most sensitive technique: fat can be detected and quantified using a T1-weighted gradient-echo in/out of phase sequence (Karcaaltincaba and Akhan, 2007), but MRI is more expensive and less readily available than CT.

Dual energy CT has shown promise to address some of the sensitivity and quantification issues associated with single energy CT (Raptopoulos *et al.*, 1991); Wang *et al.*, 2003). Dual energy CT has been used to screen potential liver donors for fatty infiltration (Kamel *et al.*, 2001), however liver iron overload interferes with this measurement (Raptopoulos *et al.*, 1991). Since the information available from dual energy CT has been shown to be valuable in diagnosing fatty liver disease, it is anticipated that spectroscopic (multi-energy) CT information will improve our ability to quantify the progression of NAFLD. The first step in demonstrating this would be to illustrate differences in x-ray attenuation by fat and liver using spectroscopic CT.

Photon attenuation curves have been obtained for a diverse variety of elements, compounds and mixtures, including adipose tissue, and are well understood and available as standard tables (Hubbell, 1994). These curves are traditionally measured on a spectroscope by scanning a monochromatic beam generated using a monochromator through a range of energies and measuring the photon absorption at each energy (Berg *et al.*, 2009). However, unless an expensive

synchrotron x-ray source is used, the beams are not intense enough to provide the spatial information required for biological imaging (Berg *et al.*, 2009).

1.6 Overview of this thesis

This thesis presents a preliminary investigation of the use of the Medipix detectors for two different medical applications. The first application is the imaging of blood vessels for diagnosis of vascular diseases. The second investigation is characterising and measuring the energy dependence of x-ray attenuation in fat and liver tissue using the Medipix2 detector. Other work carried out includes the development of practical tools needed to perform these investigations.

Monte Carlo Modelling of x-ray imaging

A theoretical approach was applied to gain insight into techniques for spectral imaging of blood vessels. A Monte-Carlo model to simulate an X-ray imaging system was developed using the BEAMnrc (based on EGSnrc) Monte-Carlo particle simulation system, and is presented in Chapter 4, where Monte Carlo simulations to obtain images of a simple blood vessel phantom have been performed to investigate the relationships between the energy of the x-ray beam and x-ray attenuation in different materials.

This model can simulate the x-ray transport along the major components of the beam path, namely: the x-ray source, aluminium filter, blood vessel (two layers representing the tissue and another layer placed between them representing the blood) and the detector (using the phasespace file to represent the detector) in different situations.

The model was initially used to calculate the energy spectra of the x-ray beam. Further, investigations were carried out to study x-ray attenuation by materials such as iron (present in blood) and iodine (a commonly used contrast agent) to identify potential techniques for forming high contrast images of blood vessels using spectral information.

Application for performing digital subtraction of images

Existing x-ray imaging techniques, such as dual energy subtraction and digital subtraction angiography have been developed to improve the contrast of medical images based on conventional (energy integrating) x-ray detectors. There is potential for improvement of these techniques by applying spectral imaging techniques. For example, it may be possible to reduce x-ray dose or reduce motion artefacts by acquiring image data for image these techniques in a single x-ray exposure.

In order to study the application of spectral data to subtraction imaging techniques, a software application was developed to perform digital subtraction imaging. This application, which is written in Matlab and is described in Chapter 5, provides a Graphical User Interface (GUI) that allows images of different types (such as jpeg, dicom and tiff) to be loaded. Once loaded, the images can be transformed and registered to pixel points selected by the user and then subtracted.

The program was tested using different types and sizes of images. The images used for testing were acquired at Christchurch Hospital (using standard medical x-ray equipment) for a range of different parameters such as: iodine concentration, and x-ray energy (x-ray tube kVp).

Evaluation of the MARS-CT2 for measurements of fat in liver

Chapters 6 and 8 present investigations into the use of the MARS-CT system and Medipix2 detector to measure the fat content of liver tissue. The application of this is for improving the diagnosis of NAFLD.

A technique for flatfield correction

The intensity and energy distribution of an x-ray beam incident on a detector depend on several factors such the position (angle and distance) relative to the source, geometric orientation of the detector, and the sensitivity of individual detector elements, which may differ due to variations in manufacture.

These factors must be accounted for when forming images. So called flatfield corrections are made to compensate for these effects. The technique used for performing flatfield corrections in this thesis is presented in chapter 7

1.7 Summary

The MARS team goal is to develop CT imaging techniques that use the spectral information made available by the Medipix detector, to improve the range of information available from CT images for diagnosis various human diseases.

This thesis presents a preliminary investigation of the use of the Medipix detectors for two different medical applications. Firstly, the imaging of blood vessels for diagnosis of vascular diseases, and secondly characterising and measuring the energy dependence of x-ray attenuation in fat and liver tissue using the Medipix2 detector. This second investigation is part of work towards (eventually) quantifying the fat content of liver tissue *in vivo*, which is important for the early diagnosis of fatty liver disease.

The MARS-CT system is being developed for pre-clinical research of spectral CT applications and at the time of writing is under active development. In this context, a program to perform image subtraction (Chapter 5), and a method for performing flatfield correction of images (Chapter 7) were developed as tools for carrying out the research presented in this thesis.

Chapter 2

2 X-ray applications

This chapter discusses the background theory of x-ray imaging applications starting with a description of x-ray production in an x-ray tube followed by an introduction to x-rays and how they interact with matter. This leads into a discussion of contrast media properties and applications. The introduction to angiography techniques from the previous chapter is developed further in more detail.

Wilhelm Conrad Röntgen at the University of Würzburg, Bavaria, discovered x-rays in 1895 while studying electrons (cathode rays) moving from a high voltage anode to cathode in an evacuated "Crookes tube" (Stanton, 1896).

2.1 X-Ray tubes

Modern x-ray generators (x-ray tubes) still produce x-rays by causing electrons to strike a solid target, but techniques have been greatly refined (Figure 2.1). In a modern Coolidge tube, the source of the electrons is a heated filament. There is no need for a residual gas to be ionized, and modern tubes are evacuated to a high degree. In fact, any high energy charged particles could be utilized in the bombardment, but using electrons is the most practical method for producing x-rays.

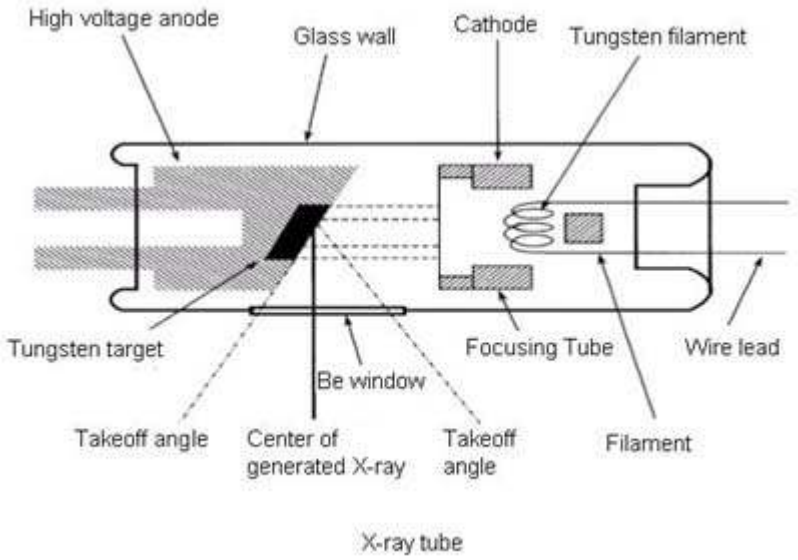

Figure 2.1 X-ray tube (Farrell and Larter, 2006).

The efficiency of x-ray production in x-ray tubes is low. Only about 2% of the energy of the cathode-ray beam is converted into x-ray energy, the rest being wasted in producing heat in the anode target. The heat production at the anode is a significant problem and dissipation of the heat has to be accounted for in the design of x-ray generators.

Early experiments revealed that x-ray spectra contained components characteristic of the material of the target. These have sharply defined energies (wavelengths). The characteristic line spectrum is superimposed upon a continuous (white) spectrum.

X-rays are part of the electromagnetic spectrum as shown in Figure 2.2, and have usually this from 10^{-1}μm down to 10^{-6}μm or energies roughly within the range from 120 eV to 250 keV. They overlap with γ-rays at the high-energy end, and they approach ultraviolet radiation at the low-energy end.

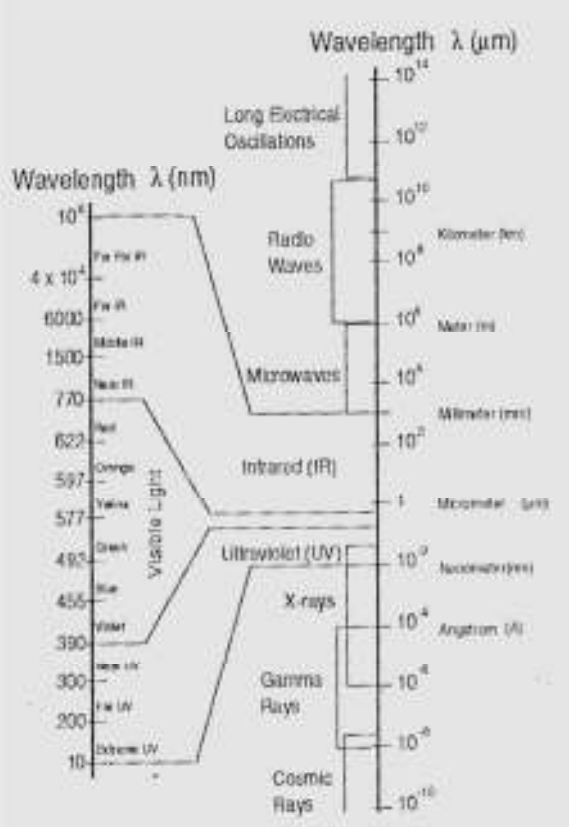

Figure 2.2 The electromagnetic spectrum have the wavelengths from 10^{-1}μm down to 10^{-6}μm.

2.1.1 X-ray tube components

The x-ray tube is an evacuated glass tube. Inside the glass envelope, at one end is a cathode, the negative electrode. At the other end there is an anode, the positive electrode. The cathode in most tubes is a tungsten filament and there were x-ray tube features with Molybdenum (Mo) and Rhodium (Rh) as target which used in mammography applications. The filament is heated by an electric current, causing electrons to be emitted from the filament by thermionic emission. These electrons are accelerated towards the anode by a high voltage (electric field) applied between the cathode and anode.

X-rays are produced when the electrons strike the anode, either by the bremsstrahlung process or electronic transitions in the anode material. The design

of the anode is used to control heat dissipation and the focal spot size of the x-ray beam.

2.1.2 The target properties

The efficiency of x-ray production depends on the atomic number of the anode target material, with more efficient x-ray production occurring in materials with high atomic numbers. A high melting point material is also necessary for the anode to withstand the high heat production. For these reasons tungsten is commonly used as the anode material in many x-ray tubes.

The anode target is often connected to a copper rod, which removes the heat from the target to where it can be cooled by oil or another coolant. Another means of protecting the target from over-heating, is to rotate the target (at high speed) so that the electrons hit it at different positions spreading the deposited heat over a larger area. The anode is designed with a small focal spot, which is necessary to produce a sharp radiographic image as shown in Figure 2.3.

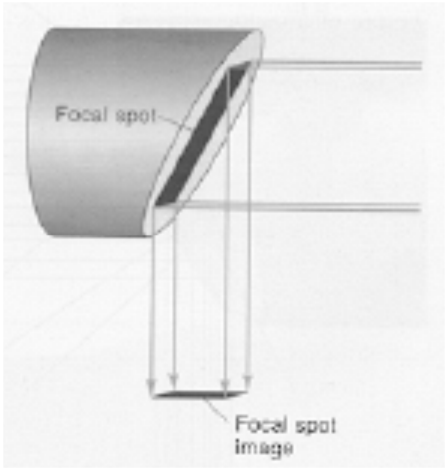

Figure 2.3 The focal spot in the area in which the electrons collide with the target (Parra, 2003)

The filament consists of wire connected to an electric circuit, and is placed in a cup, which is biased with a negative voltage (relative to the cathode) to focus the electron beam towards the target. Some x-ray tubes have two filaments and others have one, depending on the use of the x-ray.

The x-ray tube is connected to a power supply that generates the high voltage (typically 80 – 120 kV) needed to produce x-rays. Typically, the operator console has controls for setting the x-ray tube voltage, current and exposure time.

The energy spectrum of the x-ray beam emitted from the tube has a continuous distribution resulting from Bremsstrahlung interactions in the anode, with peaks of superimposed x-rays at discrete energies (characteristic radiation) from electronic transitions in the anode material. The Bremsstrahlung component of the spectrum is linear as shown (Figure 2.4: pink line).

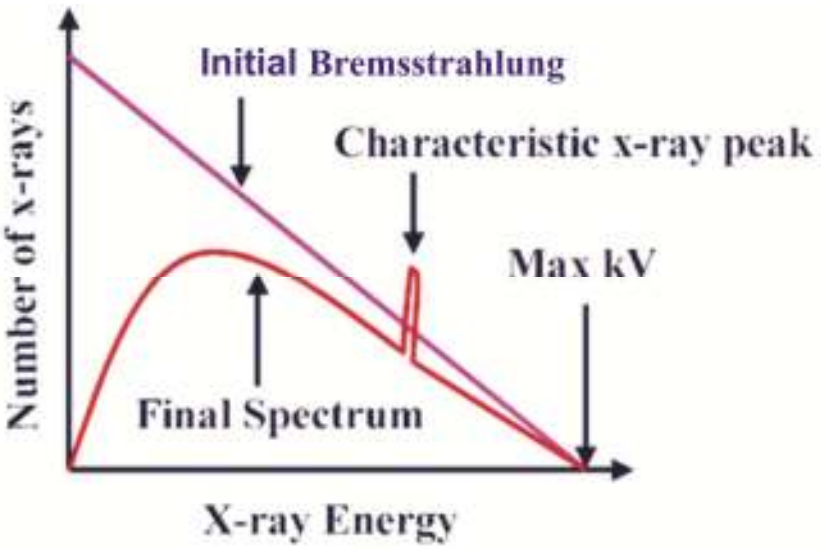

Figure 2.4 X-ray spectrum with and without filter (Hasegawa, 1987).

Inherent and added filtration causes the low energy x-rays to be absorbed, modifying the x-ray spectrum as shown by the red line in Figure 2.4. Filtration is added to remove the low energy photons that are very likely to be absorbed in the

object being imaged and have a low probability of reaching the detector. The removal of the low energy photons (known as beam hardening) increases the penetrating power of the x-ray beam, so that a greater proportion of photons passing through an object reach the detector. In conventional x-ray imaging techniques it is the photons that pass directly through the object to the detector that form the image of the object, while any scattered photons contribute to image noise. It is noted that low energy photons reaching the detector are more likely to be scattered photons than primary photons, and also that photons scattered by the object and reaching the detector convey information about the object that is not used by current x-ray imaging techniques.

2.1.3 The emission of a continuous spectrum

The continuous x-ray radiation generated by electrons in an x-ray tube has an intensity distribution that is characterized by a short wavelength limit λ_{min} (i.e. an upper energy limit E_{max}), corresponding to the maximum energy of the exciting electrons:

$$E_{\max} = eV_0$$

Where e is the electron charge and V_0 is the potential difference applied to the tube. The energy distribution exhibits a maximum at approximately 2/3 of $E_{\max}$ (see Figure 2.4). Although the overall intensity of the continuous radiation increases with applied current and potential of the x-ray tube and also with the atomic number of the target material, the relative distribution remains virtually constant. The spectral distribution of the continuous radiation is approximately represented by the following empirical formula (Carroll and Ostlie, 2007):

$$I(\nu)d\nu = i\left[aZ(\nu_o - \nu) + bZ^2\right]d\nu$$

Where I $(\nu)d\nu$ is the intensity of the continuous x-rays within a frequency range: $(\nu, \nu + d\nu)$, where *i* is the electron current striking the target, *Z* is the atomic number of the target material, ν_o is the cutoff frequency (= c/λ_{min}) above which the intensity is zero, and *a* and *b* are constants independent of the atomic number, voltage and cut-off wavelength. The spatial distribution of the continuous x-ray depends on the thickness of the target material, at low voltages and for thick targets the distribution exhibits a maximum at right angles to the incident electron beam, with this maximum moving slightly away from perpendicularity toward the direction of the electron beam as the voltage is increased.

The classic electromagnetic theory explains the emission that occurs when electrons (or other high energy particles as protons or α-particles) pass through the Coulomb field of a nucleus, where they must be rapidly decelerated as they penetrate the material of the target. Such a high negative acceleration should be accompanied by emission of radiation. The radiant energy lost by the electron is called bremsstrahlung.

2.1.4 The emission of characteristic radiation

The characteristic line energies show the same sequence as the atomic number of the elements, which the target was made of. Pioneers of x-ray theory realized that the production of characteristic x-rays involves transitions of the orbital electrons between allowed orbits or energy states, associated with ionization of the inner atomic shells of atoms in the target material. When an electron is ejected from the K shell by electron bombardment or by the absorption of a photon (a process

known as the photoelectric effect, further explained in section (2.2.2), the atom becomes ionized and the ion is left in a high-energy state.

As an example the x-ray target material, such as tungsten, needs about 60 keV to excite the atom and eject the K-electron from the atom.

The excess of energy the ion has over the normal (ground) state of the atom is equal to the energy (the binding energy) required to remove the K electron to a state of rest outside the atom. If an electron coming from an L level fills the electron vacancy, the transition is accompanied by the emission of an x-ray line known as the Kα line. This process leaves a vacancy in the L shell. On the other hand, if the atom contains sufficient electrons, the K shell vacancy might be filled by an electron coming from an M level that is accompanied by the emission of a Kβ line. The L or M state ions that remain may also give rise to emissions if electrons falling from further orbits fill the electron vacancies.

2.1.5 Spectral series of characteristic x-rays

The energy of an x-ray line can be calculated as the difference between two terms, each term corresponding to a definite energy state of the atom. The theory of x-ray spectra reveals the existence of a limited number of allowed transitions between states; the rest are “forbidden”. Selection rules for the change of quantum numbers govern the allowed transitions. Figure 2.5 shows an illustrative energy level diagram of such allowed transitions leading to characteristic lines. Relative intensities of transitions are determined by transition probabilities. In the energy level diagram, most of the x-ray lines (satellites) are very weak. In practice the most important x-ray lines occur in the K_α series.

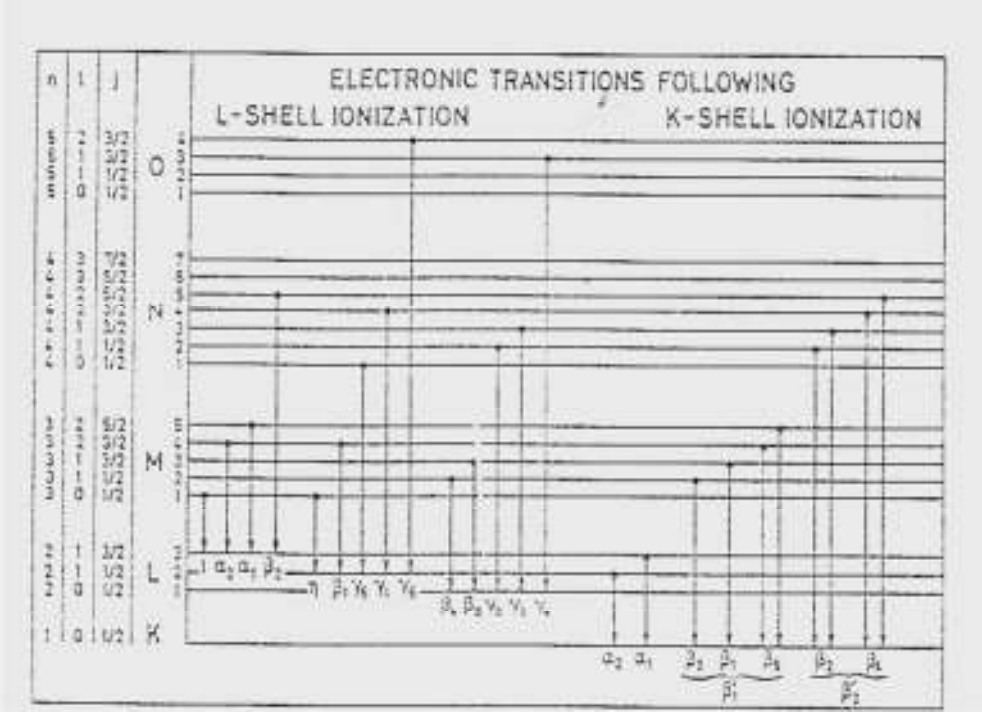

Figure 2.5 An illustrative energy level diagram of allowed transitions leading to characteristic lines

2.2 Interaction of x-rays with matter

The x-ray interactions with matter that are important in medical imaging occur with high probability over the diagnostic x-ray energy range of 20 to 120 keV. Other interactions that occur at much higher energies (such as pair production) are not covered in this thesis.

Many of the x-rays that are incident on an object do not interact with it and pass straight through, while some undergo glancing collisions with the particles of the matter (getting scattered). Some of the bombarding x-rays make solid hits and lose most or all of their energy in just one collision (being absorbed). High-energy x-ray photons are more likely to interact with electrons in the K or L-shells and the probability of an x-ray interacting with the many loosely bound electrons in a substance is small and since there are relatively few tightly bound electrons, high-energy (short-wavelength or hard) x-rays have remarkable penetrating ability.

Therefore, hard x-rays penetrate materials that are opaque to less energetic radiation. Opacity to x-rays is roughly proportional to physical density. Thus dense substances, such as bone and metal cast deep shadows in an x-ray film, whereas flesh and other substances of low density cast faint shadows.

2.2.1 Photon attenuation, half value layer (HVL)

The photons produced by an x-ray tube have a spectrum of photon energies. When an absorbing material (filter) is placed in the beam, the intensity of the attenuated beam decreases exponentially with increasing absorber thickness. The x-ray photons will interact with the absorber material and produce electrons. The attenuating processes are primarily the photoelectric effect and Compton scattering. The filter removes a greater proportion of lower energy photons than higher energy photons, so as the filter thickness is increased; the average energy of photons in the transmitted beam will increase. The intensity of a single energy x-ray beam decreases with increased absorber thickness according to: $I = I_0 e^{-\mu x}$, and illustrated by Figure 2.6. The following discussions are applied to single energy x-rays. However x-rays from x-ray machines are not single energy so the following is an approximation.

Figure 2.6 Dependence of radiation intensity on the thickness of absorber (Hasegawa, 1987).

Here I_0 is the incident intensity on the absorber; I is the intensity transmitted by a material of thickness x, and μ is the linear attenuation coefficient of the material. The negative sign indicates that the number of photons decrease as the absorber thickness increases (Archer *et al.*, 1983).

Linear attenuation

The linear attenuation coefficient μ (cm^{-1}) describes the fraction of a beam of x-rays or gamma rays that is absorbed or scattered per unit thickness of the absorber. The mass attenuation $\left(\frac{\mu}{\rho}\right)$ accounts for the number of atoms in a cubic cm volume of material and the probability of a photon being scattered or absorbed from the nucleus or an electron of one of these atoms. The linear attenuation coefficients for a variety of materials and x-ray energies are available in standard reference books such as (Hubbell, 1994). By rearranging the transmitted intensity equation ($I = I_0 e^{-\mu x}$), linear attenuation coefficients can be used to obtain several useful properties of an object being imaged.

The attenuation coefficient: μ differs between materials depending on, atomic composition, density and photon energy. The energy dependence of the linear attenuation coefficient for diagnostic x-rays having energies over the range 0 – 120 keV is such that low energy x-ray photons have a higher probability of interacting with the object than higher energy x-rays. In spectral CT this energy dependence of photon attenuation can be used to differentiate between the different body tissues.

2.2.2 Photoelectric absorption and K-edge

In the photoelectric absorption, a photon disappears and an electron is ejected from an atom. The K-shell electrons, which are the most tightly bound, are the most important for this effect in the energy region considered for x-rays. If the photon energy drops below the binding energy of a given shell, an electron from that shell cannot be ejected. Hence, a plot of τ (the photoelectric absorption cross section) versus photon energy exhibits the characteristic "absorption edges".

In Figure 2.9 where the mass attenuation of iodine is plotted over a range of photon energies, the iodine mass attenuation function consists of a series of connected curves with vertical breaks or discontinuance between them, starting at the low energy of 33.176 keV which is the binding energy of the $k_{\alpha 1}$ shell. Below 33. keV, the photon has insufficient energy to eject a K electron. Photoelectric emissions occur above 33.176 keV, which is the energy needed to eject a K-shell electron. It can be seen that for photons above 33.176 keV there is a sharp increase in the mass attenuation coefficient (Padeznik *et al.*, 2008).

Since x-ray photons have enough energy to produce ions by ejecting inner-shell electrons from an atom. Such an ion has a low-energy hole (vacancy) in its electronic structure and this vacancy is promptly filled when one of its electrons in a higher energy state falls to this low energy level. When an electron falls into a low-energy level, it releases its excess energy as radiation (see section 2.1.4, p19). The line x-rays being characteristic of the atom constituents of the matter upon which the primary x-rays are falling. To distinguish such line x-rays from the characteristic x-rays generated from the target material inside an x-ray tube and since the ionization source being different (high energy particles in the latter case

versus primary x-rays in the former case); the process is known as x-ray fluorescence and the line x-rays as fluorescence radiation. The spatial distribution of fluorescence radiation is isotropic (equally probable in all directions) upon being generated within the layers of material in which the fluorescence process takes place. It is worth mentioning that the excess of energy an atom processes after removing an electron from an inner-shell, by whatever means e.g. electron bombardment or photon absorption, and may be emitted as characteristic radiation or as fluorescence radiation respectively. Alternatively, an excited atom may return to a state of lower energy by ejecting one of its own electrons from a less tightly bound state. This transition is called an Auger effect and the ejected electrons are called Auger electrons. Generally, the probability of the Auger effect is the highest for low-atomic number elements.

The photoelectric effect on absorption or the effect on one of the interactions occurs when the photon interacts with the absorber medium (Figure 2.7). This effect occurs when a photon interacts with an atom and ejects one of the outer electrons from the atom. In the process, when the energy of the photon is absorbed by the atom and transferred to the atomic electron, it is presented as kinetic energy. This kinetic energy, given to a photo electron, is the difference between the binding energy of the electron, and the photon, when it is large enough to eject and remove the electron from its shell. When it is removed from the atom, it creates a vacancy in the shell leaving the atom in an excited state. An electron from the outer orbit can fill the vacancy. It is because of this an emission of characteristic x-ray will be seen.

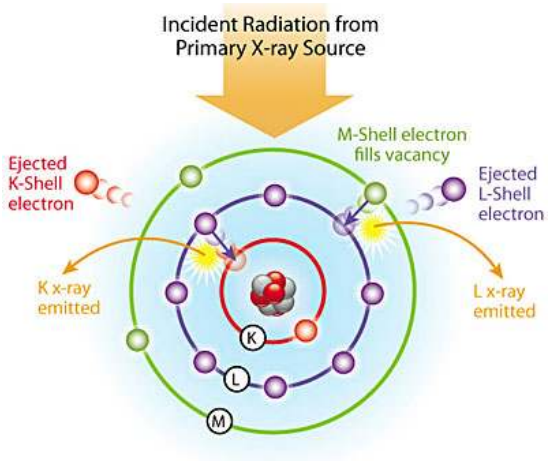

Figure 2.7 Excitation model (Pty.Ltd, 2000-2008).

In this case, the absorbed energy will be reduced by the energy emitted as characteristic radiation also called fluorescent radiation. The photoelectric absorption rate depends on the photon's energy and the atomic number of the material.

2.2.3 Fluorescence yield

The actual number of fluorescence x-ray photons produced from an atom is less than theoretically predicted, since a vacancy in a given shell might be filled through the Auger effect. Therefore, as a consequence of this competition between a radiative transition (emission of fluorescence radiation) and the Auger effect; the probability that a vacancy in an atom shell or sub shell is filled thru a radiative transition is called the fluorescence yield. Thus the fluorescence yield of the K-shell is

$$\omega_k = I_k / n_k$$

Where I_K is the total number of fluorescence K x-ray photons emitted from a sample and n_K is the number of primary K shell vacancies. Transitions at higher atomic shells are further complicated because the shells above the K shell consist

of more than one sub shell; and because of the Coster-Kronig transitions, which are non radiative transitions between the sub shells of an atomic shell having the same principal quantum number. Although, line x-ray emission is a process in which the innermost electrons in the atom are concerned and it is reasonable to suppose that the external or valence electrons have little or no effect upon the x-ray emission lines. In the K lines of low-Z elements and L or M lines of higher Z-elements the physical state and chemical combination of the elements affect the emitted line x-rays.

2.2.4 Compton scattering

Compton scattering occurs with lower probability than the photoelectric effect in the usual range of x-ray energies but occurs with higher probability than the photoelectric effect at high x-ray energies (about 100 keV and above). Compton scattering is the interaction of a photon with a free electron that is considered to be at rest. The weak binding of free electrons to atoms may be neglected provided the momentum transferred to the electron generally exceeds the momentum of the electron in the bound state. Consideration of conservations of momentum and energy leads to the following equation:

$$h\nu = h\nu_0\left[1 + \gamma\left(1 - \cos\theta\right)\right]^{-1} \qquad \text{Eq. (3.1)}$$

With $\gamma = h\nu_0 / m_0c^2$

Where $h\nu_0$ and $h\nu$ are the energies of the incident and scattered photon, respectively, and θ is the angle between the photon directions of travel before and following a scattering interaction (Stanev, 2010). Thereby, Compton scatterings produce a distribution of scattered photons with energies ranging from

$h\nu_0/\left(1+2h\nu_0/m_0c^2\right)$ to $h\nu_0$, where $h\upsilon_0$ is the energy of the incident photon and $m_0 c^2$ is the rest energy of an electron. The differential Klein-Nishina collision cross section $\frac{d\sigma_{KN}}{d\Omega}$ (defined as the ratio of the number of photons scattered in a particular direction to the number of incident photons) for unpolarized photons striking unbound, randomly oriented electrons is given by

$$\frac{d\sigma_{KN}}{d\Omega}=\frac{r_0^2}{2}\left(\frac{h\upsilon}{h\upsilon_0}\right)^2\left(\frac{h\upsilon_0}{h\upsilon}+\frac{h\upsilon}{h\upsilon_0}-\sin^2\theta\right) \qquad \text{cm}^2\text{/electron-steradian} \qquad \text{Eq.(3.2)}$$

Where r_o^2 is the classical radius of the electron.

Substituting the Compton expression of Eq. (3.1) into Eq. (3.2) gives the differential cross section as a function of the scattering angle θ:

$$\frac{d\sigma_{KN}}{d\Omega}=\frac{r_0^2}{2}\frac{1+\cos^2\theta}{[1+\gamma(1-\cos\theta)]^2}\left\{1+\frac{\gamma^2(1-\cos\theta)^2}{(1+\cos^2\theta)[1+\gamma(1-\cos\theta)]}\right\} \qquad \text{cm}^2\text{ /electron-steradian}$$

For very small energies $h\nu_0 << m_0c^2$, the expression reduces to the classic Thomson scattering cross section for electromagnetic radiation on an electron:

$$\frac{d\sigma_{Th}}{d\Omega}=\frac{r_0^2}{2}(1+\cos^2\theta) \qquad \text{cm}^2\text{ / electron-steradian}$$

For low energies of incident photons (approximately less than a few tens keV), the angular distribution of Compton scattered photons is symmetrical about $\theta = 90^o$, at higher incident photon energies, the Compton scattering becomes predominantly forward.

The differential Klein-Nishina scattering cross section $\frac{d\sigma_{KN}^{s}}{d\Omega}$ for unpolarized radiation, defined as the ratio of the amount of energy scattered in a particular direction to the energy of incident photons, is given by:

$$\frac{d\sigma_{KN}^{s}}{d\Omega} = \frac{h\upsilon}{h\upsilon_0}\frac{d\sigma_{KN}}{d\Omega} \qquad \text{cm}^2 \text{ / electron-steradian}$$

The average (or total) collision cross section σ_{KN} gives the probability of any Compton interaction by one photon while passing normally through a material containing one electron per cm^3:

$$\sigma_{KN} = \int_0^{\pi} \frac{d\sigma_{KN}}{d\Omega} 2\pi \sin\theta d\theta$$

At the low-energy limit this cross section reduces to the classic Thomson cross section:

$\sigma_{Th} = 8/3 \ \sigma r_0^2 = 0.6652 \text{x} 10^{-24}$ cm^2/electron

At high energies $h\nu_0 >> m_0 c^2$, the equation reduces to

$$\sigma_{KN} = \pi r_0^2 \frac{1}{\gamma}(\ln 2\gamma + \frac{1}{2}) \qquad \text{cm}^2\text{/electron}$$

The average (or total) scattering cross section, defined as the total scattered energy in photons of various energies $(h\nu)$ is given by

$$\sigma_{KN}^{s} = \int_0^{\pi} d\frac{d\sigma_{KN}^{s}}{d\Omega} 2\pi \sin\theta d\theta = \pi r_0^2 [\frac{\ln(1+2\gamma)}{\gamma^3} + \frac{2(1+\gamma)(2\gamma^2 - 2\gamma - 1)}{\gamma^2(1+2\gamma)^2} + \frac{8\gamma^2}{3(1+2\gamma)^3}]$$

cm^2/electron

The Klein-Nishina theory assumes the target electron is free and at rest. The binding effects, and at high energies, because of the possibility of emission of an additional photon (double Compton Effect), and radioactive corrections associated with emission and absorption of virtual photons could be accounted for by the inclusion of the so called incoherent scattering function S (x, Z) as

$$\sigma_C = \frac{1}{2} r_0^2 \int_{-1}^{1} \{[1+\gamma(1-\cos\theta)]^{-2}[1+\cos^2\theta + \frac{\gamma^2(1-\cos\theta)^2}{1+\gamma(1-\cos\theta)}]ZS(x,Z)\}2\pi d(\cos\theta) \quad \text{cm}^2/\text{atom}$$

2.2.5 Rayleigh scattering

Rayleigh scattering is a process by which photons are scattered by bound atomic electrons and in which the atom is neither ionized nor excited. Since the whole atom or solid recoil the incident photons are scattered with essentially unchanged frequency (energy) and with a definite phase relation between the incoming and scattered radiation.

Rayleigh scattering occurs mostly at low energies and for high-Z materials, in the same region where electron-binding effects influence the Compton scattering cross section. The differential Rayleigh scattering cross section for unpolarized photons is given by:

$$\frac{d\sigma_R}{d\Omega} = \frac{1}{2} r_0^2 (1+\cos^2\theta) \mp \left|F(x,Z)\right|^2 \qquad \text{cm}^2/\text{electron-steradian}$$

Where F (x, Z) is the atomic form factor given by:

$$F(x,Z) = \int_0^{\infty} \rho(r) 4\pi r \frac{\sin[(2\pi/\lambda)rs]}{(2\pi/\lambda)rs} dr$$

Where ρ(r) is the total electron density, r is the radius from the nucleus, and s=2 sin (ρ/2). At high photon energies, Rayleigh scattering is confined to small angles;

at low energies, particularly for high-Z materials, the angular distribution of the Rayleigh scattered radiation is much broader (Strutt, 1899). The total coherent (Rayleigh) scattering cross section per atom σ_R can be calculated from

$$\sigma_R = \frac{3}{8}\sigma_{Th}\int_{-1}^{1}\left(1+\cos^2\theta\right)\left|F\left(x,Z\right)\right|^2 d\left(\cos\theta\right) \qquad \text{cm}^2/\text{atom}$$

2.3 Detector techniques

All x-ray detectors in medical imaging are based on charge integration, where the detector elements convert the incident x-rays to electric charge. This charge signal is typically amplified and converted to a digital signal that can be processed by an associated computer system. The x-ray beam produced by an x-ray tube has a wide spectrum of energies and the charge generated from each x-ray interacting with the detector is proportional to the energy absorbed by the detector. Consequently, the output signal in the detector is proportional to the sum of the energies of all x-ray photons interacting with the detector. This output signal is biased towards the signal from the high energy photons in the beam, which form a less detailed image than lower energy photons, so the image contrast is reduced.

2.3.1 Medipix detector

The detector used in my thesis is a Medipix2 chip (Figure 2.8). It is a digital imaging chip, which emerged from particle detection in high energy physics experiments. The custom Medipix ASIC (application specific integrated circuit) designed at CERN.is bump-bonded to either Si, CdTe or GaAs sensors, which provide direct charge conversion of photons and therefore minimum image blurring. The detector allows setting the threshold energy or window energy,

where each pixel can set separately. This technique is used to develop the angiography application, using dual energy subtraction (Fanti *et al.*, 2003).

The Medipix chip is still under development. Actually there are several groups working on developments. There is a group which is busy developing the different parameters affecting the chip, such as the pixel size, the charge-sharing between the two neighbouring pixels; the electronic board and the signal processing. Other groups use the chip for the image applications and the developing of the active sensor material of the detector (Quarati *et al.*, 2005).

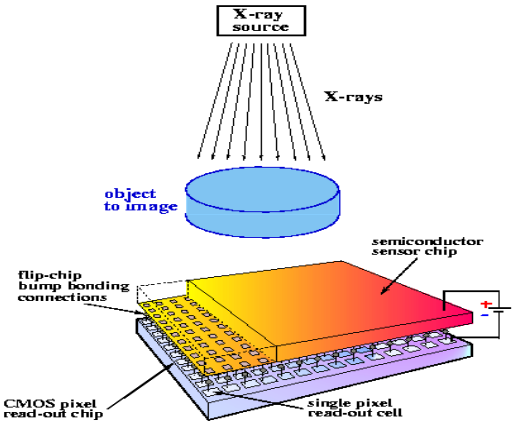

Figure 2.8 Medipix2 detector(CERN, 1991).

2.3.2 Medipix review

The first version is Medipix 1, followed by Medipix 2 (which has MXR and Timepix versions). The third version, which is now available, is the Medipix 3 series, 3.0, 3.1 and 3RX. The hybrid detector consists of a 300 µm thick silicon layer which works as the sensor material. It is bonded to a CMOS electronics chip (The Medipix ASIC). The silicon sensor is a semiconductor in which the incident radiation produces electron-hole pairs. These charges are then collected and processed by the CMOS ASIC (complementary metal oxide semiconductor). The

electronics count every event in each pixel. The advantage of the Medipix ASIC is that it has a pulse height discriminator, which allows the system to count events only within a selected energy range (Pfeiffer *et al.*, 2003, Quarati *et al.*, 2005, Butler *et al.*, 2008).

Medipix2 is used to get a clear image since it is designed with a 55μmx55μm pixel size and it is possible to detect one energy band at a time. The detector is an array of 256x256 pixels about 1.4×1.4 cm^2. This is quite small compared to a conventional x-ray detector, but has a spatial resolution ten times higher than other CT detectors. There are collaborating groups working to develop the detector in different areas, such as: developing the semiconductor materials; reducing the pixel size and increasing the number of pixels to overcome the problem of charge-sharing between neighbouring pixels. They have developed also the electronic part to get a fast read-out and fast processing (Quarati *et al.*, 2005).

The Medipix2 detector has been used widely in x-ray imaging (Fanti *et al.*, 2003). It has been tested by using Monte Carlo simulation in order to have the same result to compare it with the first experimental results. The first image of small fish was great; it showed the small inner details clearly. The chip has been tested for other applications such as angiography.

2.3.3 Medipix properties

The Medipix2 detector has a 256 x 256 array of pixels, where each pixel receives the charge deposited in the detector sensor layer. The charge pulse (input), which has amplitude proportional to the photon energy, is amplified and then sent to two

programmable comparators that define the upper and lower threshold of an energy discriminator. The device then counts the number of x-ray photons hitting the detector elements that fall within the selected energy range. These capabilities, provided by the Medipix2 detector, open a new window for applying information about the energy of detected photons to medical imaging techniques (Quarati *et al.*, 2005). It is suitable for use in angiography (Butler *et al.*, 2008).

Giuseppe Baldazzi came up with a new approach where a quasi-monochromatic beam with mean energies, lower and higher than the iodine k-edge was used (Baldazzi *et al.*, 2001a). The two beams fall on to the phantom. They pass through a small slot to allow the low energy and high energy to fall down to two detectors. The signals are treated within the electronic part and then the dual energy subtraction is made (Baldazzi *et al.*, 2001b). The technique of the dual energy beam for the angiography practice has been presented (Bornefalk *et al.*, 2006). It shows powerful performance in terms of contrast (Butler *et al.*, 2008).

2.4 Contrast agents used in x-ray imaging

The use of radiographic contrast medium dates almost from the discovery of x-rays. Three aspects of any medical image that must be taken into account when analysing it: are contrast, spatial resolution and noise. Spatial resolution determines how well details of the position of smaller objects in it can be seen; noise is related to the accuracy of the signal, in other words how precise it is. Large fluctuations across the object denote a “noisy” image, while an accurate signal produces smaller fluctuations.

Contrast is the difference in intensity between different objects in an image, particularly between an object of interest and the surrounding tissues. In medical images, information is represented in displayed images using grey scale. If the images have large differences between the grey levels, it will make it clinically easier to read. When a contrast agent is administered, the absorption of x-rays organs containing the contrast agent is increased compared to the surrounding tissue.

Image contrast depends on two factors i.e. the characteristics of the object being analysed, and the type of device that is used. The variables that can improve contrast are outside the patient. They depend on the x-ray beam whose kVp can be altered, and on the detector response. What is more difficult and sometimes impossible to control, are factors within the patient ie. Thickness, density and composition of the tissues. These also contribute however, to the formation of contrast within the image while it is being recorded.

Contrast agents may be positive (increase x-ray attenuation) such as iodine or barium compounds or negative, such as gases. There are several reasons why iodine and barium are used as contrasting agents. Firstly is their ability to integrate into non-toxic chemicals. Secondly, their linear attenuation coefficient is greater than those of other materials within the body (Figure 2.9).

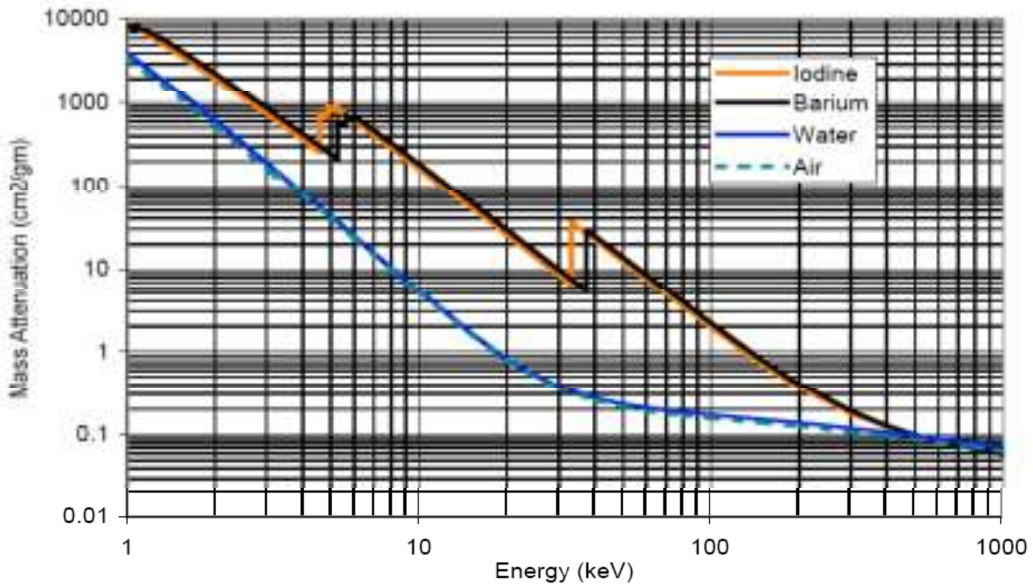

Figure 2.9 Mass Attenuation Coefficients for Contrast Agents (Hasegawa, 1987).

When iodine contrast agents are used, the iodine, for example, will assure x-ray attenuation which in turn, will produce a notable contrast in the surrounding tissues. Gaseous contrast agents however, absorb fewer x-rays than tissues because of their low density and the effective atomic number which is higher. On the other hand, positive contrast agents absorb more x-rays than tissues because of their high density and higher atomic number. Different types of contrast media have been used for a long time and have been developed to avoid toxic effects on the patient. For a long time, iodine has been the most popular contrast medium (Skucasm, 1989).

2.4.1 Iodine

Iodine has a high atomic number (Z=53) and is characterized by k-edge energy at 33.2 keV (Ullman *et al.*, 2005). Medical use of iodine is associated with adverse side effects in patients. Research shows that when iodine metal is administered to patients over long time periods, it has a toxic effect on the kidneys and may cause nephritic problems or kidney failure (Moranne O *et al.*, 2006). Consequently,

iodine is not suitable for patients suffering from kidney and thyroid problems. Also, in addition to possible kidney damage, patients may develop allergic reactions.

2.4.1.1 X-ray absorption by iodine

Iodine has a high x-ray absorption cross section, and is used widely as a contrast medium in diagnostic x-ray examinations. It is used for example in angiography scans, where iodine is injected in to the patient's blood vessels with a catheter.

In conventional x-ray imaging techniques it is simply the high x-ray attenuation by iodine that is utilised to form high contrast images. However, other materials such as calcium in bones and other tissues may also form high contrast regions in images. The absorption of x-rays by iodine increases above the iodine k-edge energy. When spectral information about detected x-rays is available, the sharp change in x-ray absorption that occurs at the iodine k-edge energy may be used to differentiate between regions in the image containing iodine and regions in the image containing other materials with high x-ray absorption such as calcium.

2.4.2 Barium Sulphate

Barium Sulphate is an insoluble, radio-opaque compound used as a contrast media that is administered orally to diagnose problems with the gastrointestinal (GI) region. When barium is taken by mouth, it makes the upper areas of the GI region, the stomach, and the small intestines appear white in radiographic x-ray images. This test is commonly called an 'Upper GI' test. Usually several x-rays images are taken to observe the barium as it travels through the gastrointestinal tract. The barium procedure provides information about the GI region and how well it is

working. Generic barium sulphate oral suspensions are available (Holleman and Wiberg, 2001).

2.4.3 Gadolinium

Gadolinium is naturally occurring metal. It has a high atomic number (Z=64) and the K-edge is at 50 keV, which is higher than that of iodine. These properties mean it is a strong absorber of high energy x-rays.

There are various types of gadolinium contrast media. Gadolinium is usually mixed with other chemical metals to reduce the toxicity. There is a problem though, as gadolinium tends to accumulate in the renal tissue over a long time, consequently, it can cause renal failure (Nolte-Ernsting *et al.*, 1998). Gadolinium is a paramagnetic material and due to this property is widely used as a contrast medium in MRI (more so than as a high Z contrast agent in x-ray imaging). Gadolinium is also used as a contrast medium in angiography when using image subtraction techniques.

2.5 Computer Tomography (CT)

Similarly to conventional x-ray, contrast materials may be used in CT procedures to increase x-ray attenuation to improve contrast detail in images. It uses a special x-ray tube fixed in a gantry. Numbers of detectors face the x-ray tube to read the x-ray falling on them. This produces multiple images and the output signals are processed in an advanced computer to put them together in cross-sectional view. The CT scan can image more sensitive parts of the body such as the brain, kidneys, lung, heart and neck (Groberg T, 1983). The patient should not wear any item that may affect the image such as metal objects, including jewelry,

eyeglasses, dentures and hairpins, may affect the CT images and should be removed prior to the exam. Hearing aids and removable dental work must be removed. Women will be asked to remove bras containing metal underwire, because the images in the CT scan are taken at different detectors. The image is reconstructed in the first loop and then subtraction techniques are applied.

The CT scan, if compared to ordinary x-ray, will show more inner details, when the image slices are assembled by computer software. The output images show details in multidimensional views of the interior of the body. When the patient is placed on the CT table, the scanner starts acquiring the mask image without the contrast media. The contrast media is injected and after a short period, the table starts moving towards the scanner. The image will be acquired in spiral patterns. Normally it is acquired in a position on the desired place to get a number of slices in certain positions to look for more details, as the table moves and the contrast media are injected at the required fixed rate in slices of the image.

2.6 Magnetic resonance angiography (MRI)

MRI is one of the other non-invasive imaging techniques used to diagnose disease. Magnetic resonance angiography (MRA) is safer than x-rays or a CT scan because it does not use ionising radiation. Instead, radio waves are directed at protons (the nuclei of hydrogen atoms) while a strong magnetic field is applied. The electric field causes the hydrogen nuclei to resonate; this resonance generates a radio signal that can be detected by a second set of electric coils (receiver or field coils).

The receiver coils are located around the desired part of the body (there are different coils for various part of the body). As the patient lies in the MRI unit, radio waves are applied (then switched off) to the protons in the area of the studied part. The protons change the alignment of their magnetic moment, producing signals that are detected by the coils. Specific sequences of radio pulses are used to acquire data that may be transformed using computed tomography to form three-dimensional images of the organ or blood vessel.

The protons are abundant in water, so the MRI image shows the difference in water content between various body tissues. The area that is diseased has more water than the other healthy areas. The differentiation of abnormal tissues from normal tissues is easier with MRI than with other imaging modalities such as x-ray and CT.

The MRI uses gadolinium, which is a paramagnetic metal, as the contrast medium. When the contrast medium is introduced during the procedure it alters the local magnetic field causing the hydrogen nuclei in blood vessels (containing the gadolinium contrast) to have a different signal to hydrogen nuclei in other tissues (not containing gadolinium). In reconstructed images this signal causes the regions containing contrast material to have a bright white colour (Nolte-Ernsting *et al.*, 1998).

2.7 Angiography

Angiography is a medical x-ray imaging technique which shows the morphology of blood vessels and the organs in the body. The term angiography comes from Greek words meaning “vessel” and draw”. The x-ray film image of the blood

vessel is called an angiogram and can be used to identify information about factors such as occlusion or stenosis in the blood vessels that are used for making clinical decisions on patient treatment.

Angiography techniques are required to diagnose cardiac disease in a blood vessel: to do this a catheter is inserted into the vessel and iodine dye is injected through the catheter (Baldazzi *et al.*, 2001b). X-ray images are taken both before and after the contrast medium is injected, the image taken before contrast injection is subtracted from the x-ray image taken with contrast to remove background tissues in order to provide enhanced images showing the morphology of the interior vessel. However, due to patient movement during the imaging the subtracted image may become blurred. Consequently, the conventional angiogram is done under controlled conditions, where the patient must hold their breath during the scan and not make any movement.

The purpose of angiography is to specifically image and diagnose disease of the blood vessel (Kenneth *et al.*, 2003) especially to diagnose blockages of blood vessels. However, not all angiography techniques show the different thicknesses of the blood vessel (Nolte-Ernsting C, 1998). Some small vessels cannot be seen or are not clear. The development of the techniques of angiography will lead to sharper images even of the smallest vessel in the body. The many different techniques used in angiography are: an ordinary x-ray machine, computed tomography CT and magnetic resonance image MRI. These techniques are all used with contrast media.

The standard angiography technique for imaging blood vessels is to use a fluoroscopy x-ray machine, with iodine used as a contrast medium. In fluoroscopy

the patient are exposed to x-rays at the same time as the contrast medium is injected into the patient to acquire x-ray images that show the blood vessels. There are several problems with this simple approach, for example shadows formed by overlying tissue may appear as a plaque in the blood vessels (leading to misdiagnosis) and the process exposes the patient and operator to a high radiation dose.

Another technique to improve image contrast and to show a better image between the body elements' composition is dual energy subtraction (Alessandra *et al.*, 2002). The technique works when the subject or patient is imaged twice with different energies of the x-ray source. The technique uses the k-edge subtraction imaging where the two energies are chosen: one energy peak below the k-edge of the contrast media and the other peak just above the k-edge. The subtracted image is clearer and has better contrast (Kobayashi, 1998).

2.8 Multi energy imaging

Modern angiography can be performed using dual energy techniques such as digital subtraction angiography (DSA) and dual energy angiography (DEA) (Schena *et al.*, 2003).

2.8.1 Digital subtraction angiography (DSA)

The first image of the blood vessel is acquired without contrast media at kVp above the iodine absorption edge. The second image is acquired with iodine contrast medium at the same x-ray machine setting, where high absorption takes place in the iodine. In order to make a clearer image, the second image is subtracted electronically 'by using special software developed for this type of

subtraction' from the first image, known as the mask, to make a very clear image of the blood vessel.

The disadvantage of this technique is that the patient is imaged twice which means the patient has to take exactly the same imaging position. Sometimes, this is very difficult to achieve, especially with patients who are not very cooperative. On the other hand, the patient has to wait for a long time for the iodine to be distributed in the blood vessel before the images are acquired. This is a time-consuming process and is more expensive for the patient and the hospital.

2.8.2 Dual energy angiography (DEA)

DEA avoids some of the problems of DSA where two images, one taken before, and one after injection of contrast agent are subtracted. Instead, DEA subtracts two images, taken at two different x-ray energies, one below and one above the contrast K-edge energy.

In dual energy imaging, a patient is injected with the contrast medium, in this case with iodine, and the images are taken twice at the same position. From the first image, the x-ray machine's applied voltage is set below the iodine absorption edge and the image is acquired. In this case the absorption of the iodine is relatively small and no clear image of the vessel will appear. In the second image, the x-ray's applied voltage is set just above the iodine absorption edge. The absorption of iodine will be at the maximum and the image will show a clear picture of the vessel. Subtraction is taken of the two images taken at different energies. The output image will show the blood vessel and will be clearer and better (Prino *et al.*, 2008).

The advantage of this process is that, first it is much less time consuming for the patient remaining on the table; secondly, imaging is not sensitive for relative change in the patient's position. Accordingly, the error will be less. The process is much more convenient for the patient and more economical for the hospital and patient. This technique has been used for long time. It was developed in order to get the best k-edge energy by applying different x-ray tube targets, energy, and various settings to be used with different contrast media, such as gadolinium and iodine. The subtraction techniques used with the dual energy improve the image.

The Medipix detectors have the advantage of acquiring an image at a selected energy. It can also acquire an image using different energies at the same time (Wright *et al.*, 2005).

2.8.2.1 Dual energy imaging with iodine contrast

The mass absorption coefficient μ_m of iodine decreases with energy until about 33.2 keV. At this energy, called the absorption edge coefficient, the value at that point jumps drastically. Immediately after the edge's absorption rise, this property is utilized for dual energy imaging. The techniques work by subtracting the image acquired before the edge at low energy subtracted from the image acquired exactly at the edge or above it where the absorption is at a maximum. The output image will show good contrast image. The scattered and absorption events depend on the photon energy, from (Figure 2.10) it is clearly that the variation between the absorption at different composition, where at low energies give better soft tissue contrast (Prino *et al.*, 2008).

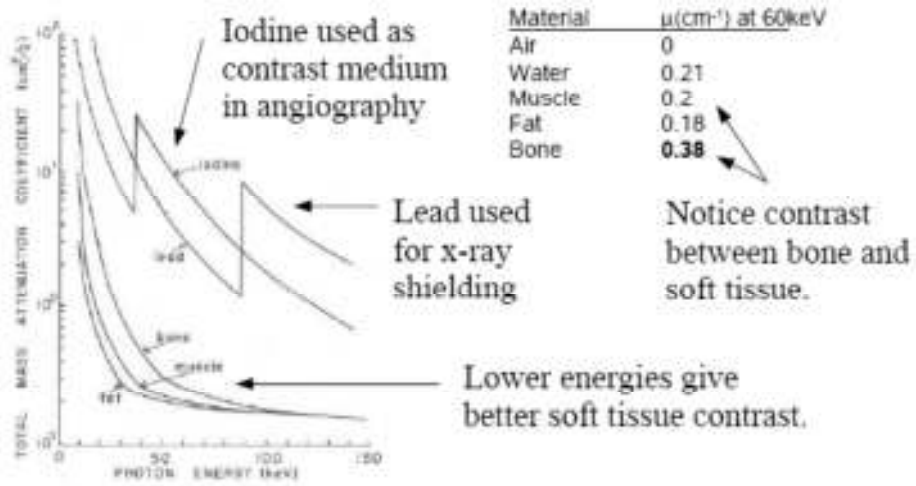

Figure 2.10 Scatter and absorption events depend on photon energy (Hasegawa, 1987).

2.9 Summary

This chapter has reviewed angiography imaging techniques, which use x-ray images with iodine contrast to show the details of the blood vessel morphology. There are two different techniques used to acquire the image, these are digital subtraction angiography (DSA), and dual energy angiography (DEA).

Digital subtraction angiography is a well-established technique for removing background tissue structures in imaging studies using contrast media. In these studies, images are acquired before and after contrast media injection, and the images containing contrast media are subtracted from the images without contrast medium (mask images).

In dual energy angiography the requirement to acquire two sets of images one before, and one after (iodine) contrast media injection is eliminated by utilising the differences in x-ray attenuation at energies just above and below the k-edge energy of iodine (33.2 keV). X-ray photons with energies just below the iodine k-edge energy are attenuated much less strongly by iodine, than those just above the iodine k-edge energy.

The work presented in this thesis has reviewed these multi-energy techniques that improve the contrast of angiography imaging studies by subtracting images obtained at two different energies, one below and one above the k-edge of iodine.

.

Chapter 3

3 Overview of MARS-CT system

The aim of this chapter is to describe the Medipix technology as used in the MARS-CT scanners built in Christchurch, New Zealand. We used the innovation x-ray detector to develop MARS-CT system supplied with Medipix detectors. This innovation is joint project amongst the University of Canterbury and University of Otago in New Zealand, and the CERN Medipix collaboration in Geneva. The first version of the scanner, MARS-1 (Campbell et al., 1998), was built and put into operation in late 2007, followed by the advanced MARS-2 (Llopart et al., 2001), introduced in 2008 with upgraded technology and improvement, following this the MARS-3 was introduced with further improvements and a new layout. The MARS group still working to develop new improved scanner systems having advance technology.

This chapter describes the progression of the different MARS-CT models and particularly in MARS-2 where the data of this study performed, it is important to mention that MARS-CT systems are designed for preclinical applications. The MARS-CT2 system workflow is explained by showing details of the system and its operation.

3.1 CT imaging definition

The attenuation coefficient describes the extent to which the intensity of an x-ray exposure is reduced as it passes through a specific material and it is dependent on the thickness and density of the material, and the atomic number and photon energy. The total attenuation is the sum of the attenuation due to the different

types of interactions, such as; Rayleigh scattering, Compton scattering, Photoelectric absorption and Pair production (Pair production is not significant for photon energies used in diagnostic imaging). The probability (cross-section) of these interactions occurring varies with energy. In CT applications only Rayleigh scattering, Compton scattering and Photoelectric absorption are significant (Wang *et al.*, 2011).

Figure 3.1 shows the total mass attenuation coefficient for soft tissue (Z=7) along with the mass attenuation for each of the different x-ray interactions with matter as a function of energy (Bushberg, 1998). For energies range below 50 keV the dominant interaction is photoelectric absorption. For energies from 50 keV up to 90 keV both photoelectric absorption and Compton scatter interactions are significant and finally for energies between 90 keV to 150 keV Compton interactions are the most dominant.

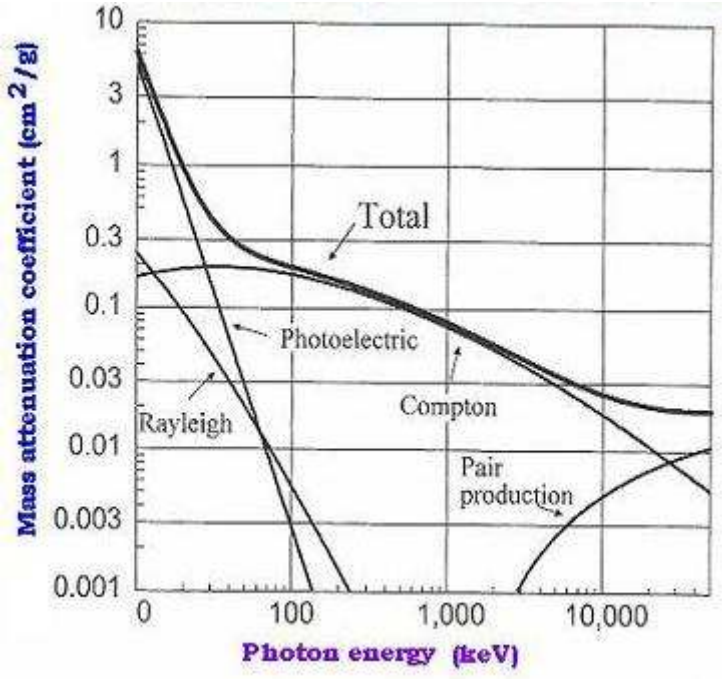

Figure 3.1 Mass attenuation coefficient as a function of energy shown for the major types of photon interaction with matter (Bushberg, 1998).

Attenuation due to the photoelectric effect, which dominates at low energies, varies in proportion to E^3 (Alvarez and Macovski, 1976). This strong energy dependence of attenuation at low energies is an important property that will allow spectral imaging techniques to detect differences in tissue composition. Compton scatter is somewhat less dependent on photon energy see Figure 3.1. Different combinations of materials can produce similar absorption, which is why conventional CT is unreliable for distinguishing these materials. The spectral information available from photon counting detectors such as the MedipixRX has the potential to allow better differentiation and identification of the material composition of tissues.

3.2 Developments in CT imaging techniques

In the time since the CT scanner was invented by Hounsfield in 1973, it has been a valuable diagnostic tool in the field of radiology (Ambrose and Hounsfield, 1973, Roentgen, 1895). Conventional CT technology has been advanced by developments to improve spatial resolution, speed and structural design and adding new functions such as multi-slice detectors and dual energy subtraction CT. These developments have improved the resolution and clarity of anatomical details, providing enhanced discrimination of tissues and facilitating more accurate diagnosis.

The theory behind all current CT imaging techniques is the measurement of the x-ray attenuation properties of the tissues and contrast materials in the object being scanned. Figure 3.2 show the development of CT imaging techniques from standard CT scanning to dual-energy subtraction and then spectral imaging using the MARS-CT system. In standard CT imaging, x-rays are passed through the

object to obtain the x-ray intensity measured at the detector. The attenuation of each x-ray photon depends on the photon energy, and the atomic number and electron density of the materials between the x-ray source and the detector. In reconstructed CT images the gray scale represents the attenuation coefficient of the material in each voxel (Schena et al., 2003). The standard CT represents the attenuation by tissue in a voxel using a single scalar value called Hounsfield Unit (HU) (described in section 8.2.3.1, P.162). Hounsfield units normalise the attenuation values such that $HU_{water} = 0$; $HU_{air} = -1000$, but otherwise do not identify the composition or type of tissue (Alvarez and Macovski, 1976).

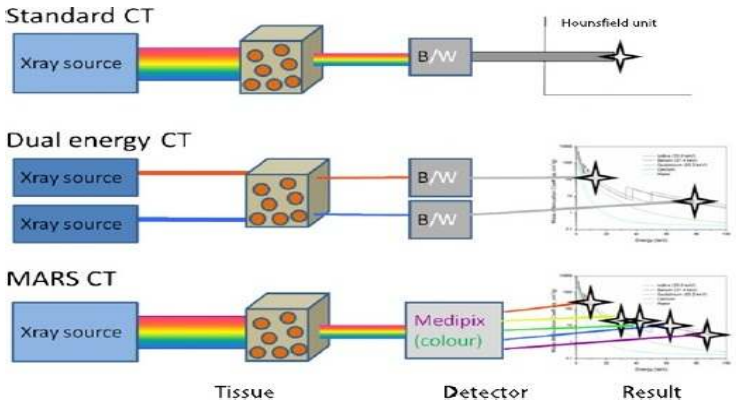

Figure 3.2 Diagram to illustrate the differences between standard CT, dual-energy CT and spectroscopic MARS CT. Note that standard CT detects attenuation signals from all energies combined, dual-energy CT improves the measured attenuation signals using two energies, but only the MARS CT system can detect attenuation signals for multiple discrete energies to allow a more complete attenuation curve to be reconstructed (Anderson *et al.*, 2010).

In dual energy CT (described in section 2.8.2), two x-ray projection images are taken at each angular position of the gantry. The first image is taken below the k-edge energy of the contrast medium, and the second image taken just above the k-edge energy. This is done to improve the contrast of the reconstructed images,

allowing scan times to be reduced to minimise artefacts (including blurring) due to movement of the patient (Marshall *et al.*, 1981, Marshall *et al.*, 1984).

The MARS-CT system uses the spectral information provided by energy selection features of the Medipix photon counting detector to determine characteristics of the materials in a scanned object, which are described as follows. The Medipix detector uses a semiconductor sensor layer (currently either Si, GaAs, or CdTe) operated as a proportional radiation detector to convert x-ray photons into electron pairs that are amplified and shaped to form an electrical pulse that can be counted as a photon interaction. The amplitude of the electrical pulse is proportional to the photon energy. Consequently, a pair of voltage comparators may be used to select and count pulses that have amplitudes above and below pre-defined threshold levels. Since the pulse amplitude is proportional to energy, this allows the detected photons to be sorted into groups that represent photons detected within a predefined energy range. This allows information about the energy dependent differences in x-ray photon attenuation in different materials to be applied when reconstructing images to improve the differentiation between tissues in medical images. The MARS-CT can acquire data for multiple x-ray energy ranges per image (potentially up to 8 energy ranges in a single exposure) and provides the technology platform necessary for acquiring spectroscopic CT images (Anderson *et al.*, 2010, Fornaro *et al.*, 2011).

3.3 MARS-CT system development

The improvements in resolution, sensitivity and qualitative accuracy for sample imaging that are possible with spectral CT, allow the MARS-CT design to obtain information on molecular composition of the tissue (Fornaro *et al.*, 2011). This

advanced technology is now available as an alternative technique to image small samples and to produce tissue morphology (De Kemp *et al.*, 2010).

The experimental studies presented in this thesis were performed using the MARS-CT2 system developed by our group. This system is equipped with a Medipix spectroscopic photon counting detector (Butler et al., 2008, Butzer et al., 2008) Figure 3.3., Several versions of MARS-CT have been developed, with these different versions incorporating improvements in mechanical design and utilising different versions of the Medipix detector (Butler *et al.*, 2008, Zainon *et al.*, 2010). This detector has the ability to image biological samples and may be used other applications. In this thesis I used the MARS-CT2 to scan biological samples and particularly fatty liver.

Figure 3.3 The MARS-CT scanner show the main components, (1) Motor controller, (2) Fan switch, (3) Power supply, and as labeled the x-ray control and MUROS readout.

The main components of the MARS-CT scanner are: a lead shielded box that holds the gantry, stepper motors, motor controller, x-ray tube, cooling fans, power supply, and the Medipix detector and sample holder.

The MARS-CT has been used for preclinical applications such as imaging of atherosclerotic plaque and soft tissue (Zainon *et al.*, 2010, Berg *et al.*, 2009). This

scanner has the ability to enhance differentiation between material types such as between fat and liver tissues and contrast agents.

3.4 The MARS-CT system layout

The MARS-CT system scanner contains several sub-systems that are used together to construct the image see Figure 3.4. These include the MARS scanner, the MARS console, and the MARS workstation, which is used for image processing. The specimen is held in the MARS-CT unit during the scanning process, and the MARS console is used to control the movement of gantry and detector. The gantry, x-ray tube and other scan parameters can be adjusted from the MARS console, which provides the interface needed to control the system and collect data during scans.

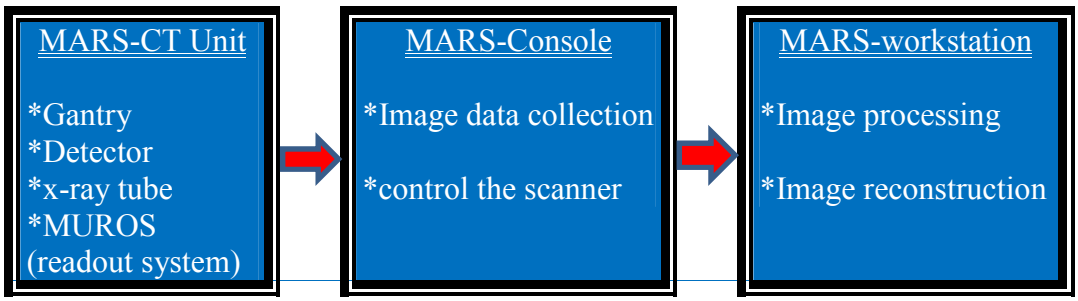

Figure 3.4. The workflow of MARS-CT system, show the three sub-systems involved in this process. The three sub-systems are MARS-CT Unit, MARS-CT Console and MARS-CT Workstation.

The MARS workstation is used to process the data collected during sample scans. This processing includes using Matlab (used in this study) for image processing to enhance images (e.g. image subtraction operations, and flatfield correction of images: see Chapters 5 & 7), and using the Octopus visualization software to construct 3D CT images.

3.4.1 MARS-CT system unit

The MARS-CT system unit consists of the gantry, detector, x-ray tube and MUROS readout. The gantry is designed to hold the x-ray tube, detector and the sample, and can rotate 360 degrees around the sample axis. The rotation is performed by a stepper motor in increments of approximately 0.05 degrees. It is also possible to move the sensor along the detector translation axis, which is tangential to the detector rotation path.

The MARS-CT2 is equipped with a Medipix detector (either Si, GaAs or CdTe). Since the active area of the detector is 14 x 14 mm the detector unit is designed to move vertically to cover the field of view needed to scan larger objects.

A portable micro-focus x-ray tube (Kevex PXY-11-150-75) is installed in the MARS-CT2 scanner. The tube has a tungsten target with a focal spot size of 45 μm and an exit window of 0.125 mm thick beryllium, the maximum tube current is 0.15 mA and the tube accelerating voltage is 75 keV. To harden the x-ray beam a thin layer of aluminium is used.

The Medipix readout unit (MUROS) is an electronic interface for the Medipix detector, which contains the power supply and control circuits needed to operate the Medipix chip and communicate with the MARS console computer through a PCI card (Giersch, 2005).

3.4.2 MARS-CT system Console

The MARS Console, which is located outside the MARS scanner, allows the user to control the MARS scanner by setting the parameter values needed to perform scans such as, the x-ray tube current and voltage, and the gantry and detector movements. The console runs the PixelMan software to control the detector and

view images as they are acquired. The console also allows parameters such as the detector energy selections, acquisition time, and parameters used to control the system to cover the field of view for a specific sample to be adjusted. Image data from the scanner is collected and stored by the console for later use at the workstation to do image processing.

3.4.3 MARS-CT system Workstation

Images are transferred from the MARS console to the MARS workstation for image processing, reconstruction, 3D visualization and display. The MARS workstation provides a variety of software applications such as Matlab, which used for image processing using codes developed by members of our group. The Octopus software package is used to produce 2D CT images and has features that may be used to control and reduce artefacts in images. Other plotting software enables users to process and view the complete spectral dataset as 2D and 3D images.

3.5 MARS-CT operation

The control of the three main gantry motors is performed by a microcontroller that is interfaced via Matlab. Our group has also written software libraries to control most of the functionality of 'Pixelman' from within Matlab. This includes setting all DAC values, loading a THL equalization mask and the noise mask and performing the image acquisition. The noise mask is used to deactivate individual pixels that have abnormal behaviour.

The MARS-CT scan procedure has been automated and parameters to control the scan are defined at the beginning of each scan. These include the number of

rotational steps, the number of sensor positions needed to enlarge the field of view, the different energy threshold settings and the acquisition time. To perform a scan, the sensor is first moved to its top position, then images are acquired for each selected energy range, after this the sensor is translated (by 256 × 55 μm = 14.08 mm) to the next translation position and the next acquisition is made. Once, the complete field of view has been imaged, the sensor is returned to its top position and the gantry is rotated to the next angular position. The amount of rotation between each angular position is defined at the beginning of each scan, and set so that an integer multiple of rotation steps corresponds to (exactly) 360 degrees rotation. The image from each rotational position is called a 'projection'. Each projection is stored as a Matlab file that includes the image data, the values of parameters used to specify the scan and calibrated values of various system parameters. The data saved is then transferred to the MARS workstation for performing the image processing and visualization tasks.

3.6 Summary and discussion

This chapter has introduced the MARS scanning systems and their operation particularly the MARS-CT2 system, which is used for the experimental studies presented later in this thesis. The spectral capabilities of the MARS-CT have been introduced and discussed in relation to conventional CT systems.

Dual-energy CT has brought spectral x-ray imaging into clinical reality and proven its benefit in numerous applications such as distinguish fatty liver. The MARS group at University of Canterbury together with physicists from Christchurch Hospital constructed a Medipix based spectral CT scanner. With this scanner, images are taken not only from different angles as in CT, but also for

different energy ranges. Because of the new energy resolution that Medipix provides, our system was dubbed ‘Medipix All Resolution System’ (MARS).

Chapter 4

4 Monte Carlo simulations of X-ray imaging

4.1 Introduction

The BEAMnrc/EGSnrc Monte Carlo simulation system was used to develop a simple simulation model of the major components of a complete angiography x-ray imaging system, namely, the x-ray tube anode (electron target), primary aluminium filter, collimators, blood vessel and the detector. The model was initially used to simulate the energy spectra of the x-ray beam emitted from the x-ray tube, and then subsequently, the energy spectra of the transmitted x-ray beam, which passes through the blood vessel to the detector.

The first major use of Monte-Carlo simulations was in 1944 (Pllana and Sabri., 2003), by researchers working on the Manhattan project to develop the first atomic bomb. The scientists working on this project had difficulty to solving the complicated equations related to the fission of Uranium. They finally solved these equations by using what is now known as the Monte Carlo method, which is applied to solve the equations by statistical methods based on tracking individual particles.

The BEAMnrc/MP system for Monte Carlo simulation is designed for simulating radiotherapy sources. BEAMnrc uses the EGS4 Monte Carlo code system to simulate paired electron and photon transport (Electron gamma shower 4: (Kawrakow and Rogers, 2001)). The range of particle energies that can be simulated by EGSnrc is from 1 keV to 1 GeV, where the lower energy limit is due to uncertainties in cross section, and breakdown of the particle tracking concept,

which loses validity in the eV range. The high energy limit is due to the lack of irradiative corrections. EGSnrc can simulate interactions with elements having atomic numbers from Z=1 to Z=100 and also materials comprising a mixture of these elements.

The EGSnrc system contains information such as the interaction cross-section of many elements and compounds as a function of their density, and the energy range of the interacting electrons and photons. And, allows parameters of simulated objects such as the material composition, density and mass to be defined, as well as the energy range over which particles will be tracked in the simulation. The code also allows defining the desired compound or element and then saving it to the file in order to use that material or compound in the component modules (CM) simulation of the x-ray imaging system.

The Monte Carlo simulation requires the description of the geometry of the x-ray imaging system. BEAMnrc provides general purpose component module codes for defining the geometry of objects to be simulated. The advantage of these tools is that the simulation can be easily and quickly defined.

The BEAMnrc component modules allow simulations for most types of medical linear accelerators to be defined. For example, there is a component module for simulating an x-ray tube, which is used in this chapter, that allows parameters such as the anode target material, the acceleration potential of electrons striking the anode target, and the angle of the target to the incident electron beam to be defined. All important parameters of the x-ray tube can be defined.

The phase-space file is defined and used to store all the data about simulated particles reaching a specified location, such as, a plane intersecting the Z-axis. This data includes the particle type, energy, and direction vector, as well as data from the simulation such as information about statistical errors, and interaction history of the particle. In the simulations presented in this thesis the data in the phase-space file is assumed to represent the x-ray beam incident on the detector.

In the following sections BEAMnrc is used to perform a Monte Carlo simulations of x-ray imaging of blood vessels (as used in angiography) to obtain the transmitted energy spectrum. These simulations have been performed to investigate the effect the energy of the x-ray beam has on the transmitted x-ray signal reaching the detector, and to assess the properties of the x-ray beam that determine image contrast.

4.1.1 Overview of the Monte-Carlo Simulations

Simulations of two different experimental models were performed using the BEAMnrc code. Each simulation specifies the component modules required to fully describe the experimental model such as, x-ray tube, filter, blood vessel and phase-space file. The interaction cross-sections of the materials used in the simulations (Figure 4.4, p.67), were chosen based on their suitability for simulating low energy photon interactions.

Simulated detection of iron fluorescence x-rays

The first simulation was performed to obtain the spectrum of x-rays transmitted through blood vessels containing different concentrations of iron. The transmission spectra show that the iron could be identified at high concentrations,

Water was added to the iron to simulate the human tissue. The transmission spectra show that the water absorption has superimposed the iron peaks, which have disappeared. These results suggest that techniques based on identifying iron, rather than using iodine contrast media, may not have the sensitivity required for clinical applications (see section 4.3.1, p77).

A disadvantage of Monte Carlo techniques is that large numbers of particles (histories) must be simulated to obtain data with sufficiently low statistical noise. Consequently, an important first step is to determine an optimal number of histories. To do this, the first simulation (to obtain transmission spectra through an iron sample) was run with histories ranging from 100,000 up to 1,000,000 for a 50kVp spectrum. Based on an analysis of data from these repeated simulations, I decided to use 1,000,000 histories for all subsequent simulation runs.

Simulated detection of iodine contrast material

The second simulation was performed to obtain the spectrum of x-rays transmitted through blood vessels containing iodine in different concentrations. In the simulations three detectors were placed. One of them was a slab of iodine. The other two was no iodine. The transmitted spectrum showed that the detector with the iodine slab had more absorption compared to the other detectors. Another simulation was run to identify the iodine peaks at different slab thicknesses where the iodine slab was increased gradually.

Simulations were performed to find the optimum x-ray tube energy for achieving high image contrast. To do this, x-ray exposures for the experimental model were simulated both with iodine and without iodine at different energies over the range

of 50 kVp to 120 kVp. The optimum energy was identified at 50 kVp (see section 4.3.5, p.103).

Using this optimum x-ray tube energy, the minimum concentration of iodine required was then identified for the same experimental mode. When the amount of iodine was increased the results showed that the minimum concentration was at about 6 to 8 mg/l (see section 4.3.6, p108).

The preliminary results showed the ability of the Monte Carlo code to simulate the x-ray, aluminium filter, blood vessel and the detector. The x-ray energy spectrum of iodine was defined and the iodine peaks could be seen clearly. From the analysis of those spectra, the simulations needed to be more realistic and the phase-space file that was used in all the simulations, needed to be similar to the materials of the Medipix detector.

4.2 Simulation methods used

BEAMnrc was used in this chapter to simulate the geometry of the x-ray source and the other component modules (CM) such as the filter, phantom and detector used in simulated clinical applications of the Medipix detector. The code has the ability of tracking each particle's history and, using this information, to analyse the scoring component modules so as to determine the x-ray spectrum and the x-ray fluorescence of iodine contrast medium.

This project used the Monte Carlo code to determine the iodine k-edge and come up with a setup to represent the blood vessel phantom and the Medipix detector. The output information was analysed to get the best concentration of iodine at the best energy to improve the contrast of angiography. An important aspect of the

project was to use Monte Carlo simulations of the photon beam to obtain detailed spectral information of the x-ray beam emitted by the x-ray tube, and absorbed by the Medipix detector after passing through a simulated object.

4.2.1 The BEAMnrc simulation system

Figure 4.1 represents the steps required to construct and run a simulation of an x-ray system with the BEAMnrc software. BEAMnrc reads in cross section data prepared by the PEGS package from the EGS4 system and the input file, which contains all the information related to that specific run. The output data listed in the phase-space data and the graphics requested and produce an output list.

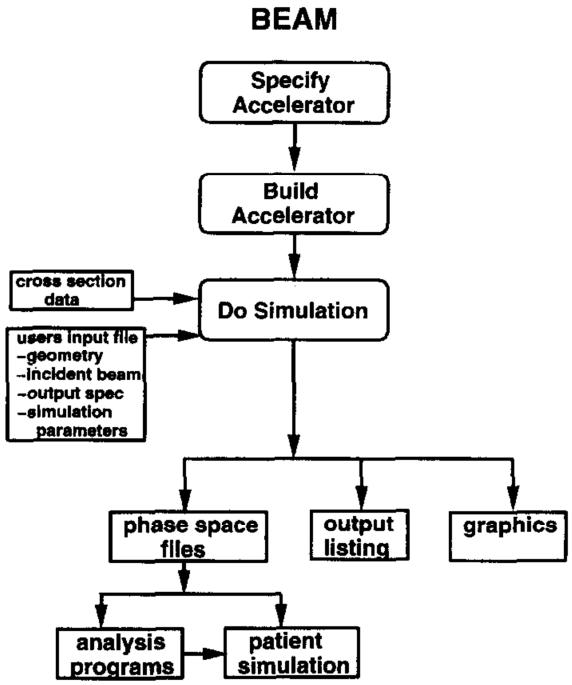

Figure 4.1 The layout of the simulation starting from the build-up of the CM end of with the output results.

The model is built up from a series of component modules: CM. Each CM operates completely independently of the other component models. All the CMs are placed along the z-axis direction at a right angle, to the beam axis. The model

allows calculating or testing each CM individually. The CM has many different designs that can be used in a wide range of configurations. The model does not allow the CMs to overlap each other and if it does by mistake, the run will not execute and will show ″error″. The EGS_Window package is used to display the geometry. It is linked to each of the CMs to visualise the designed geometry, and this display is set to help understand the designed geometry rather than give an accurate representation.

The available CM modules have been designed in a specific geometry. These may represent either generic geometry or a specific component of a radiotherapy linear accelerator, and include the following modules: SLABS, CONS3R, CONESTAK, FLATFILT, CHAMPER, PAYRAMIDS, APPSQ, JAWS, MIROR and XTUBE.

This project used the SLAB and XTUBE to simulate the x-ray source, phantom and detector. The SLAB is a simple generic CM module, it models parallel slabs in the x-y plane that can be of different materials with different thicknesses where the outside geometry is square. The XTUBE is used to model an x-ray tube as photon source and thus must be the first CM in any simulation configuration. It simulates the x-ray tube with several layers, the first layer represents the tungsten target and the second layer, which holds the target, is copper. The copper layer is used to remove heat from the target. The whole setup is in a vacuum. Parameters required to describe the x-ray tube and its operation can be set, such as, the tube energy, target angle and the cut-off energy of photons and dimension.

The output from the BEAM; BEAM has three major forms of output. The list file, phase-space data file and graphic output file which shows both the x-ray geometry and every step of the particles.

The list file; The list file contains records describing the simulation steps performed, which provide an accurate specification of the model, and may be used to reproduce a given simulation.

The list file also gives a summary of the region numbers for every CM and lists the geometry region with the different materials. In addition, it contains several standard outputs for each scoring plane, defined in the x-ray model. The number and widths of the scoring planes are listed at different regions. The final output shows the data of the complete run such as the energy deposited in an arbitrary number of zones and region.

The phase-space data file; the phase-space files contain the data about each individual particle crossing the scoring planes. The most important output depends on the application. The phase-space file is used to store all the output data from the simulation and record it. The file can be used with plotting software, such as Grace or Excel to plot the output data.

The BEAM code produces a phase-space file or output of the beam representing the position, energy direction, charge and history of each particle at any specific plane in the component modules. The phase-space data forms the end of the batch for all the scored plan or CM. It represents the calculation done in each CM, shows the calculation in separate runs, usually 10 runs, and then calculates the mean and variance of the mean.

The graphical output file; The EGS_Window graphical package allows showing the geometry for the component modules as set in the simulation. The run history to execute the data file should be set to 1000 histories to allow the EGS_Window

to display the geometry. If the history is set over 1000, the files called egsgeo and egsgph will not present. These files are necessary to run the EGS_Window package. The use of this plot is to make sure that the simulation is exactly as designed (Figure 4.2). The graphical package can display in three-dimensional space. It can also display the electron transport toward the target and the photons coming out of the target and hitting the component module and the scoring plane. The package allows changing the colour of the electrons and the photons so that they are easily distinguishable in the display (Figure 4.3).

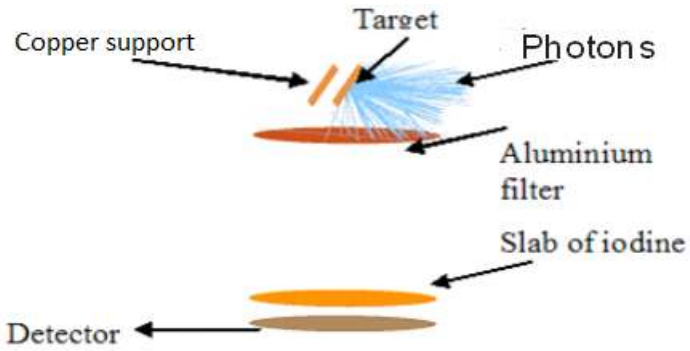

Figure 4.2 Geometry from EGS_Window graphical package show the x-ray's come out the target.

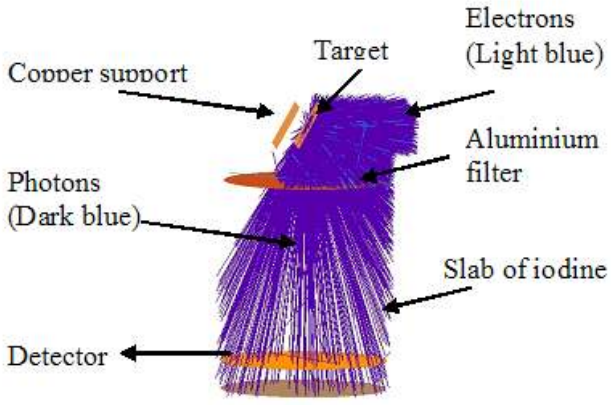

Figure 4.3 Geometry from EGS_Window graphical package shows the photos hitting the components module.

4.2.2 Design of simulation models used

The Monte Carlo simulation was used to simulate the target which is the x-ray, with 1mm Aluminium filter, blood vessel phantom and the detector (Figure 4.4).

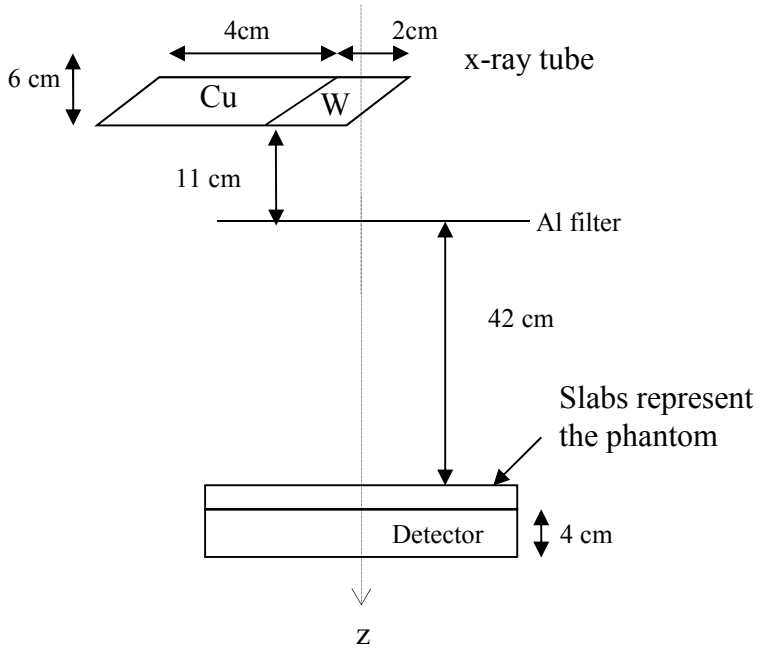

Figure 4.4 The setup used with Monte Carlo simulation

4.2.3 The Cross-Section Data - PEGS4

The cross section data for BEAMnrc is created by the code PEGS4. For information on running this code, see the EGS4 manual (Nelson *et al.*, 1985). PEGS4 data are included on the OMEGA distribution as two large data files.

The energy range is from the AE values of 521 or 700 keV up to 55 MeV in both cases. These data are based on the density effect corrections in ICRU Report 37 (ICRU., 1984). The data file has two files; one is 700icru.pegs4dat and the other is 521icru.pegs4dat. The first data file is used for a medium with high-energy cross-section while the second one is used for one of low energy.

This work simulation used the low energy cross-section data file because the simulation was based on using x-rays at low energy. The default file name of the cross-section data is 521icru.pegs4dat which had been corrected to use the material with different electron and photon energies. The new output file has been renamed as 521icru_mod.pegs4dat.

4.2.3.1 The BEAMnrc input parameters

The BEAMnrc is the graphical user interface windows, which allows the user to specify the model-mainly the accelerator. The window has three main options. The first option is the file that allows the user to specify new simulation, open previous simulation, change PEGS4 file, loading and saving input data. The second option is used to preview the simulation while the third option is to execute the file such as compiling the file and run the simulation file. Simulation had been set to create a new simulation, PEGS4. The file name window will prompt to specify the PEG4 cross-section data file to be used by browsing the HEN_HOUSE directory. The PEGS4 data "521icru_Mod.pegs4dat" was selected (see section 4.2.3, p. 67). The project specified in this BEAMnrc window created the simulation where the window allows setting the component modules that had been selected, such as x-ray tube and slab. After editing the main menu with the proper component modules, the simulation is saved. A small window will appear automatically to view the selected components.

The selected components' window has two main options. The first option allows the user to edit the main input parameters and the second option allows the user to edit every single component module individually. Firstly, I will explain the main input parameter. The main input data has two main options. The first is to edit the

main parameters for the simulation, the second to edit the EGSnrc parameters. The main input parameters for the project simulation were selected as follows:

Title: X-ray Tube was assigned as the title of this simulation.

Medium: Vacuum was selected to represent the region both about the central-axis and at the front or back of the component modules (CM).

IWATCH Output: This was set to one. Hence, the output lists every time an interaction occurs. If one changes the value of IWATCH to two, the output includes information on every single electron step and hence explodes dramatically in quantity. Finally, if one uses the code EGS Windows for doing a 3-D graphics display of EGS simulations, then IWATCH = 4 will write files for the input of this code. In this case, the numbers of histories should be set to 1000, otherwise the file cannot be written.

RNG Seed Option: The options were Random number generator, Store RNG at the start of each batch. Zero was used at the start of each history; means store RNG seed for the first history being simulated.

Run option: "First time" zero was used and means that this was first run for this data. BEAMnrc initiates a new run, deleting all of the output files from previous runs of the same name, if present. There are four other options that can be used for the parallel run.

Output Option: Phase space at each scoring plane is used for the input and output file.

Store Data Arrays: "No" was used: using "yes" stores data arrays for reuse of the data for the next run. Actually it will take time which prolongs the time of run.

LATCH option: "Non-inherited" latch used an integer variable to track histories and the option associated with each particle in the simulation. It used the bit variable to track the particle history and it had the opportunity to define a mapping of geometric regions.

Score last Z: Last interaction means to score the xyz- position of the last site of interaction in the file called egsgph which is used by EGS_Window to plot the 3-D geometry.

Number of histories: This parameter sets the number of histories to run for the simulation. The minimum allowed history is 100. 100,000 histories where used for most of the simulation runs, but if 3-D geometry requests the use with the EGS_Window, the number of histories should be set to 1000.

Initial RNG seed1 and **Initial RNG seed2** were set to 33 and 97 respectively.

Maximum CPU hours allowed: 0.99 hours means an estimate of how much time is needed to complete another batch. If the run is not completed within this time, the run will stop and the time needed to be increased or decreased depending on how much time is required for the run.

Bremsstrahlung Splitting: Bremsstrahlung splitting is a technique which can provide a factor of four or more improvements in efficiency when modelling beams generated by medical accelerators. The advantage of doing this splitting within the routine BREMS, is that various constants for the electron's energy are only calculated once and the sampling is therefore faster. When the option is set on "uniform", this means the Bremsstrahlung splitting is constant and is the same for all Bremsstrahlung events.

Split electron or photons at CM: "None" was selected. Splitting is designed primarily for photons and was originally introduced to allow splitting in phantoms placed at the bottom of an accelerator. In my case I did not think that I needed splitting.

Incident particle: "Electron" was selected as the type of source used in the simulation. The option allows the user to select electron, photon or positron.

Source number: This option allows the user to set the source number by selecting the type of source to use in the simulation. Then full details for each source can be edited as needed. Number 13, which is a parallel rectangular beam, incident from the side used in this work, simulated the x-ray tube. The new screen will open to allow the user to edit the specification of the source, the parameter set as follows; Ybeam=0.1, Zbeam=0.4, UINC=-1 and VINC=0. The source beam energy can also be specified. In this work, mono energetic is selected and the energy varied depending on the energy used in every run. The option allows one to load spectrum from a specified file if it is available.

Global electron cutoff energy-ECUT (MeV): 0.511 MeV was selected, where the global cutoff energy for electron transport in MeV, as soon an electron total energy falls below the cutoff energy, its history is terminated and its energy deposited in the current region. The time required for a given calculation strongly depends on the value of ECUT and thus it is important to use as high a value as possible.

Global photon cutoff energy-PCUT (MeV): 0.001 was selected, where PCUT defined the global cutoff energy for photon transport in MeV. The photon is the same as the ECUT.

Electron range rejection: Set to "off". It was used to save computing time during simulations.

Photon forcing: "on" selected as this option allowed forcing photons to interact in specific component modules within a simulation, where this option was useful for improving statistics of scattered photons. In addition, the other purpose was to study the generation of contaminant electrons in a photon beam. The option will open another window which allows one to set the type of forcing. There were three options; firstly force photon interactions from interaction one: this was set to one; secondly start photon interaction forcing at CM: number was set to 1 and thirdly stop photon interaction forcing after CM: number was set to 4.

Number of scoring planes: was set to "1", to set the number of fluence scoring planes that can be used with this option. The planes are always at the back of a CM, so it should be specified which CM to place the plane behind, as well as specified the number of scoring zones within the scoring plane. A new window will open to allow one to set the scoring plane and the number of scoring zones. The CM number for plane1 was set to "4", number of scoring zones was set to "4" and the zone type was set to annular.

Dose calculation: was set to "only total dose",

Z of front of 1st CM to reference plane: was set to "0.0", which represents the Z coordinate of the front surface for the first component modules. This includes any air gap and defines the position of the front of the model.

As I mentioned previously the second option at the main input window is the EGSnrc parameter, which was set as follows:

Maximum step size (cm): Defines the maximum electron step length in cm. It was set to 5 to ensure proper electron transport in low density materials (air).

Max. Fractional energy loss/step: was set to 0.25. This defines the maximum fractional energy loss per electron step. For accurate electron transport with default EGSnrc electron step algorithm, it should not exceed 0.25 (the default).

Ximax: was set to 0.5. This defines the maximum first multiple elastic scattering moments per electron step. It is equal to roughly half the average multiple scattering angles, squared. It should not be set greater than1, since this is beyond the range of available multiple scattering data. The default value of 0.5 should be sufficient for most applications.

Boundary crossing algorithm: was set to PRESTA-I, This controls the algorithm used to transport electrons across region boundaries. It is mainly used for the dose calculation.

Skin depth BCA: was set to 0

Electron-step algorithm: was set to PRESTA-II. This input determines the algorithm used to calculate lateral and longitudinal corrections. These account for elastic scattering in a condensed history electron step. There are two possible settings: PRESTA-II (the default) and PRESTA-I. PRESTA-II, the new, more

accurate algorithm developed for use with EGSnrc (Kawrakow and Rogers, 2000). PRESTA-I may be accurate enough for high energies (since elastic scattering is weak), but it is not recommended for low energy applications.

Spin effects: was set to "on" (the default), that means that the elastic scattering cross-sections which take into account relativistic spin effects, are used in electron transport. Using "on" will increase calculation time, but, the results are more accurate and it is necessary for good backscatter calculations.

Electron impact ionization: was set to off, if on it will use the Kawrakow EII theory, but here the theory was not used.

Brems angular sampling: was set to Simple (default), this input determines the type of angular sampling that is done when a Bremsstrahlung photon is created.

Bres cross-sections: was set to BH (default). This input determines the differential cross-section used for Bremsstrahlung interactions. The Bethe-Heitler cross-sections (Coulomb corrected above 50 MeV) are used, because the difference between the two options is not important at energies greater than 10 MeV, but become significant in the keV energy range.

Bound Compton scattering: was set to "on", The Bound Compton scattering input is used to determine whether binding effects and Doppler broadening are simulated in Compton (incoherent) scattering events.

Pair angular sampling: was set to "simple". This input determines the method used to sample the positron/electron emission angles (relative to the incoming photon) in a pair production event.

Photoelectron angular sampling: was set to on. The photoelectron angular sampling input determines the sampling method used by EGSnrc to determine the angle of emission of photoelectrons.

Rayleigh scattering: was set to "off". This input determines whether Rayleigh (coherent) scattering is simulated or not. Rayleigh scattering is only recommended for low energy less than 1MeV simulations.

Atomic relaxations: was set to "on". This input determines whether the relaxation of atoms to their ground, state after Compton and photoelectric events is simulated. The relaxation after Compton and photoelectric events is simulated via the emission of any combination of K-, L-, M- and N-shell fluorescent photons, Auger electrons and Coster-Kronig electrons. The lower energy limit for relaxation processes is 1 keV. Thus, only relaxation in shells with binding energy greater than 1 keV is simulated.

Photon cross-section: was set to Storm-Israel (PEGS4) (default), to determines which photon cross-section would be used.

The second option in the selected components option mentioned above is to allow the user to edit each component module CM individually. This work used four component modules; XTUBE was used to simulate the x-ray tube, SLAB code was used to simulate three models in the simulation, such as filter, iodine and phase-space (represent the detector) respectively.

Input parameter using XTUBE code; A component module must be the first component module for simulating an x-ray tube. XTUBE is usually the first CM in a beam model, and the source beam is usually incident on XTUBE from the

side. The second CM may be any of the available CM with a central opening serving as the exit window of the x-ray tube. The target of the xtube may have an arbitrary number of layers, each with a different thickness and medium. XTUBE has square symmetry.

The parameters used with the XTUBE in this work are tungsten as a target, 2cm thick, mounted on a copper holder. The target is angled at 20 degrees with respect to the z-axis. It spans 6 cm in the z direction. The medium in front of the target is AIR. ECUT and PCUT for all regions are set to 0.521, 0.001 respectively. The input file specifies the target to start at 10cm from the reference plane.

Drawing 1: XTUBE component module with two layers in the target (N=2). The angle of the target relative to the Z-axis is given by ANGLEI. The thickness of a target layer i is given by DTHICK(i). The target is positioned so that the front of the target (layer 2 in the figure) intersects with the beam at the central (Z) axis. Target layers are arranged with the front of layer i-1 flush with the back of layer i. The target and target holder extend to RMAX_CM in the Y-direction. MED3 in the figure above would usually be air or vacuum, but could be any material. MED4 specifies the material of the target holder.

Input parameter using SLAB code; SLABS are used for multiple planes of arbitrary thickness and material, a set of semi-infinite slabs. One single slab is a special case for SLABS. SLABS have square symmetry about the beam axis. The slabs in this work were used to represent the filter, tissue (water), iodine (blood vessel) and phase-space (detector). The parameter was set for the filter and was defined as 0.001 cm thick slabs of aluminium. The front slab is at Z=11 cm. Electrons were followed in the slabs down to kinetic energies of 0.511 MeV and

photons were followed down to energies of 0.01 MeV. The dose deposited in the air scored these regions in dose zone 1, because the filter in this work used only one layer of the SLAB code.

Iodine is defined with a slab of different thicknesses depending on the simulation used for different setup of iodine. The front slab was at Z=16.001cm. Electrons were followed in the slabs down to kinetic energies of 0.511 MeV and photons were followed down to energies of 0.001 MeV. The dose deposited in the air will be scored in these regions in dose zone 1, because the iodine in this work used only one layer of the SLAB code.

Phase-space file (represent the detector) is defined as a 4 cm thick slab of air (silicon was used in another experiment to represent the detector material). The front slab is at Z=42.01 cm. Electrons will be followed in the slabs down to kinetic energies of 0.511 MeV and photons will be followed down to energies of 0.001 MeV. The dose deposited in the air, will be scored in dose zone 1, because the air in this experiment used only one layer of the SLAB code.

4.3 Results and discussions

4.3.1 Identifying iron fluorescence peaks

Photon-induced x-ray fluorescence has been used to determine elements in human whole blood samples (Borjesson et al., 2003). The method is reliable and has a good sensitivity for a wide range of elements. Extending this idea to spectral imaging has led to the proposal in this project to detect the iron present in the blood rather than detecting an injected iodine contrast agent. The obvious advantage of this method is that iron is one of the contents of human blood, and is

distributed in the blood vessels of the human body. If this approach is successful injections of (iodine) contrast agent into the patient would no longer be necessary for imaging blood vessels. The importance of this is that the (substantial) health risks to the patient (Chezmar *et al.*, 1990) that are associated with the use of injected contrast agent are eliminated. Consequently, the method would be a clinically important development.

The Monte Carlo code was used to simulate the model shown previously in Figure 4.4. This model comprises a slab of iron exposed to x-rays at 50 kVp, and a slab of air representing the detector (output data is captured from the air slab CM). The first run was performed without the iron slab to obtain the spectrum of the x-ray beam at 50 kVp for 100,000 histories, which is shown in Figure 4.5.

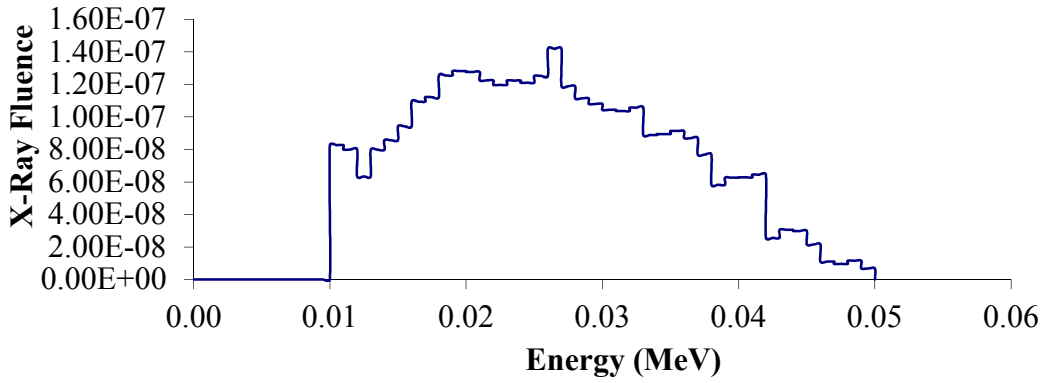

Figure 4.5 Simulated x-rays fluence for an x-ray tube operated at 50 kVp.

The second run was performed using a 0.1 mm thick slab of iron with an x-ray tube voltage of 50 kV_p, using a cutoff energy[2] of 50 keV. The fluorescence x-ray peaks for iron at 7.1 and 9.2 keV, can be clearly seen in the simulated spectrum (Figure 4.6):

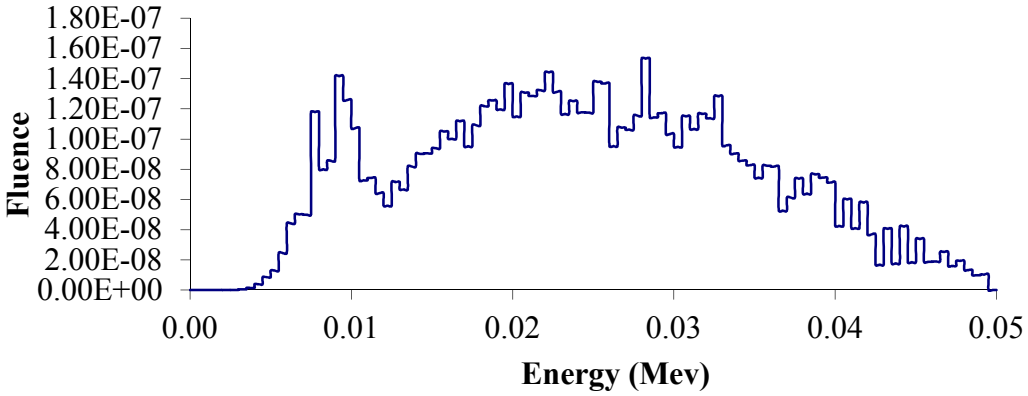

Figure 4.6 Energy fluence distribution for iron at slab thickness 0.0001 cm

The run was repeated for different thicknesses of iron ranging from 0.0001 cm up to 0.03 cm (Figure 4.9). It is obvious that the iron fluorescence x-ray peak becomes clearer as the thickness of the iron slab is increased. Figure 4.7 (next page) shows the area under the iron peak ratio versus the iron thickness. Where the area under the peak ratio, which is defined by dividing the absorption under the peak between energy range of 8-10 keV by the absorption under the peak between energy range of 5-7 kVp, is observed to decrease with increasing thickness of the iron slab. This result shows that although the iron is emitting fluorescence x-rays, most of the low energy photons in the spectrum are absorbed.

[2] Initially the simulated spectrum did not show any signal below 10 keV. The reason for that was that the default EGS data cut-off energy for the electron and photon was set at 10 keV. Simulation parameters appropriate for low energy medical imaging (5 keV to 120 keV) are required.

The quantity of iron in this simulation is much greater than the quantity of iron in the blood.

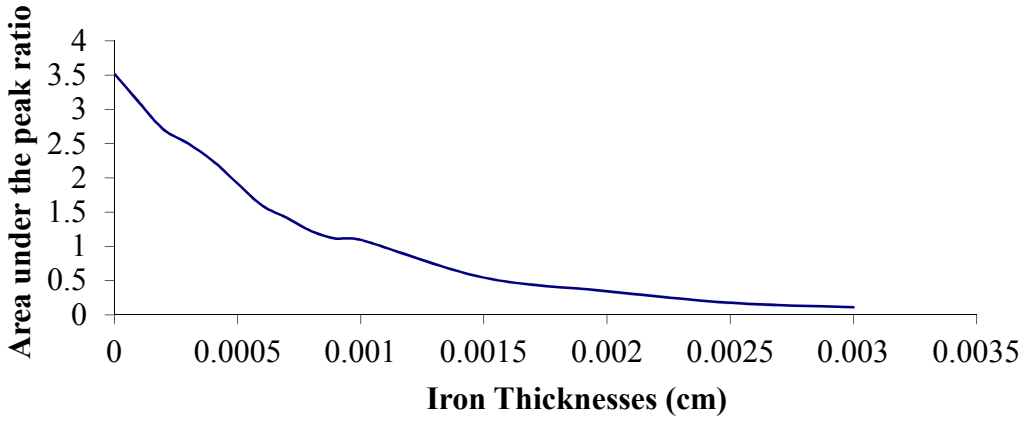

Figure 4.7 Ratio versus iron thickness.

The simulation was repeated with water added to the model to represent human tissue surrounding the blood vessels. In this simulation the iron peaks completely disappeared due to the high attenuation of low energy photons in water (Figure 4.8). This demonstrates that detecting and iron in small quantities by identifying iron absorption peaks in the spectrum is not practical, especially when water (simulating human tissue) is present. The human blood vessels are located deep under the body tissue and maybe under the bone, which makes it impractical to detect the iron in blood. Therefore, these results suggest that imaging methods utilising detection of iron fluorescence x-rays or changes in x-ray transmission at the k-edge of iron present in blood instead of iodine contrast media is impractical.

In addition, the high attenuation of low energy photons observed in Figure 4.8 suggests that there is a practical lower energy limit of 15 – 20 keV for acquiring the image signal.

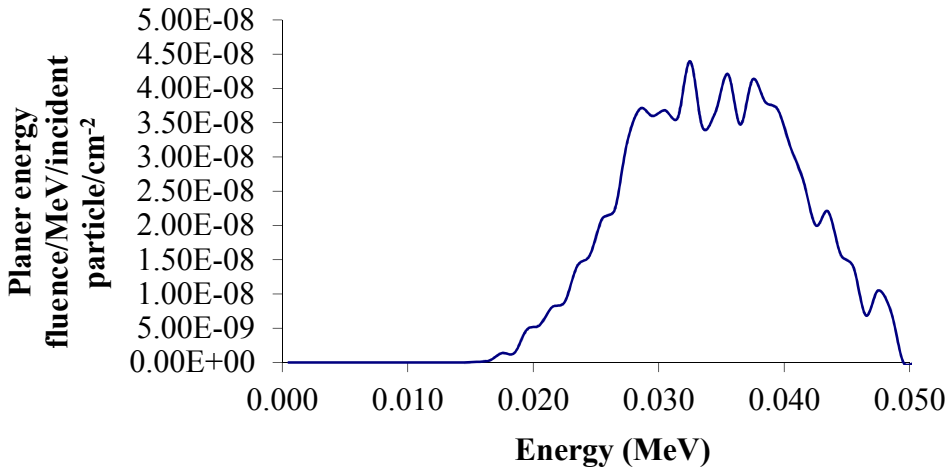

Figure 4.8 Planer energy fluence distribution simulated using a 0.02 cm iron slab with water. Note that there is no signal from the iron characteristic x-rays at 7.1 and 9.2 keV due to attenuation by water.

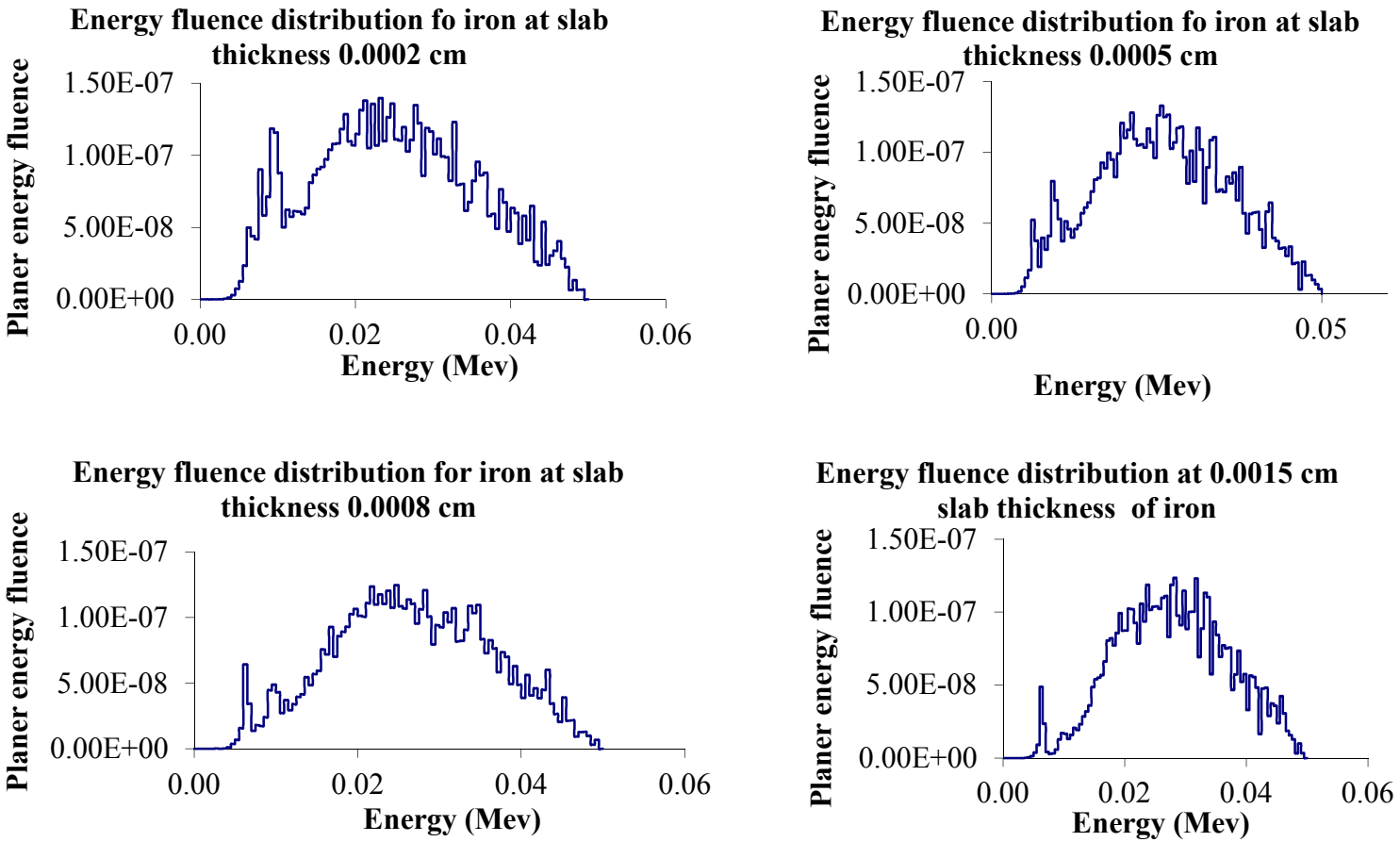

Figure 4.9 Energy fluence distribution for iron at slab thickness from 0.0002cm to 0.0015cm

4.3.2 Identifying parameters for obtaining high contrast images using iodine

The aim in this section was to identify parameters for obtaining images with (high) contrast to noise while using low concentrations of iodine contrast media. In dual energy angiography, image contrast is provided by the difference between the absorption of the spectrum transmitted through the object in two exposures, firstly without iodine contrast media, and then with iodine. Spectral information provides the potential to acquire images in a single exposure at energy ranges above and below iodine k-edge, which may be subtracted to provide high contrast angiography images. Identifying, a large difference in absorption between these images can be used to demonstrate the utility of the technique

The spectra were analysed to prove the use of iodine contrast media. The same setup was used by adding a slab of water in the first setup. The water slab was added in two layers; hence the water level increased both from above and below. The run was made at different distances from the detector. In the second setup, the slab of iodine was added in between the water slab to represent the blood vessel. The detector was placed at the lower end of the simulation

Simulation 1: The simulation model (shown in Figure 4.10) uses a slab of 4cm of water as medium, which represents body tissue. Initially, the simulation was run for 100,000 histories using an x-ray tube voltage of 50 kVp and an object to detector distance of 1cm. The simulation was repeated for object to detector distances of 2cm and 3cm. The simulated x-ray beam fluence at the detector is shown in Figure 4.10.

This simulation was repeated for 1,000,000 histories (using the same parameters). The simulated x-ray fluence from these repeated runs are shown in Figure 4.11, 4.12 and 4.13.

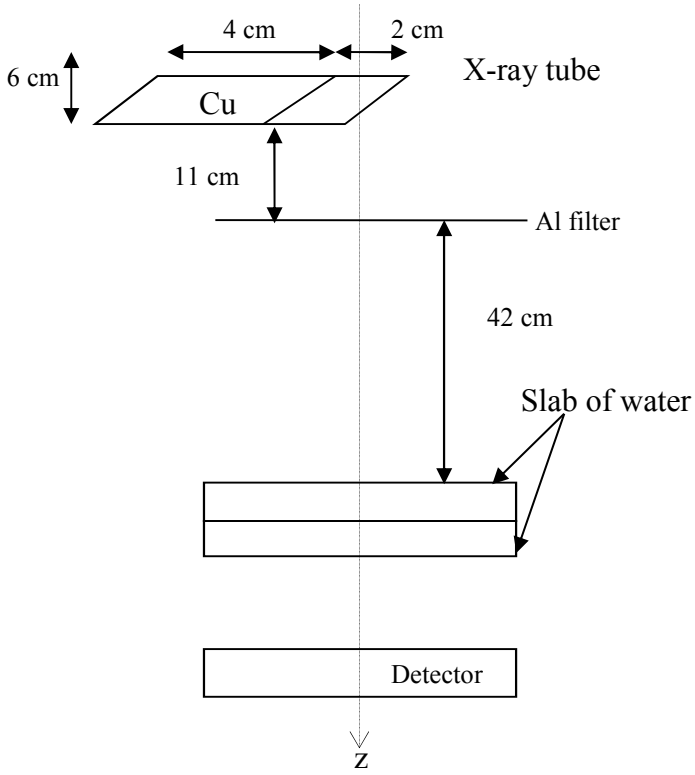

Figure 4.10 Simulation 1: represents the x-ray tube, slab of water representing the body tissue and the detector.

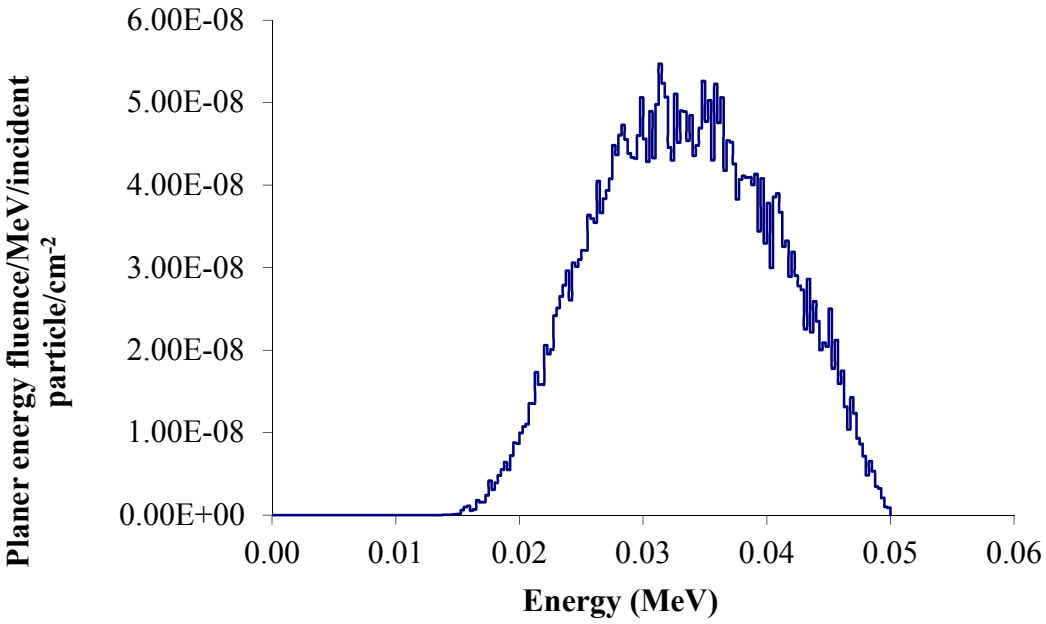

Figure 4.11 Planer energy fluence at 50 kVp of 4 cm water slab placed at 1 cm distance from the detector, the run made with 1,000,000 histories.

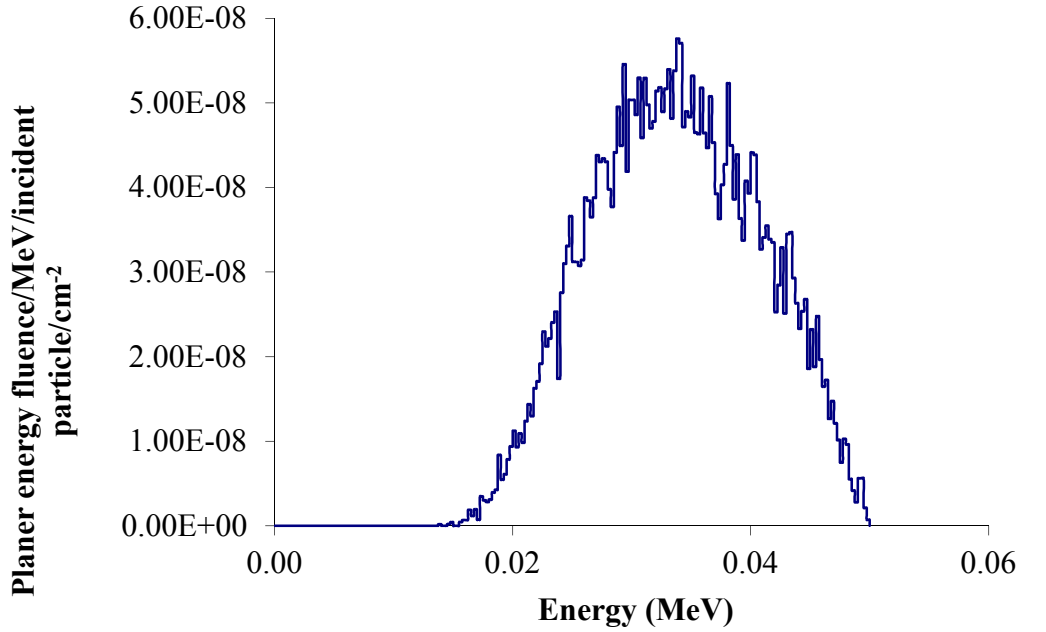

Figure 4.12 Planer energy fluence at 50 kVp of 4 cm water slab placed at 2 cm distance from the detector, the run made with 1,000,000 histories.

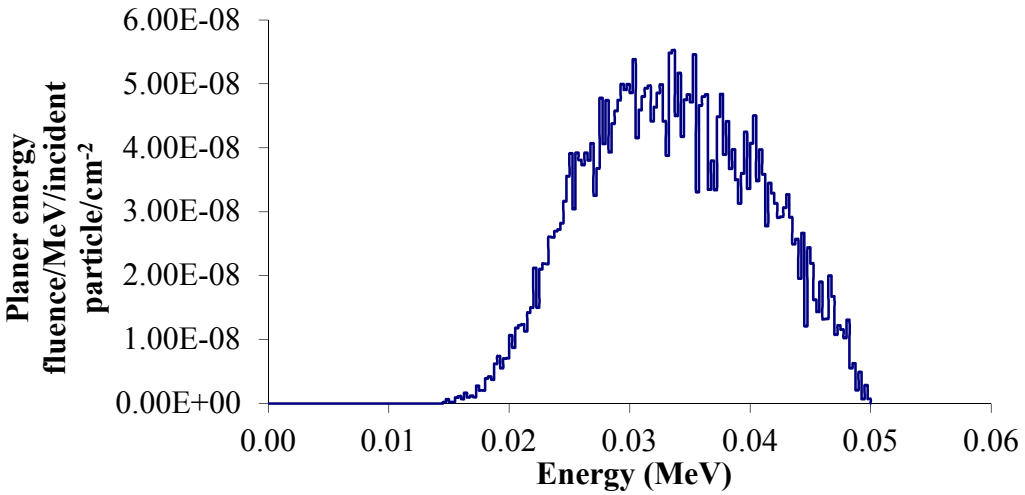

Figure 4.13 Planer energy fluence at 50 kVp of 4 cm water slab placed at 3 cm distance from the detector, the run made with 1,000,000 histories.

Simulation 2: This simulation used the same parameters as Simulation1 but with the addition of a 0.0002 cm slab of iodine (Figure 4.14). The simulation was run using 1,000,000 histories with the slab positioned at distances of 1 cm, 2 cm and 3 cm from the detector. The simulated x-ray fluences are shown in Figures 4.15, 4.16 and Figure 4.17 respectively.

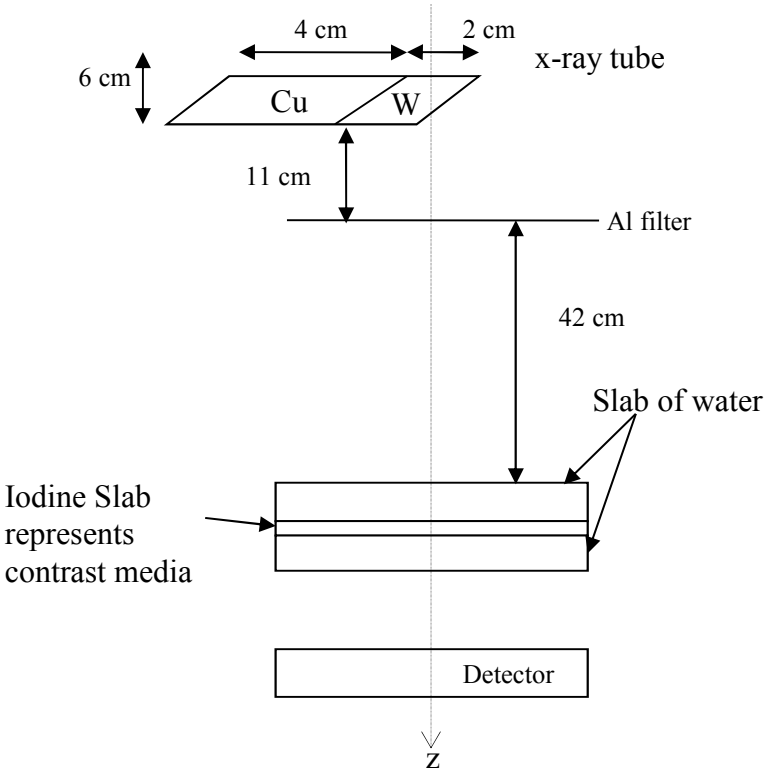

Figure 4.14 Simulation 2: represents the x-ray tube, slab of water representing the body tissue, slab of iodine representing the contrast media and the detector.

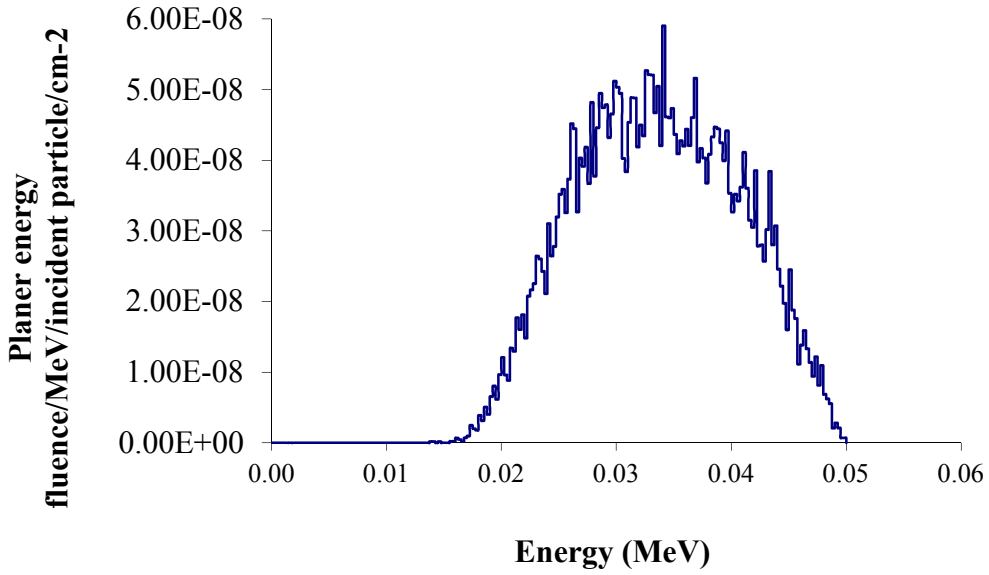

Figure 4.15 Planer energy fluence at 50 kVp of two slabs of 4 cm water slab on top of 0.0002 cm of iodine slab attached and placed at 1 cm distance from the detector, the run made with 1,000,000 histories.

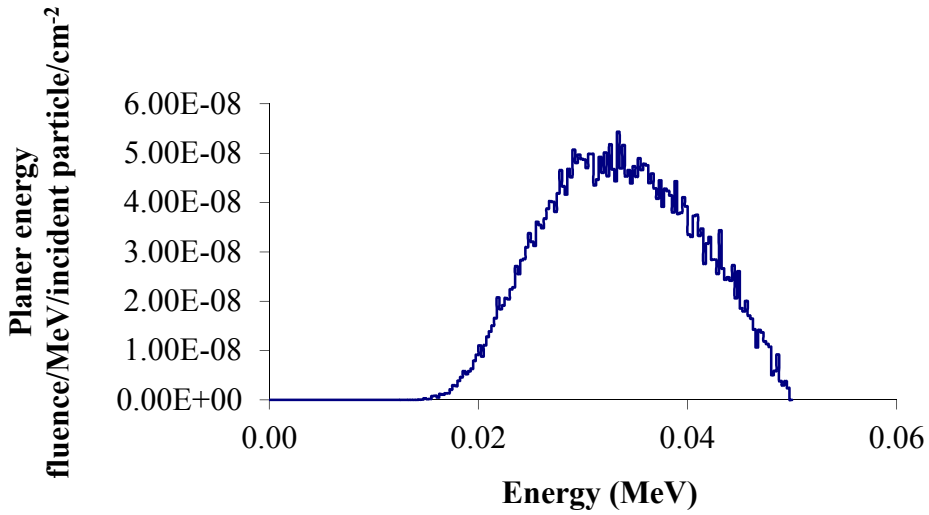

Figure 4.16 Planer energy fluence at 50 kVp of two slabs of 4 cm water slab on top of 0.0002 cm of iodine slab attached and placed at 2 cm distance from the detector, the run made with 1,000,000 histories.

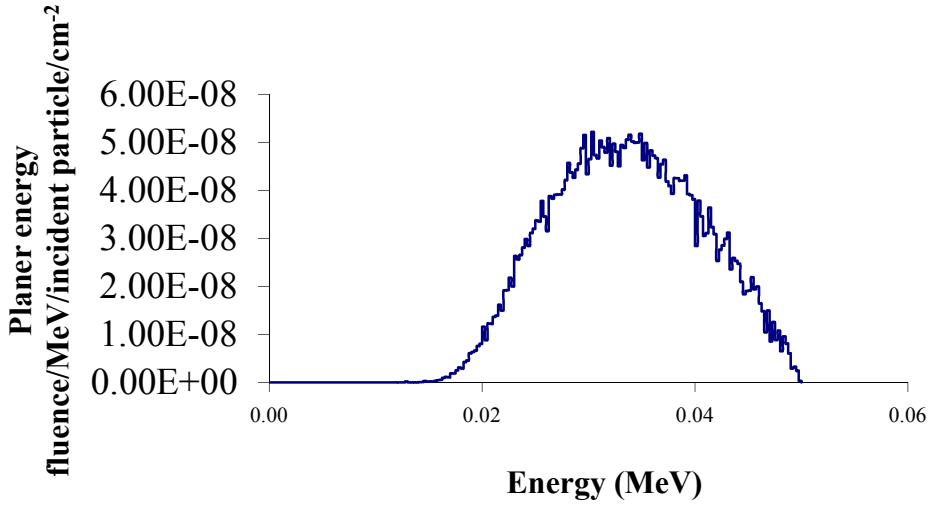

Figure 4.17 Planer energy fluence at 50 kVp of two slabs of 4 cm water slab on top of 0.0002 cm of iodine slab attached and placed at 3 cm distance from the detector, the run made with 1,000,000 histories.

Simulation 3: The final simulation, uses a 0.001 cm iodine slab positioned 1 cm from the detector, and repeated for distances of 2 cm and 3 cm. The simulated x-ray fluence from these simulations is shown in figures 4.18, 4.19 and 4.20 for simulations using 1,000,000 histories.

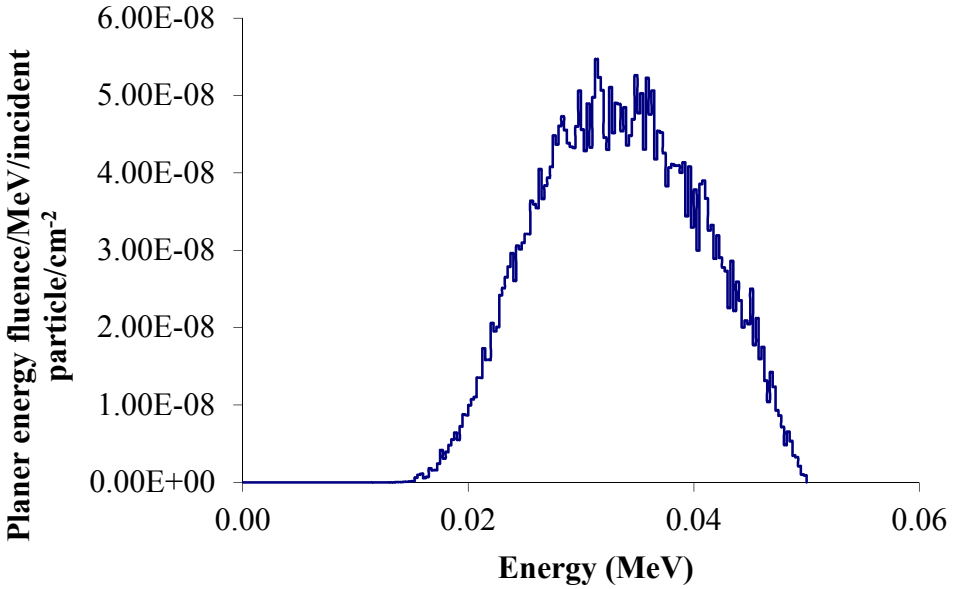

Figure 4.18 Planer energy fluence at 50 kVp of two slabs of 4 cm water slab on top of 0.001 cm of iodine slab attached and placed at 1 cm distance from the detector, the run made with 1,000,000 histories.

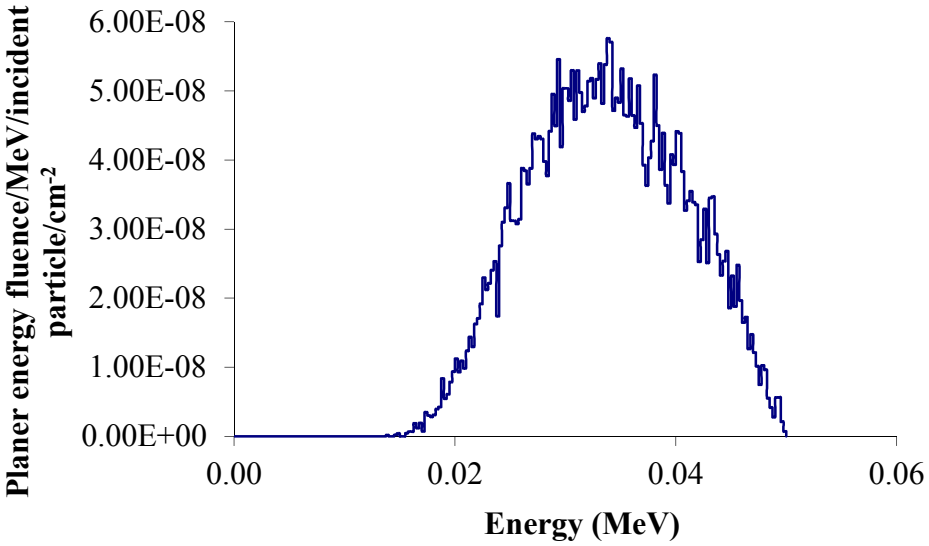

Figure 4.19 Planer energy fluence at 50 kVp of two slabs of 4 cm water slab on top of 0.001 cm of iodine slab attached and placed at 2 cm distance from the detector, the run made with 100,000 histories.

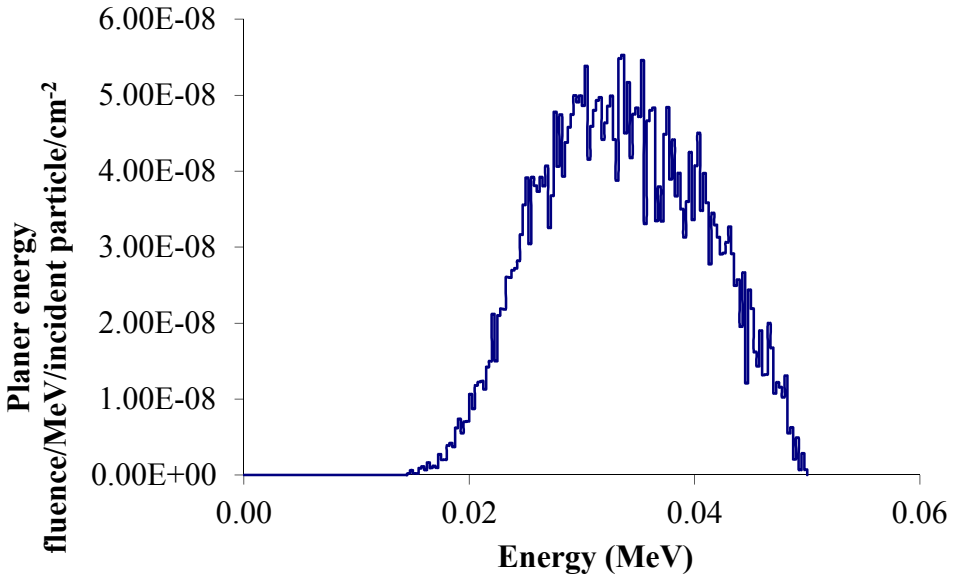

Figure 4.20 Planer energy fluence at 50 kVp of two slabs of 4 cm water slab on top of 0.001 cm of iodine slab attached and placed at 3 cm distance from the detector, the run made with 100,000 histories.

The spectra were made without iodine and at different histories. They were identified by having the peak ratio of the integral fluence under the spectrum peaks of water, having energy between (15-32 kVp) and (32-49 kVp) (Table 4.1). It was expected to see absorption increases with increasing the distance between the phantom and the detector. At 1 cm and 2 cm the absorption increased but at 3 cm it decreased, though the difference was not so big (Figures 4.21 and 4.22). Actually more points were needed to get acceptable information. By adding the 0.0002 cm slab of iodine, the absorption decreased with increasing the detector distance. The simulation needed to have more points to get acceptable information.

From Figure 4.23 it is obvious that the variation between the ratios of integral fluence is very small. However, the difference between the spectrum of water and the spectrum with the iodine slab was notable. That meant that we could easily separate the peaks having iodine from those without it. That is useful in getting the benefits of identifying the k-edge of the iodine and using them in subtracting the image in order to have good contrast image in angiography imaging

Table 4.1 The integral fluence of the simulated x-ray beam with and without the iodine at 50 kVp, the spectrum peaks is identified.

Distance between the detector and vessel (cm) with 100,000 histories	**Area(15-32 keV)**	**Area(32-49 keV)**	**Peak ratio**
1	4.09E-10	5.22E-10	1.28
2	4.17E-10	5.06E-10	1.21
3	3.96E-10	5.06E-10	1.28
Distance between the detector and vessel with iodine 0.0002 (cm)			
1	4.58E-10	5.61E-10	1.23
2	4.16E-10	5.60E-10	1.35
3	4.48E-10	5.09E-10	1.14
Distance between the detector and vessel with iodine 0.001 (cm)			
1	4.38E-10	4.89E-10	1.12
2	3.99E-10	5.08E-10	1.27
3	4.22E-10	4.78E-10	1.13
Distance between the detector and vessel with iodine 0.001 (cm) with 1000k histories			
1	4.08E-10	4.94E-10	1.21
2	3.97E-10	4.79E-10	1.21
3	4.07E-10	4.91E-10	1.21
Distance between the detector and vessel (cm) with 1000k histories			
1	4.30E-10	5.42E-10	1.26
2	4.24E-10	5.76E-10	1.36
3	4.24E-10	5.44E-10	1.28
Distance between the detector and vessel with iodine 0.00002 (cm) with 1000k histories			
1	4.21E-10	5.51E-10	1.31
2	4.26E-10	5.50E-10	1.29
3	4.25E-10	5.512E-10	1.30

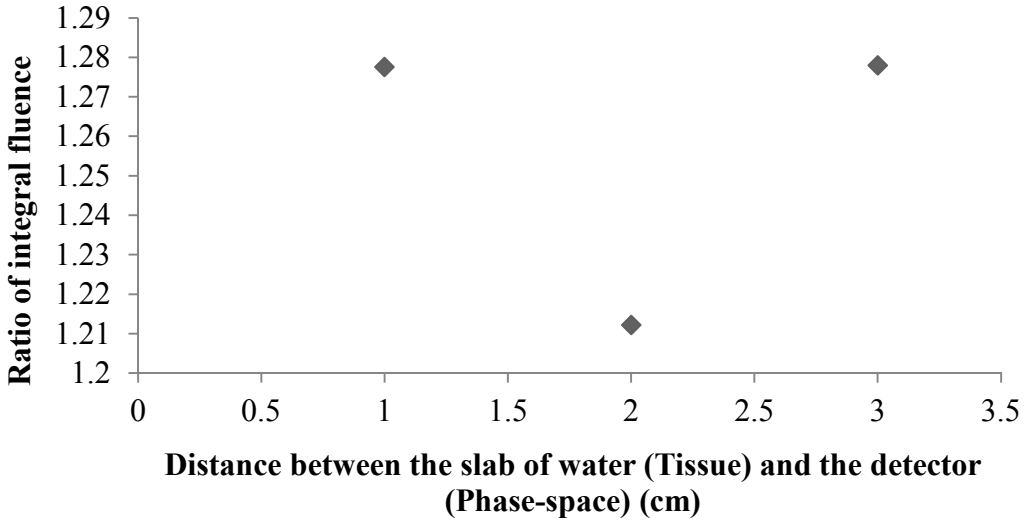

Figure 4.21 The peak ratio of the integral fluence under the spectrum peaks of water having energy between (15-32 kVp) and (32-49kVp) run with 100,000 histories.

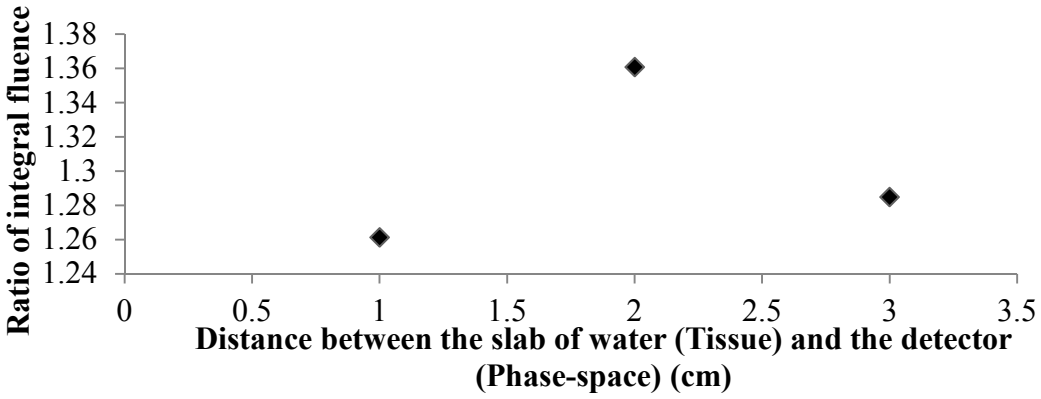

Figure 4.22 The peak ratio of the integral fluence under the spectrum peaks having energy between 15-32 kVp and 32-49 kVp run with 1,000,000 histories.

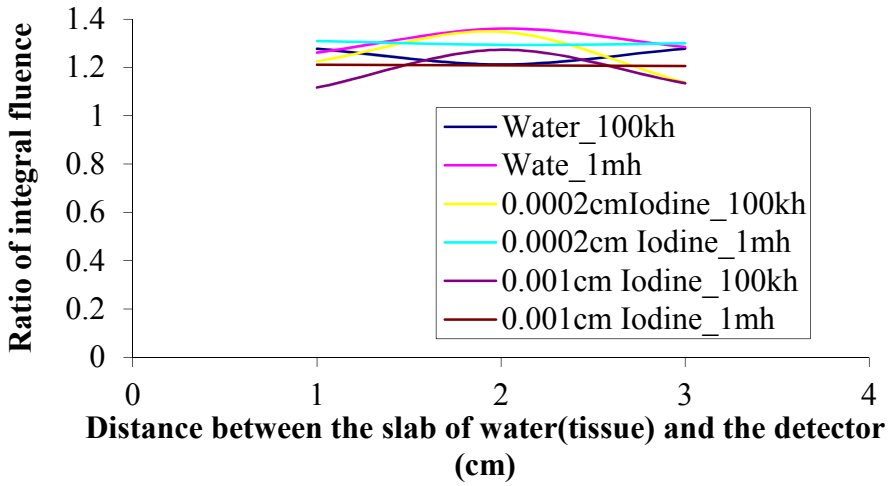

Figure 4.23 Composite plot, showing the difference between the slab with and without iodine at different vessel-detector distance and at different number of histories.

4.3.3 Simulating the effect of x-ray attenuation by water on the transmitted x-ray beam

X-ray spectra at the water surface were measured by using an air medium as a detector. The measurement was made using x-ray beam energy of 50 kVp, an aluminium filter, and a slab, which was placed on the top of the detector, having a thickness that was varied from 2 to 20 cm.

The first simulation was made using an iodine slab without water. The run was made at 100,000 histories and the spectra were defined. The integral fluence was obtained at the iodine peaks, between the energy ranges of 28-32 kVp and 33-40 kVp (Table 4.2). The peak ratio of the integral fluence was calculated and plotted. It was obvious that the spectrum sloped down until it reached 0.005 cm and the curve became flat. That meant there was not much change, while the absorption was almost the same (Figure 4.24).

Table 4.2 The integral fluence of iodine slab at various thicknesses

Iodine thickness (cm)	Integral fluence of iodine between 28-32 keV with iodine					Integral fluence of iodine between 33-40 keV with iodine					Peak ratio
	X1	X2	Y1	Y2	(Y2-Y1)/ 2*(X2-X1)	X1	X2	Y1	Y2	(Y2-Y1)/ 2*(X2-X1)	
0	0.028	0.32	1.11E-07	1.06E-07	3.17E-08	0.033	0.037	8.88E-08	7.67E-08	3.31E-10	1.04E-02
0.001	0.028	0.32	1.06E-06	9.19E-07	2.89E-07	0.033	0.037	7.04E-07	6.28E-07	2.67E-09	9.21E-03
0.005	0.028	0.32	1.34E-07	9.60E-08	3.36E-08	0.033	0.037	4.72E-08	4.54E-08	1.85E-10	5.50E-03
0.006	0.028	0.32	1.26E-07	9.60E-08	3.24E-08	0.033	0.037	4.67E-08	4.13E-08	1.76E-10	5.43E-03
0.007	0.028	0.32	1.13E-07	8.34E-08	2.86E-08	0.033	0.037	4.49E-08	3.28E-08	1.55E-10	5.43E-03
0.008	0.028	0.32	1.28E-07	7.98E-08	3.04E-08	0.033	0.037	3.51E-08	2.92E-08	1.29E-10	4.23E-03
0.009	0.028	0.32	1.21E-07	8.52E-08	3.01E-08	0.033	0.037	3.64E-08	2.66E-08	1.26E-10	4.18E-03
0.01	0.028	0.32	1.24E-07	7.67E-08	2.93E-08	0.033	0.037	3.33E-08	2.52E-08	1.17E-10	4.00E-03
0.015	0.028	0.32	1.01E-07	6.82E-08	2.48E-08	0.033	0.037	2.53E-08	9.99E-09	7.05E-11	2.85E-03
0.02	0.028	0.32	7.92E-08	5.40E-08	1.94E-08	0.033	0.037	2.03E-08	5.97E-09	5.25E-11	2.70E-03
0.025	0.028	0.32	5.79E-08	4.67E-08	1.53E-08	0.033	0.037	1.91E-08	3.26E-09	4.48E-11	2.93E-03
0.03	0.028	0.32	5.31E-08	4.53E-08	1.44E-08	0.033	0.037	1.50E-08	1.12E-09	3.21E-11	2.24E-03

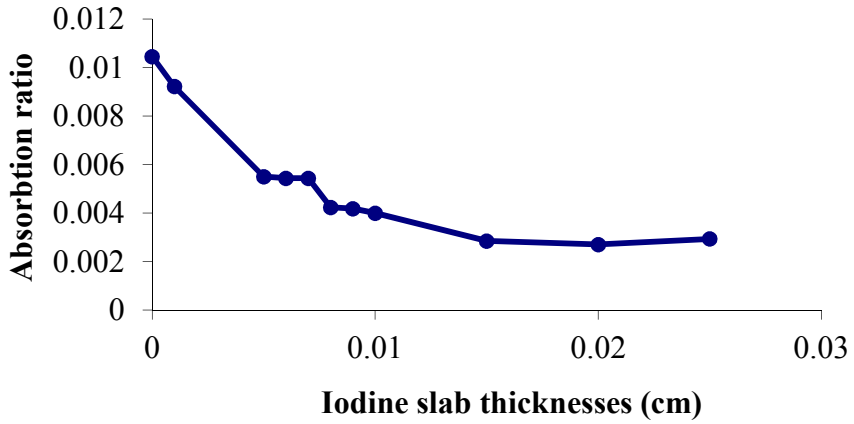

Figure 4.24 The absorption ratio at 50 kVp of iodine slab placed on the detector the run made with 100,000 histories.

The second simulation was made using a slab of water media representing the body's tissues and placed on the top of the detector.

The iodine slab was placed between the water slabs and the detector. The integral fluence was obtained at the iodine peaks, between the energy ranges of 28-32 kVp and 33-40 kVp (Table 4.3). Adding the water slab to the simulation lead to the absorption of the x-ray spectrum. The results of increasing the water level and varying the iodine slab thickness are shown in. The spectra showed little change when water was added although the absorption increased. It is clearly seen that the spectra slope down at the end of the tail (Figure 4.25).

Table 4.3 The integral fluence of iodine slab at various thicknesses with water added on top of the detector at various levels.

Iodine (cm)	Water level (cm)	Integrated fluence of iodine between 28-32kVp							Integrated fluence of iodine between 33-40kVp							Ratio
		X1	X2	X2-X1	Y1	Y2	(Y2+Y1)/2	(Y2-Y1)/2*(X2-X1)	X1	X2	X2-X1	Y1	Y2	(Y2+Y1)/ 2	(Y2-Y1)/2*(X2-X1)	
0.001	2	0.03	0.32	0.29	1.06E-07	9.418E-08	1E-07	2.92E-08	0	0	0	7.54E-08	6.507E-08	7.022E-08	2.8088E-10	0.00962
0.001	4	0.03	0.32	0.29	1.07E-07	9.597E-08	1E-07	2.966E-08	0	0	0	7.76E-08	6.507E-08	7.134E-08	2.8536E-10	0.00962
0.001	8	0.03	0.32	0.29	1.08E-07	9.597E-08	1E-07	2.972E-08	0	0	0	7.85E-08	6.193E-08	7.022E-08	2.8088E-10	0.00945
0.001	10	0.03	0.32	0.29	1.18E-07	9.328E-08	1.1E-07	3.083E-08	0	0	0	7.54E-08	6.597E-08	7.067E-08	2.8267E-10	0.00917
0.001	12	0.03	0.32	0.29	1.18E-07	9.283E-08	1.1E-07	3.077E-08	0	0	0	7.4E-08	6.597E-08	7E-08	2.7998E-10	0.0091
0.001	14	0.03	0.32	0.29	1.14E-07	8.656E-08	1E-07	2.926E-08	0	0	0	7.31E-08	6.104E-08	6.708E-08	2.6834E-10	0.00917
0.001	16	0.03	0.32	0.29	1.19E-07	9.328E-08	1.1E-07	3.097E-08	0	0	0	7.09E-07	6.373E-08	3.863E-07	1.5453E-09	0.0499
0.001	18	0.03	0.32	0.29	1.19E-07	8.791E-08	1E-07	3.025E-08	0	0	0	7.49E-08	6.507E-08	7E-08	2.7998E-10	0.00926
0.001	20	0.03	0.32	0.29	1.11E-07	8.88E-08	1E-07	2.913E-08	0	0	0	7.45E-08	6.417E-08	6.932E-08	2.773E-10	0.00952
0.005	2	0.03	0.32	0.29	1.34E-07	0.0000001	1.2E-07	3.417E-08	0	0	0	4.85E-08	4.492E-08	4.671E-08	1.8683E-10	0.00547
0.005	4	0.03	0.32	0.29	1.36E-07	9.955E-08	1.2E-07	3.443E-08	0	0	0	4.76E-08	4.313E-08	4.536E-08	1.8146E-10	0.00527
0.005	8	0.03	0.32	0.29	1.32E-07	9.91E-08	1.2E-07	3.378E-08	0	0	0	5.07E-08	4.223E-08	4.648E-08	1.8594E-10	0.0055
0.005	10	0.03	0.32	0.29	1.33E-07	9.821E-08	1.2E-07	3.378E-08	0	0	0	4.94E-07	4.447E-08	2.692E-07	1.0768E-09	0.03188
0.005	12	0.03	0.32	0.29	1.29E-07	9.507E-07	5.4E-07	1.576E-07	0	0	0	4.81E-08	4.85E-08	4.828E-08	1.931E-10	0.00123
0.005	14	0.03	0.32	0.29	1.35E-07	9.06E-08	1.1E-07	3.299E-08	0	0	0	5.25E-08	4.85E-08	5.052E-08	2.0206E-10	0.00612
0.005	16	0.03	0.32	0.29	1.07E-07	8.074E-08	9.4E-08	2.743E-08	0	0	0	5.34E-08	4.268E-08	4.805E-08	1.9221E-10	0.00701
0.005	18	0.03	0.32	0.29	1.08E-07	8.164E-08	9.5E-08	2.77E-08	0	0	0	5.39E-08	4.268E-08	4.828E-08	1.931E-10	0.00697
0.005	20	0.03	0.32	0.29	1.66E-07	9.104E-08	1.3E-07	3.748E-08	0	0	0	6.24E-08	4.313E-08	5.275E-08	2.1102E-10	0.00563
0.006	2	0.03	0.32	0.29	1.22E-07	8.612E-08	1E-07	3.044E-08	0	0	0	4.76E-08	4.089E-08	4.425E-08	1.7698E-10	0.00581
0.006	4	0.03	0.32	0.29	1.22E-07	8.477E-08	1E-07	3.025E-08	0	0	0	4.85E-08	3.999E-08	4.425E-08	1.7698E-10	0.00585
0.006	8	0.03	0.32	0.29	1.22E-07	8.836E-08	1.1E-07	3.07E-08	0	0	0	4.76E-08	4.223E-08	4.492E-08	1.7967E-10	0.00585
0.006	10	0.03	0.32	0.29	1.31E-07	9.194E-08	1.1E-07	3.253E-08	0	0	0	5.07E-08	4.268E-08	4.671E-08	1.8683E-10	0.00574
0.006	12	0.03	0.32	0.29	1.26E-07	8.657E-08	1.1E-07	3.097E-08	0	0	0	4.94E-08	4.447E-08	4.693E-08	1.8773E-10	0.00606
0.006	14	0.03	0.32	0.29	1.3E-07	8.657E-08	1.1E-07	3.155E-08	0	0	0	4.98E-08	4.133E-08	4.559E-08	1.8236E-10	0.00578
0.006	16	0.03	0.32	0.29	1.3E-07	8.388E-08	1.1E-07	3.123E-08	0	0	0	5.12E-08	3.506E-08	4.313E-08	1.725E-10	0.00552
0.006	18	0.03	0.32	0.29	1.3E-07	9.283E-08	1.1E-07	3.26E-08	0	0	0	4.76E-08	4.089E-08	4.425E-08	1.7698E-10	0.00543
0.006	20	0.03	0.32	0.29	1.26E-07	9.06E-08	1.1E-07	3.168E-08	0	0	0	4.98E-08	3.327E-08	4.156E-08	1.6623E-10	0.00525
0.007	2	0.03	0.32	0.29	1.18E-07	8.209E-08	1E-07	2.922E-08	0	0	0	4.49E-08	3.238E-08	3.865E-08	1.5459E-10	0.00529
0.007	4	0.03	0.32	0.29	1.21E-07	8.567E-08	1E-07	3.012E-08	0	0	0	4.54E-08	3.238E-08	3.887E-08	1.5549E-10	0.00516
0.007	8	0.03	0.32	0.29	1.21E-07	8.701E-08	1E-07	3.044E-08	0	0	0	4.36E-08	3.608E-08	3.983E-08	1.5932E-10	0.00523
0.007	10	0.03	0.32	0.29	1.26E-07	8.746E-08	1.1E-07	3.116E-08	0	0	0	4.49E-08	3.704E-08	4.098E-08	1.6392E-10	0.00526

Iodine (cm)	Water level (cm)	Integrated fluence of iodine between 28-32kVp							Integrated fluence of iodine between 33-40kVp							Ratio
		X1	X2	X2-X1	Y1	Y2	(Y2+Y1)/2	(Y2-Y1)/2*(X2-X1)	X1	X2	X2-X1	Y1	Y2	(Y2+Y1)/ 2	(Y2-Y1)/2*(X2-X1)	
0.007	12	0.03	0.32	0.29	1.19E-07	8.567E-08	1E-07	2.985E-08	0	0	0	4.67E-08	3.82E-08	4.245E-08	1.6982E-10	0.00569
0.007	14	0.03	0.32	0.29	1.25E-07	8.164E-08	1E-07	3.018E-08	0	0	0	5.03E-08	3.73E-08	4.38E-08	1.7519E-10	0.0058
0.007	16	0.03	0.32	0.29	1.21E-07	7.716E-08	9.9E-08	2.9E-08	0	0	0	5.07E-08	3.327E-08	4.201E-08	1.6803E-10	0.00579
0.007	18	0.03	0.32	0.29	1.3E-07	8.343E-08	1.1E-07	3.116E-08	0	0	0	4.89E-08	3.686E-08	4.29E-08	1.7161E-10	0.00551
0.007	20	0.03	0.32	0.29	1.21E-07	8.836E-08	1E-07	3.051E-08	0	0	0	4.13E-08	3.103E-08	3.618E-08	1.4474E-10	0.00474
0.008	2	0.03	0.32	0.29	1.27E-07	7.895E-08	1E-07	3.012E-08	0	0	0	3.55E-08	2.924E-08	3.238E-08	1.2951E-10	0.0043
0.008	4	0.03	0.32	0.29	1.27E-07	8.343E-08	1.1E-07	3.077E-08	0	0	0	3.46E-08	3.059E-08	3.26E-08	1.3041E-10	0.00424
0.008	8	0.03	0.32	0.29	1.23E-07	7.403E-08	9.9E-08	2.881E-08	0	0	0	3.1E-08	3.238E-08	3.171E-08	1.2683E-10	0.0044
0.008	10	0.03	0.32	0.29	1.26E-07	7.582E-07	4.4E-07	1.292E-07	0	0	0	3.14E-08	3.238E-08	3.19E-08	1.276E-10	0.00099
0.008	12	0.03	0.32	0.29	1.29E-07	7.358E-08	1E-07	2.959E-08	0	0	0	3.15E-07	3.372E-08	1.743E-07	6.9709E-10	0.02356
0.008	14	0.03	0.32	0.29	1.26E-07	7.268E-08	9.9E-08	2.9E-08	0	0	0	2.97E-08	3.417E-08	3.193E-08	1.2772E-10	0.0044
0.008	16	0.03	0.32	0.29	1.15E-07	7.044E-08	9.3E-08	2.704E-08	0	0	0	2.88E-08	2.745E-08	2.812E-08	1.1249E-10	0.00416
0.008	18	0.03	0.32	0.29	1.2E-07	6.686E-08	9.3E-08	2.724E-08	0	0	0	3.15E-08	3.059E-08	3.103E-08	1.2414E-10	0.00456
0.008	20	0.03	0.32	0.29	1.15E-07	7.492E-08	9.5E-08	2.776E-08	0	0	0	3.42E-08	2.835E-08	3.126E-08	1.2503E-10	0.0045
0.009	2	0.03	0.32	0.29	1.18E-07	8.164E-08	1E-07	2.916E-08	0	0	0	3.55E-08	2.611E-08	3.081E-08	1.2324E-10	0.00423
0.009	4	0.03	0.32	0.29	1.2E-07	8.253E-08	1E-07	2.953E-08	0	0	0	3.42E-08	2.611E-08	3.014E-08	1.2056E-10	0.00408
0.009	8	0.03	0.32	0.29	1.26E-07	8.074E-08	1E-07	3.012E-08	0	0	0	3.55E-08	2.656E-08	3.103E-08	1.2414E-10	0.00412
0.009	10	0.03	0.32	0.29	1.2E-07	7.627E-08	9.8E-08	2.868E-08	0	0	0	3.73E-08	2.7E-08	3.215E-08	1.2862E-10	0.00449
0.009	12	0.03	0.32	0.29	1.23E-07	8.119E-08	1E-07	2.979E-08	0	0	0	3.69E-08	2.7E-08	3.193E-08	1.2772E-10	0.00429
0.009	14	0.03	0.32	0.29	1.13E-07	7.358E-08	9.4E-08	2.73E-08	0	0	0	3.95E-08	2.835E-08	3.395E-08	1.3578E-10	0.00497
0.009	16	0.03	0.32	0.29	1.08E-07	7.268E-08	9E-08	2.639E-08	0	0	0	4E-08	2.253E-08	3.126E-08	1.2503E-10	0.00474
0.009	18	0.03	0.32	0.29	1.24E-07	7.134E-08	9.8E-08	2.848E-08	0	0	0	4E-08	2.611E-08	3.305E-08	1.322E-10	0.00464
0.009	20	0.03	0.32	0.29	1.18E-07	7.716E-08	9.8E-08	2.851E-08	0	0	0	4.04E-08	2.208E-08	3.126E-08	1.2503E-10	0.00439
0.01	2	0.03	0.32	0.29	1.22E-07	7.537E-08	9.9E-08	2.887E-08	0	0	0	3.55E-08	2.566E-08	3.059E-08	1.2235E-10	0.00424
0.01	4	0.03	0.32	0.29	1.26E-07	7.895E-07	4.6E-07	1.337E-07	0	0	0	3.64E-08	2.476E-08	3.059E-08	1.2235E-10	0.00092
0.01	8	0.03	0.32	0.29	1.21E-07	7.492E-08	9.8E-08	2.861E-08	0	0	0	3.51E-08	2.432E-08	2.969E-08	1.1876E-10	0.00415
0.01	10	0.03	0.32	0.29	1.21E-07	7.716E-08	9.9E-08	2.894E-08	0	0	0	3.46E-08	2.432E-08	2.947E-08	1.1787E-10	0.00407
0.01	12	0.03	0.32	0.29	1.22E-07	7.492E-08	9.8E-08	2.874E-08	0	0	0	3.42E-08	2.387E-08	2.902E-08	1.1608E-10	0.00404
0.01	14	0.03	0.32	0.29	1.18E-07	7.223E-08	9.5E-08	2.776E-08	0	0	0	3.46E-08	2.387E-08	2.924E-08	1.1697E-10	0.00421
0.01	16	0.03	0.32	0.29	1.07E-07	7.582E-08	9.1E-08	2.672E-08	0	0	0	3.42E-08	2.163E-08	2.79E-08	1.116E-10	0.00418
0.01	18	0.03	0.32	0.29	1.15E-07	7.537E-08	9.5E-08	2.776E-08	0	0	0	3.6E-08	2.163E-08	2.88E-08	1.1518E-10	0.00415
0.01	20	0.03	0.32	0.29	1.08E-07	7.582E-08	9.2E-08	2.678E-08	0	0	0	3.91E-08	1.984E-08	2.947E-08	1.1787E-10	0.0044
0.015	2	0.03	0.32	0.29	9.86E-08	6.747E-08	8.3E-08	2.424E-08	0	0	0	2.47E-08	1.261E-08	1.865E-08	7.4608E-11	0.00308
0.015	4	0.03	0.32	0.29	1.01E-07	7.134E-08	8.6E-08	2.515E-08	0	0	0	2.39E-08	1.223E-08	1.805E-08	7.219E-11	0.00287
0.015	8	0.03	0.32	0.29	1.03E-07	6.731E-08	8.5E-08	2.482E-08	0	0	0	2.16E-08	1.223E-08	1.693E-08	6.7712E-11	0.00273

Iodine (cm)	Water level (cm)	Integrated fluence of iodine between 28-32kVp							Integrated fluence of iodine between 33-40kVp							Ratio
		X1	X2	X2-X1	Y1	Y2	(Y2+Y1)/2	(Y2-Y1)/2*(X2-X1)	X1	X2	X2-X1	Y1	Y2	(Y2+Y1)/ 2	(Y2-Y1)/2*(X2-X1)	
0.015	10	0.03	0.32	0.29	1.08E-07	7.134E-08	8.9E-08	2.613E-08	0	0	0	2.21E-08	1.267E-08	1.738E-08	6.9503E-11	0.00266
0.015	12	0.03	0.32	0.29	1.06E-07	6.552E-08	8.6E-08	2.502E-08	0	0	0	2.43E-08	1.223E-08	1.827E-08	7.3086E-11	0.00292
0.015	14	0.03	0.32	0.29	1.1E-07	6.686E-08	8.8E-08	2.58E-08	0	0	0	2.7E-08	1.133E-08	1.917E-08	7.6668E-11	0.00297
0.015	16	0.03	0.32	0.29	1.07E-07	7.313E-08	9E-08	2.626E-08	0	0	0	2.61E-08	1.088E-08	1.85E-08	7.3981E-11	0.00282
0.015	18	0.03	0.32	0.29	1.05E-07	7.089E-08	8.8E-08	2.567E-08	0	0	0	2.61E-08	1.088E-08	1.85E-08	7.3981E-11	0.00288
0.015	20	0.03	0.32	0.29	1.02E-07	6.865E-08	8.5E-08	2.495E-08	0	0	0	2.57E-08	1.088E-08	1.827E-08	7.3085E-11	0.00293
0.02	2	0.03	0.32	0.29	7.85E-08	5.343E-08	6.6E-08	1.926E-08	0	0	0	1.98E-08	5.428E-09	1.259E-08	5.0372E-11	0.00261
0.02	4	0.03	0.32	0.29	7.96E-08	5.594E-08	6.8E-08	1.979E-08	0	0	0	1.96E-08	5.786E-09	1.268E-08	5.073E-11	0.00256
0.02	8	0.03	0.32	0.29	8.29E-08	5.87E-08	7.1E-08	2.067E-08	0	0	0	1.9E-08	5.905E-09	1.245E-08	4.9816E-11	0.00241
0.02	10	0.03	0.32	0.29	8.35E-08	5.991E-08	7.2E-08	2.094E-08	0	0	0	2.12E-08	6.106E-09	1.366E-08	5.4653E-11	0.00261
0.02	12	0.03	0.32	0.29	8.35E-08	5.85E-08	7.1E-08	2.073E-08	0	0	0	2.16E-08	6.711E-09	1.417E-08	5.6668E-11	0.00273
0.02	14	0.03	0.32	0.29	7.87E-08	6.006E-08	6.9E-08	2.026E-08	0	0	0	2.26E-08	5.786E-09	1.421E-08	5.682E-11	0.0028
0.02	16	0.03	0.32	0.29	7.74E-08	5.935E-08	6.8E-08	1.997E-08	0	0	0	2.15E-08	5.965E-09	1.376E-08	5.5029E-11	0.00276
0.02	18	0.03	0.32	0.29	8.27E-08	6.435E-08	7.4E-08	2.147E-08	0	0	0	2.34E-08	5.905E-09	1.467E-08	5.8683E-11	0.00273
0.02	20	0.03	0.32	0.29	8.17E-08	6.354E-08	7.3E-08	2.12E-08	0	0	0	2.14E-08	4.897E-09	1.316E-08	5.2638E-11	0.00248
0.025	2	0.03	0.32	0.29	5.83E-08	4.733E-08	5.3E-08	1.543E-08	0	0	0	1.84E-08	3.265E-09	1.086E-08	4.3421E-11	0.00281
0.025	4	0.03	0.32	0.29	5.94E-08	5.029E-08	5.5E-08	1.602E-08	0	0	0	1.72E-08	3.265E-09	1.025E-08	4.1003E-11	0.00256
0.025	8	0.03	0.32	0.29	6.23E-08	5.114E-08	5.7E-08	1.656E-08	0	0	0	1.78E-08	3.339E-09	1.055E-08	4.2194E-11	0.00255
0.025	10	0.03	0.32	0.29	6.32E-08	5.271E-08	5.8E-08	1.693E-08	0	0	0	1.79E-08	3.495E-09	1.071E-08	4.2821E-11	0.00253
0.025	12	0.03	0.32	0.29	6.18E-08	4.926E-08	5.6E-08	1.622E-08	0	0	0	1.76E-08	3.495E-09	1.055E-08	4.2194E-11	0.0026
0.025	14	0.03	0.32	0.29	6.09E-08	5.24E-08	5.7E-08	1.654E-08	0	0	0	1.84E-08	3.182E-09	1.078E-08	4.3135E-11	0.00261
0.025	16	0.03	0.32	0.29	5.92E-08	5.365E-08	5.6E-08	1.647E-08	0	0	0	1.74E-08	2.996E-09	1.018E-08	4.073E-11	0.00247
0.025	18	0.03	0.32	0.29	6.35E-08	5.757E-08	6.1E-08	1.768E-08	0	0	0	1.95E-08	2.868E-09	1.118E-08	4.4702E-11	0.00253
0.025	20	0.03	0.32	0.29	5.7E-08	5.123E-08	5.4E-08	1.58E-08	0	0	0	1.72E-08	2.862E-09	1.005E-08	4.0197E-11	0.00254

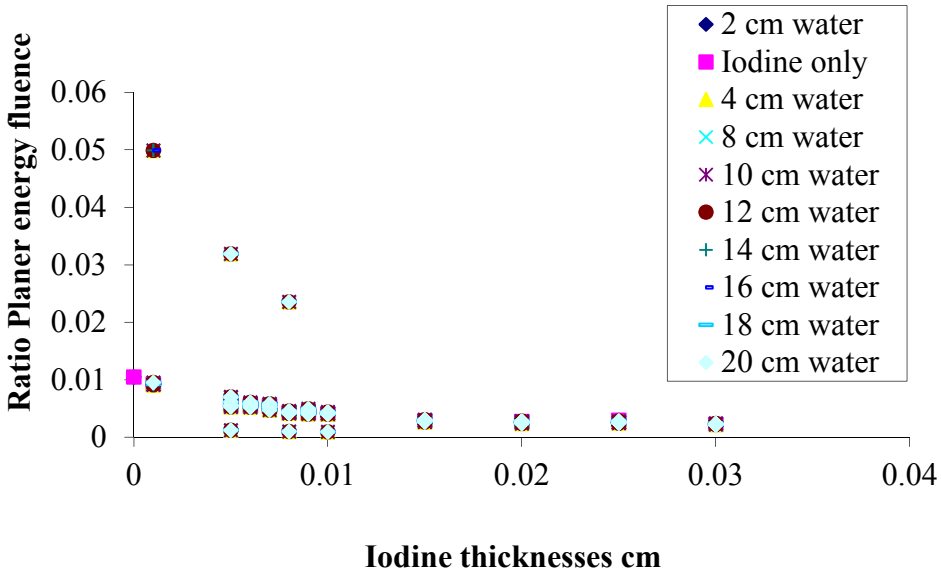

Figure 4.25 The ratio of planer energy fluence at 50 kVp of iodine and water placed on the top of the detector run made with 100,000 histories; the spectrum shows the effect of water when added to the simulation.

4.3.4 Detector response to the iodine peaks

The simulation was tested to check the response of three model detectors. One model was simulated with x-ray using a 0.001 cm iodine slab placed between the x-ray tube and the detector. The spectrum was made at 50 kVp. The other two detectors were made without iodine media but with the same simulation and parameters. The integral fluence was obtained at the iodine peaks, between the energy ranges of 28-32 kVp and 33-40 kVp (Table 4.4). The spectra were plotted and it was obvious that the spectrum with iodine showed high absorption compared to the response of the other two detectors which had no absorption. Consequently, using Monte Carlo simulation will help to distinguish between the absorption of the spectrum with and without the contrast media such as iodine,

and it will make the subtraction between both spectra easier. It also helps to improve the contrast of the images.

Table 4.4 The integral fluence at 50 kVp the spectrum taken with and without iodine to check the detector responses.

Detector	Water (cm)	X1	X2	X2-X1	Y1	Y2	(Y2+Y1)/2	(Y2-Y1) /2* (X2-X1)	X1	X2	X2-X1	Y1	Y2	(Y2+Y1)/2	(Y2-Y1) /2* (X2-X1)	Ratio
1	2	0.028	0.32	0.292	8E-11	2.4E-10	1.601E-10	4.6749E-11	0.033	0.037	0.004	4.9E-09	1.5E-08	9.905E-09	3.9622E-11	0.848
2	2	0.028	0.32	0.292	5E-11	4.8E-09	2.422E-09	7.0712E-10	0.033	0.037	0.004	1.3E-09	1.3E-10	7.087E-10	2.8347E-12	0.004
3	2	0.028	0.32	0.292	8E-11	2.4E-10	1.601E-10	4.6749E-11	0.033	0.037	0.004	4.9E-09	1.5E-08	9.905E-09	3.9622E-11	0.848

4.3.5 Selecting the x-ray tube voltage

The simulation was run, using four different setups, to identify an x-ray tube voltage that allows high contrast images to be formed. In the first setup, the detector was placed in front of the x-ray source and the energy varied from 50 kVp to 100 kVp using a 0.001 cm aluminium filter. In the second setup, the blood vessel was placed between the x-ray source and the detector. In the third setup, a 0.001 cm slab of iodine was placed in between the x-ray source and the detector. In the fourth setup, the phantom was filled with 0.001 mm of iodine. The simulated x-ray spectra for each x-ray tube voltage were obtained and are shown in figures 4.26, 4.27, 4.28, 4.29, 4.30 and 4.31.

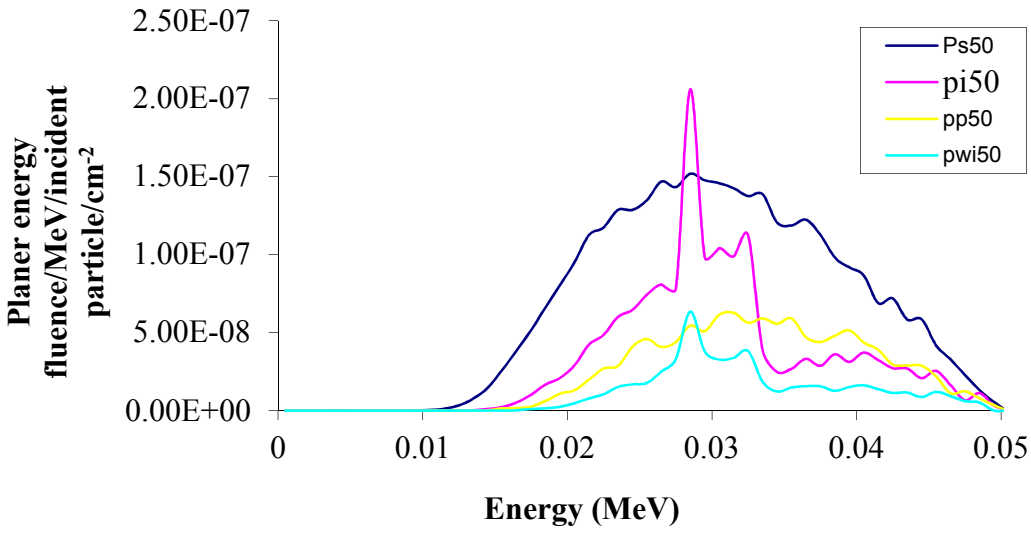

Figure 4.26 The planer energy fluence of detector with 50 kVp on the x-ray tube, the four spectra are; direct spectra (PS), spectra of iodine slab (PI), spectra of phantom (PP) and spectra of phantom with iodine (PWI).

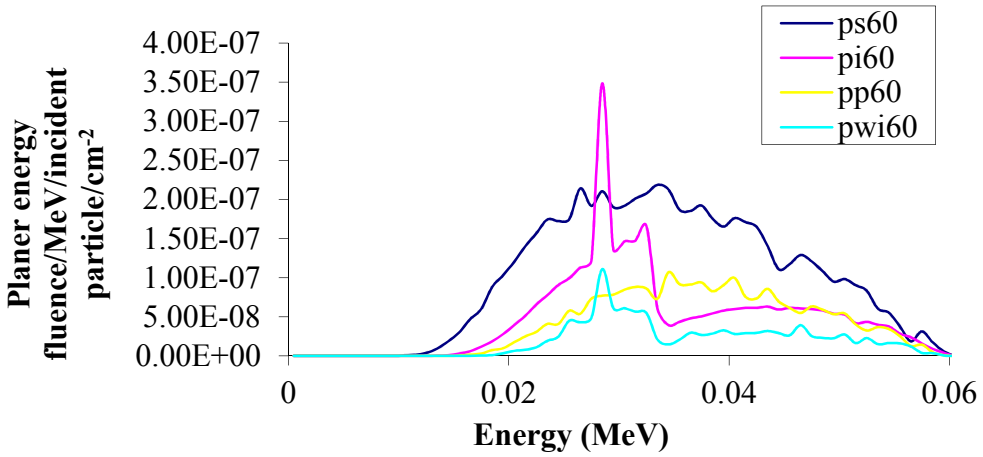

Figure 4.27 The planer energy of detector with 60 kVp on the x-ray tube, the four spectra are; direct spectra (PS), spectra of iodine slab (PI), spectra of phantom (PP) and spectra of phantom with iodine (PWI).

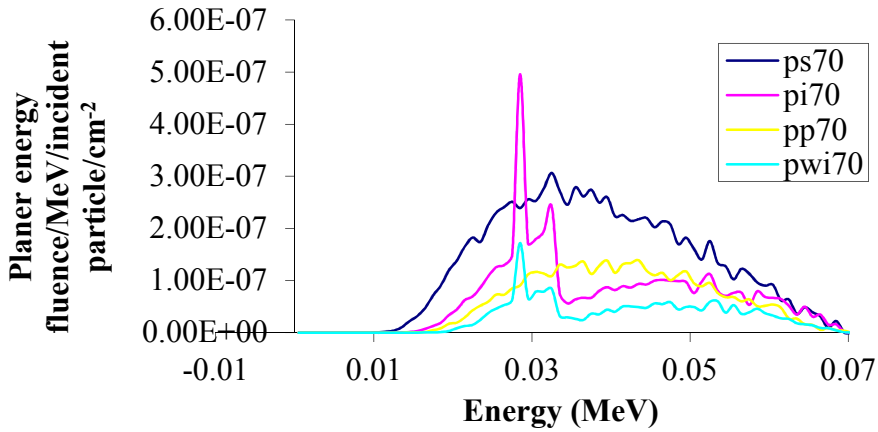

Figure 4.28 The planer energy of detector with 70 kVp on the x-ray tube, the four spectra are; direct spectra (PS), spectra of iodine slab (PI), spectra of phantom (PP) and spectra of phantom with iodine (PWI).

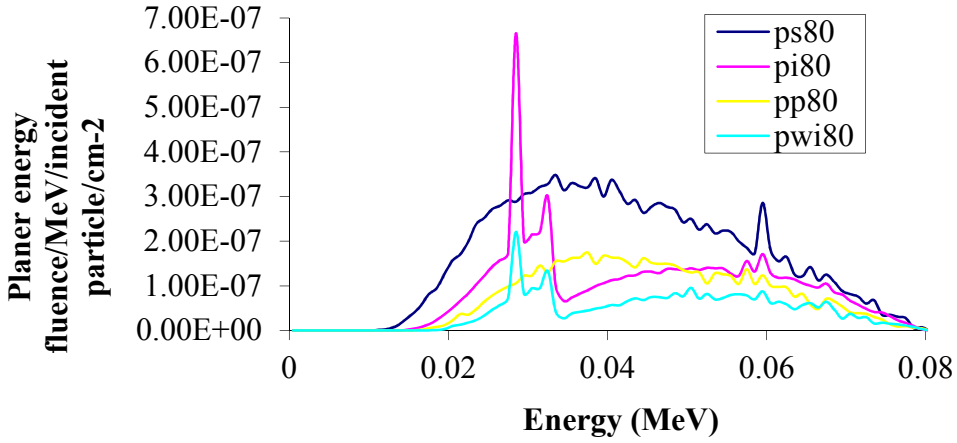

Figure 4.29 The planer energy of detector with 80 kVp on the x-ray tube, the four spectra are; direct spectra (PS), spectra of iodine slab (PI), spectra of phantom (PP) and spectra of phantom with iodine (PWI).

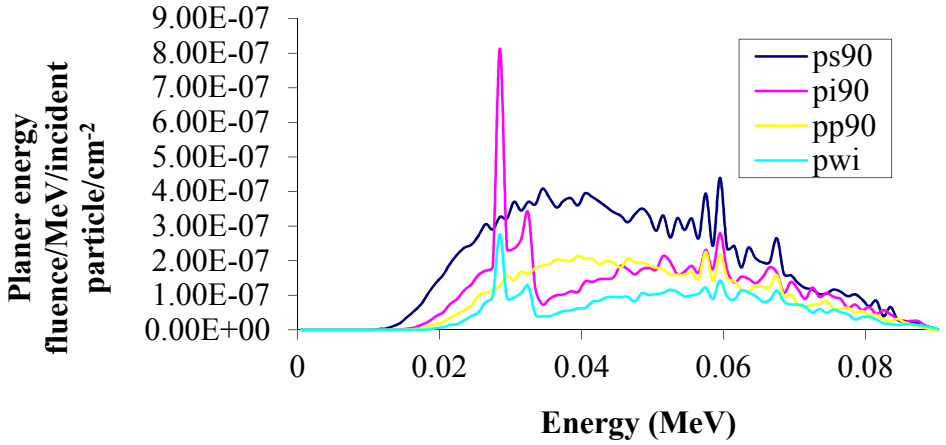

Figure 4.30 The planer energy of detector with 90 kVp on the x-ray tube, the four spectra are; direct spectra (PS), spectra of iodine slab (PI), spectra of phantom (PP) and spectra of phantom with iodine (PWI).

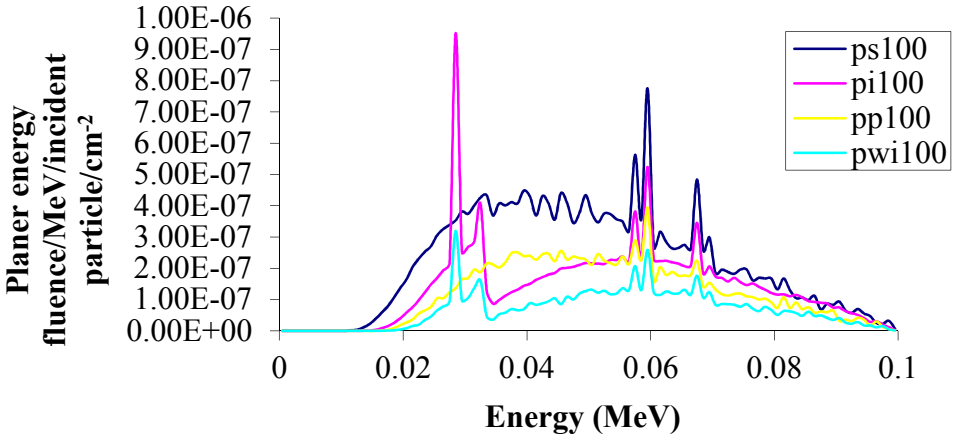

Figure 4.31 The planer energy of detector with 100 kVp on the x-ray tube, the four spectra are; direct spectra (PS), spectra of iodine slab (PI), spectra of phantom (PP) and spectra of phantom with iodine (PWI).

The integral fluence curve between the plane iodine (pi) and the plane phantom (pp) was calculated to find the maximum absorption, which was at the peaks having energies of 33.5 and 50 kVp. The relative difference of iodine to phantom was calculated as in Table 4.5 and the spectra plotted as shown in Figure 4.32. Absorption was at energy range between 33.5-50 kVp. The area was calculated under the total spectra Table 4.6 Moreover, Figure 4.33; it is obvious that the maximum absorption is at 50 kVp.

Table 4.5 The integral ratio under the spectra peaks at different energies shows the relative difference of iodine to phantom.

Energy (kVp)	Direct spectra of phantom	spectra of iodine slab	Direct x-ray spectra	Constant ratio	Energy range (kVp)	
	PP	PI	PS	(PI-PP)/PS	From	To
50	5.61E-10	4.07224E-10	1.19368E-09	-0.128827835	33.5	50
60	1.36404E-09	9.96452E-10	2.70459E-09	-0.135910888	33.5	50
70	2.16326E-09	1.52296E-09	4.01184E-09	-0.159603648	33.5	50
80	2.75929E-09	2.05175E-09	5.30847E-09	-0.133283915	33.5	50
90	3.51054E-09	2.52693E-09	6.39224E-09	-0.153875167	33.5	50
100	4.17931E-09	2.96914E-09	7.21076E-09	-0.167828218	33.5	50

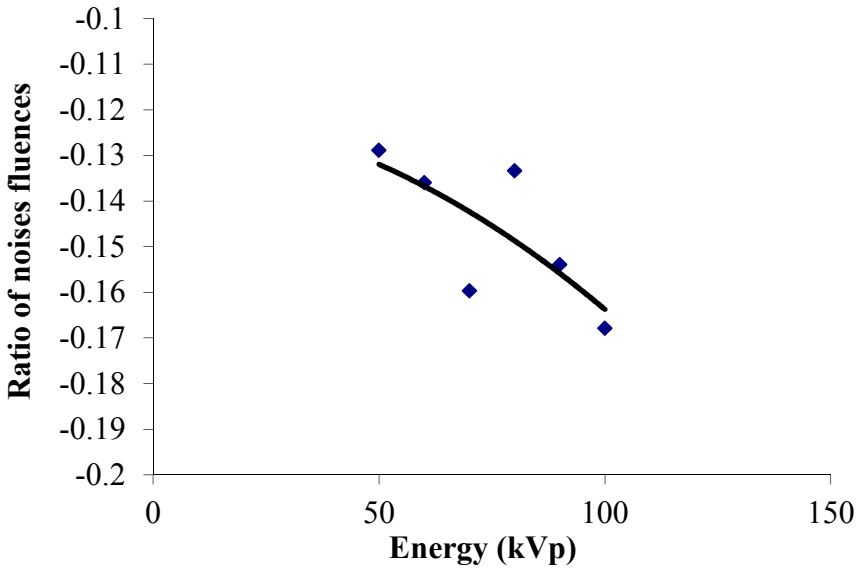

Figure 4.32 The plot show that the highest fluence at 50 kVp.

Table 4.6 The integral ratio under the spectra at different energies covers the total fluence under the spectra.

Energy (kVp)	Direct spectra of phantom	spectra of iodine slab	Direct x-ray spectra	Ratio of noises fluences
	PP	PI	PS	(PI-PP)/PS
50	1.58011E-09	1.15814E-09	3.28614E-09	0.128409565
60	2.92084E-09	2.35773E-09	5.87682E-09	0.095819465
70	4.72825E-09	4.02143E-09	8.89976E-09	0.079420065
80	7.27882E-09	5.95059E-09	1.29389E-08	0.102653798
90	9.93399E-09	8.55406E-09	1.69322E-08	0.081497377
100	1.37636E-08	1.17109E-08	2.15744E-08	0.095147733

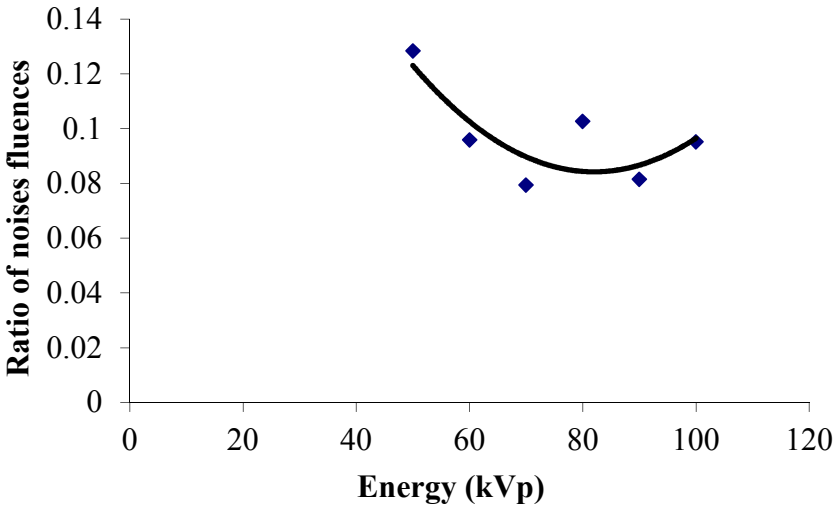

Figure 4.33 The plot of the noise shows that the highest fluence at 50 kVp, it considered as the optimum energy.

4.3.6 Finding the minimum iodine concentration for forming images

To run the simulation, the x-ray tube voltage was set to 50 kVp (found in section 4.3.3, p.94); and the concentration of the iodine slab were varied to find the minimum detectable iodine concentration. The simulation results are shown in Table 4.7 and Figure 4.34, (p.109) and allow the minimum detectable concentration of iodine of approximately 6 to 8 mg to be calculated as follows. Assuming we have 80 g of iodine in 800 cm3 of blood which equal to 0.01 g/cm3, the blood vessel is assumed to be 10 cm wide, 10 cm height and 0.1 cm in thickness, so the density will be 0.01 g/cm3 of iodine contents in 10 cm3. If we have 0.00025 g/cm3 of iodine contrast media the volume will be 0.025 cm3 by knowing the assumed volume of the blood vessel, the thickness can be calculated which equal to 0.0025 cm, for 2 mg of iodine contrast media corresponding to a 0.0025 cm slab thickness. Figure 4.34 shows that the finest iodine concentration is between 6 and 8 mg/l of iodine.

Table 4.7 The iodine concentrations at 50 kVp.

Iodine concentration (g/ml)	spectra of iodine slab	Direct spectra of phantom	Direct x-ray spectra	Ratio of noises fluences
	PI	PP	PS	(PI-PP)/PS
2	2.1282E-08	1.33207E-08	2.6897E-08	0.29599391
4	1.6599E-08	1.33207E-08	2.6897E-08	0.121877973
6	1.205E-08	1.33207E-08	2.6897E-08	-0.047253015
7	1.1418E-08	1.33207E-08	2.6897E-08	-0.070750451
7.5	1.0819E-08	1.33207E-08	2.6897E-08	-0.093017984
8	8.1661E-09	1.33207E-08	2.6897E-08	-0.191639339
10	7.055E-09	1.33207E-08	2.6897E-08	-0.232949073
12	4.8109E-09	1.33207E-08	2.6897E-08	-0.316384756
14	4.1383E-09	1.33207E-08	2.6897E-08	-0.341389571
16	1.816E-09	1.33207E-08	2.6897E-08	-0.427732039
18	2.065E-09	1.33207E-08	2.6897E-08	-0.418472355
20	1.069E-11	1.33207E-08	2.6897E-08	-0.494849587

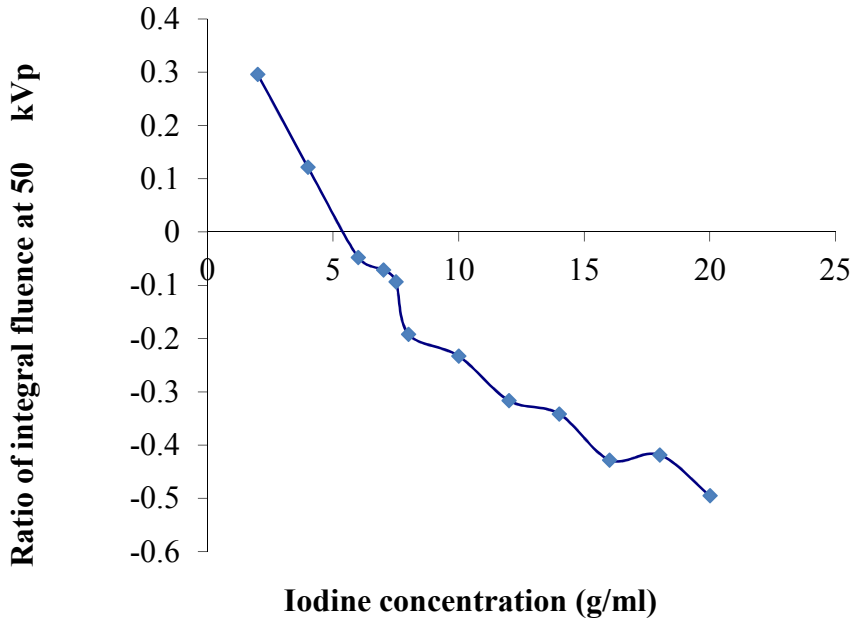

Figure 4.34 The iodine concentration at 50 kVp.

4.4 Discussion and Summary

I used code BEAMnrc code to simulate and measure the x-ray spectrum for several different angiography imaging models. Each model was simulated using a range of parameters to identify the optimal parameter values for spectral imaging. The transmitted spectrum of iron can only be detected when large amounts of iron, which are in excess of that found in the human body, are present. Adding a layer of water on top of the iron layer led to the complete attenuation of the iron fluorescence x-rays, which made it impossible to detect the iron.

This result is expected, as the absorption spectrum of iron in this energy range is very similar to that of water. Thus I have shown that a "plain film" or spectral x-ray projection image cannot be used to find iron deposits. However, I note that other members of the MARS-CT research group have used the MARS-CT system with a silicon Medipix 3.0 quad camera to detect deposits of calcium and iron in reconstructed CT images of excised atheroma's (Zainon *et al.*, 2010).

The calcium in bones is readily detectable due to its large concentration, and similar calcium concentrations occur in atheroma. Small dense deposits of iron are known to be present in atheroma's, and small dense deposits have been observed in spectral CT studies by (Zainon *et al.*, 2010). They were not able to differentiate between iron and calcium on the basis of their spectral CT data, but stained samples indicate that the small punctate deposits are iron.

Having succeeded with using BEAMnrc to get these results, I then looked at other more interesting physical situations. The iodine spectra at different energies, I found that optimum energy is 50 kVp, where iodine can be detected at a concentration between 6 and 8mg/l of iodine.

My work could be extended to simulating the acquisition of CT images (Bell, 2011). To do this the simulation needs to be more detailed to account for the rotational geometry of a CT scan and the anatomy of the human body. The iodine used in this simulation was considered to be metal, but in real situations the iodine is diluted with other chemicals. To improve the simulation, materials should be represented in the simulation by the actual chemical compound and concentration used.

In this work a slab of air represented the detector. Future work requires the use of geometry and sensor materials that represent the Medipix detector in the configuration it is used in the experimental setup. This will allow the response of the detector to be accounted for in the simulated image data.

Chapter 5

5 Development of a program for Dual Energy X-ray Subtraction

5.1 Introduction

This chapter describes a Matlab program developed to perform dual energy x-ray subtraction. Aim of the work presented in this chapter is to improve the contrast of angiography by utilising changes in x-ray attenuation that occur at the k-edge energy of the contrast medium. This can be achieved by using two different techniques. The first technique to improve visual contrast is digital subtraction angiography (DSA). In DSA, a "mask" image is acquired before the infusion of the iodine contrast agent. This is subsequently subtracted from images with iodine contrast. In this way, the appearance of blood vessels is amplified. The second technique is dual energy angiography (DEA) which improves image contrast and differentiates better between the absorbing elements compositions. The subject is imaged twice with two different energy spectra from the x-ray source. Different energy spectra may be obtained by applying different x-ray tube voltages. A category within this technology is k-edge subtraction imaging. Two energy spectra are chosen so one spectrum peaks below the k-edge of the iodine contrast medium and the other just above the k-edge. In particular, it uses subtraction imaging at the iodine k-edge, which is suitable for angiography imaging application.

Both techniques described above require software to perform the image subtraction. To do this, an application with a graphical user interface (GUI) was developed using Matlab to perform common image manipulation tasks such as, loading image files of different types (e.g. jpg, txt, dicom and tif). This application

allows the user to load and manipulate the two images that need to be subtracted. Once loaded, the images can be transformed and registered to pixel points selected by the user, and then subtracted.

After testing to check that the application could load and manipulate different types and sizes of images, the program was evaluated using x-ray images of a blood vessel phantom (described later in this chapter) acquired using conventional medical x-ray equipment at Christchurch Hospital using different choices of parameters such as; iodine concentration (5-8 g/ml), and x-ray energy (50 keV).

The analysis of the images presented in this chapter demonstrates that the application can correctly load and manipulate the images and perform the image subtraction operation for images with and without iodine. The subtracted image clearly shows the regions of the image that contain iodine contrast media. The application developed in this chapter will be used in the next stage of the project (experimental studies presented in chapter 8) to subtract the images at the iodine k-edge energies.

5.2 Program Structure

5.2.1 Overview

The program was designed as a single window GUI application with controls for loading and manipulating image files in different formats (for example txt, tif and dicom). Once the image files are selected, they are loaded and the image registration and subtraction operations are performed. The application allows images of different sizes to be subtracted. To do this the two images must be transformed so that the image size and resolution are matched. This was done by

selecting pixels in each image, which correspond to the same position, and using these pixels as a basis for performing a transformation on each image. The transformation is applied to resize the original image, while retaining the original image resolution as it was, regardless of the image size.

To perform the image subtraction, the two images to be subtracted are loaded, the first image is obtained without iodine, and the second image obtained with iodine. Then, the images are registered by selecting a point (corresponding to a feature) in the first image and the equivalent point on the second image then, transforming the images by applying function from the image processing toolbox. After applying the transformation the images are subtracted and the resulting output image is displayed (and can be saved).

5.2.2 Image registration and adjustment

When the two images, which will be subtracted, are loaded, they need to be adjusted to match the pixel size. The Matlab Image Processing Toolbox provides tools to support point mapping in images to determine the parameters of the transformation required to bring an image into alignment with another image. In point mapping, you pick points in a pair of images that identify the same feature (such as an anatomical landmark) in both the images. Then, a spatial mapping is inferred from the positions of these control points. The code ‘cpselect’ created as a script that launches the Control Point Selection Tool with an input and a base image. The script then uses the control points selected to create a ‘tform’ structure and passes the ‘tform’ and the input image to the imtransform function; the function result is the registered image.

At least three points can be selected. The program will then do the transformation and register the two images by using a linear conformal transformation. This code is used to interpolate between two adjacent pixels to match the image size of the two loaded images but it slows the program because it takes long a time to process the data. After the image is transformed and registered, the program shows the registered image.

5.2.3 Image subtraction

The registered images are now transformed, registered and ready to be subtracted. Actually to do the subtraction, the image can be selected depending on the type of image. In some cases the user needs to subtract the image having contrast medium from the image without contrast medium. In other cases, the subtraction is made of images with high energy from those with low energy, using the k-edge energy of the contrast medium. The following sections will explain how the program was used to subtract the x-ray images that were obtained at Christchurch hospital.

5.2.4 User interface

The Matlab program is software that can be used to manage the image with the graphical user interface, as shown in Figure 5.1 and see the Matlab code in APPENDIX A. In this work the program has been designed with the ability to load files with different extensions. The files are registered and then the subtraction will be produced.

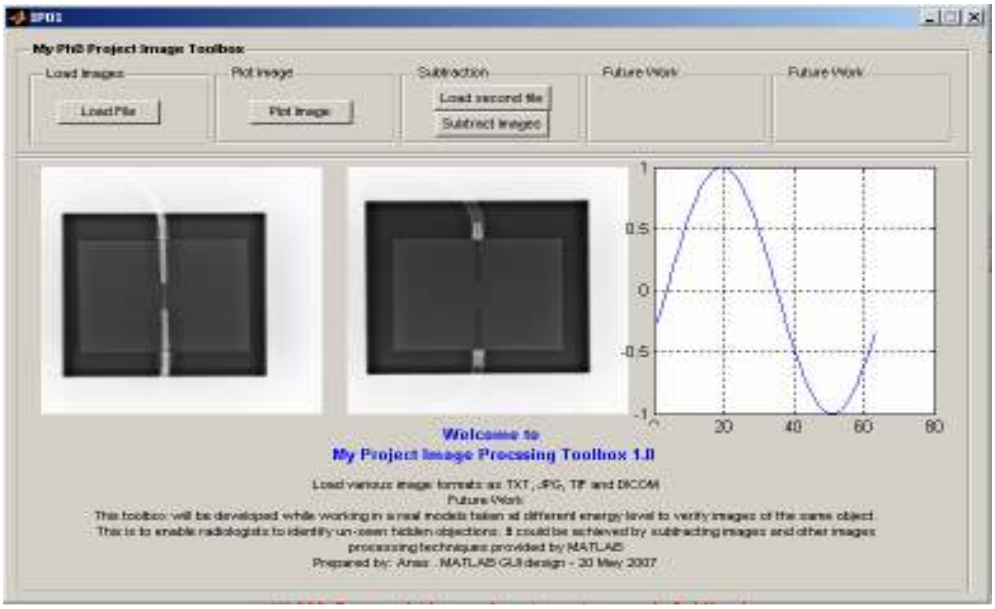

Figure 5.1 The Matlab graphical user interface used in the project.

5.3 Using the image subtraction program

In this work, the base image is the image of blood vessel phantom with iodine contrast media at 90 kVp (Figure 5.3a). The image to be registered is the image without iodine contrast media at 90 kVp (Figure 5.3b). The toolbox provides an interactive tool, called the Control Point Selection Tool, which you can use to pick pairs of corresponding control points in both images. To start this tool enter 'cpselect' at the Matlab prompt, specifying as arguments the input and base images. The Control Point Selection Tool displays two views of both the input image and the base image in which you can pick control points by pointing and clicking. The figure shows the Control Point Selection Tool with three pairs of control points selected. The number of control point pairs picked is regarding to the type of transformation we used which is the linear conformal transformation. The Control Point Pairs was saved to the Matlab workspace.

5.3.1 Phantom design

The project used a blood vessel phantom, built by the Physics and Astronomy workshop staff, comprising a 10 cm square piece of Plexiglas (Acrylic) that contained holes drilled through the centre with diameters ranging from 1 to 4 mm to allow the injection of the contrast media. The outer opening on one side was connected to a tube, the end of which was blocked. On the other side a tube connected the opening to a syringe pump (Figure 5.2).

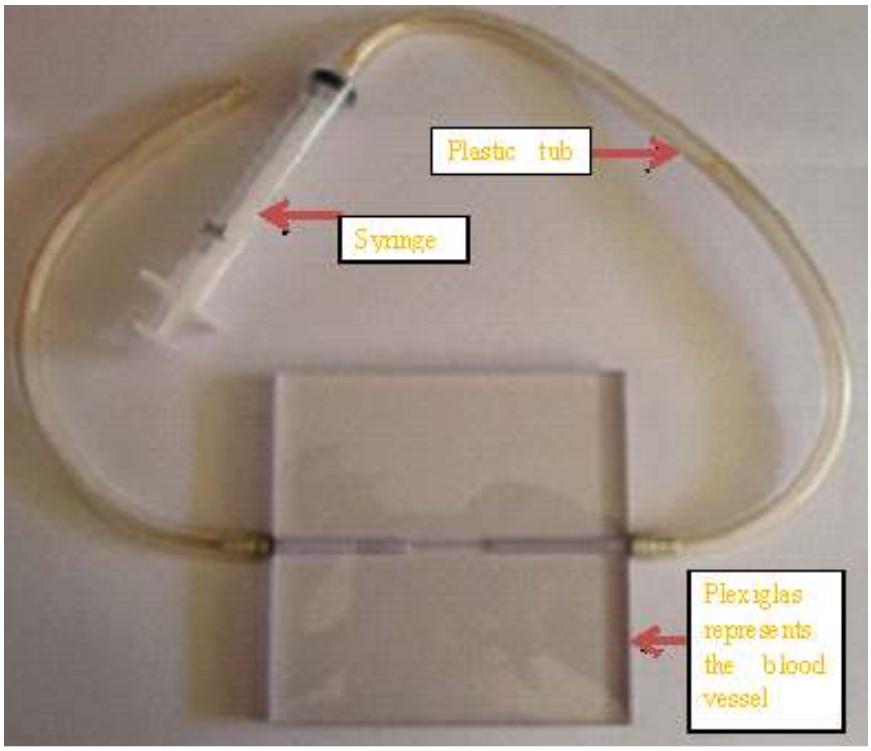

Figure 5.2 Phantom represents blood vessel made of Plexiglas.

5.3.2 Program Test

The control points passed to the cp2tform function that determines the parameters of the linear conformal transformation needed to bring the image into alignment. 'cp2tform' is a data-fitting function that determines the transformation based on the geometric relationship of the control points. As the final step in image registration, transform the input image to bring it into alignment with the base

image (Figure 5.3c). Then the transformed image was subtracted from the base one to perform the subtracted image witch actually showed the blood vessel (Figure 5.3d).

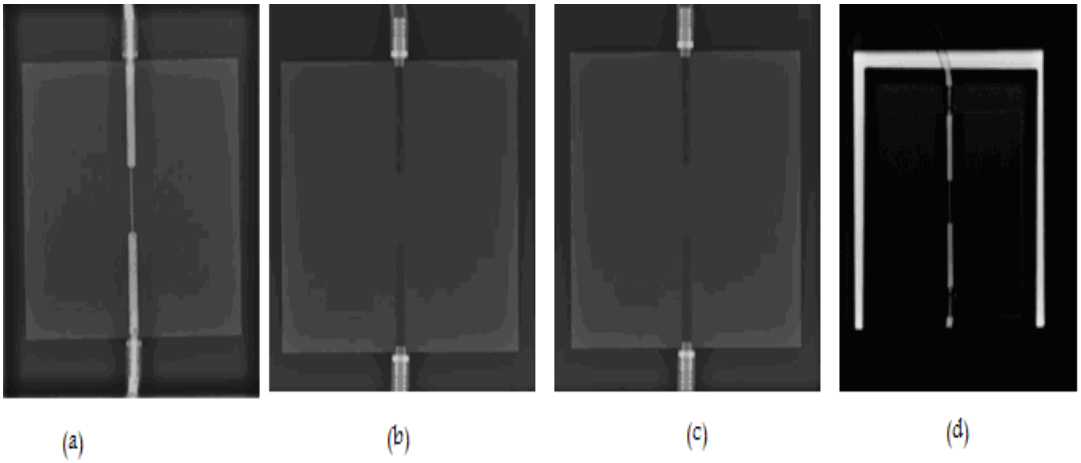

Figure 5.3 (a) digital image with iodine at 90 kVp, (b) digital image without iodine at 90 kVp, (c) the image without iodine after applying the registration transformation and (d) the subtracted image were the iodine can be seen clearly.

5.3.3 X-ray subtraction imaging using the application

5.3.3.1 Images taken with the blood vessel phantom

The phantom was exposed to x-rays from an x-ray machine at Christchurch Hospital. Images of the phantom were taken at different energies and were repeated using different concentration of iodine (Table 5.1).

The phantom was exposed to x-rays at different x-ray energies of 50, 60, 70, 80, 90 and 100 kVp. The result showed that at low energy, the contrast was much better than the contrast at high energy (Figure 5.4).

Table 5.1 Parameters used for imaging the phantom

Image type	Energy (kVp)	mA
Plane Phantom	50	60
Plane Phantom	60	60
Plane Phantom	70	60
Plane Phantom	80	60
Plane Phantom	90	60
Plane Phantom	100	60
phantom with water	50	60
phantom with water	60	60
phantom with water	70	60
phantom with water	80	60
phantom with water	90	60
phantom with water	100	60
Iodine with2ml	50	60
Iodine with2ml	70	60
Iodine with2ml	90	60
Iodine with4ml	50	60
Iodine with4ml	70	60
Iodine with4ml	90	60
Iodine with6ml	50	60
Iodine with6ml	70	60
Iodine with6ml	90	60
Iodine with8ml	50	60
Iodine with8ml	70	60
Iodine with8ml	90	60
Iodine with10ml	50	60
Iodine with10ml	70	60
Iodine with10ml	90	60

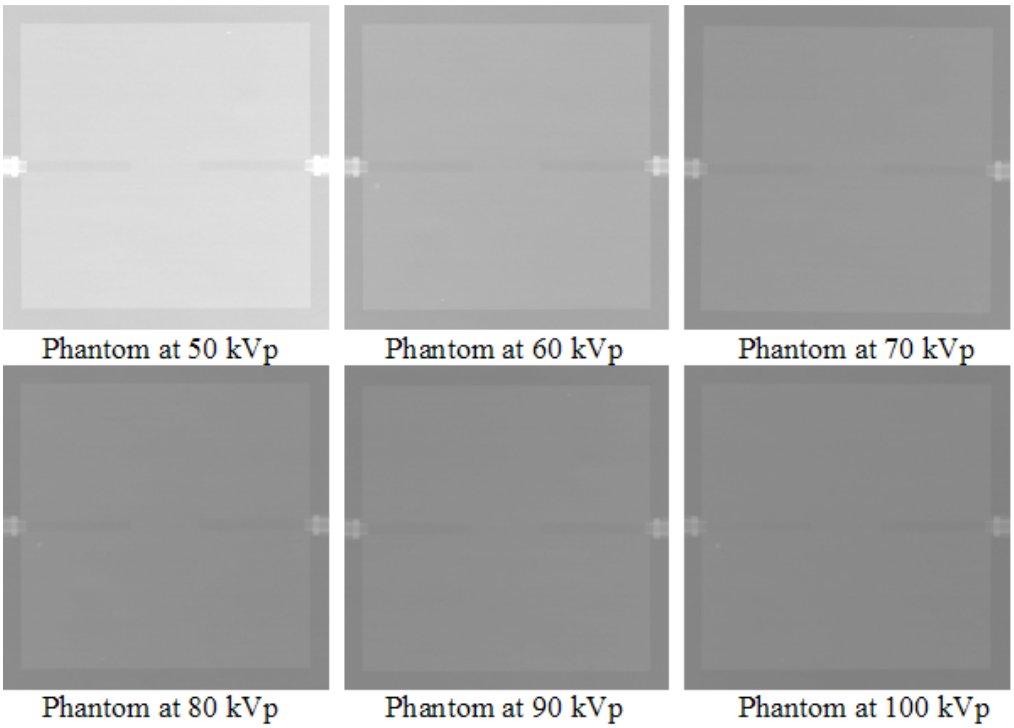

Figure 5.4 Images of the phantom taken at x-ray tube energies of 50, 60, 70, 80, 90 and 100kVp.

The phantom was filled with water and x-ray images were acquired at different x-ray tube energies. The results showed that the contrast decreased when the x-ray energy was increased, that is normal because the contrast taken between the water infused within the vessel and plexiglass. The difference of the contrast between them at low energy is small compare to the difference at high energy (Figure 5.5, p.121). Following this, the phantom was filled with iodine at different concentrations and additional x-ray images were acquired at different energies. The results showed that using low iodine concentrations with low x-ray tube energy gave good image contrast. Increasing both the iodine concentration and the x-ray tube energy also resulted in good image contrast (Figure 5.6, see following page).

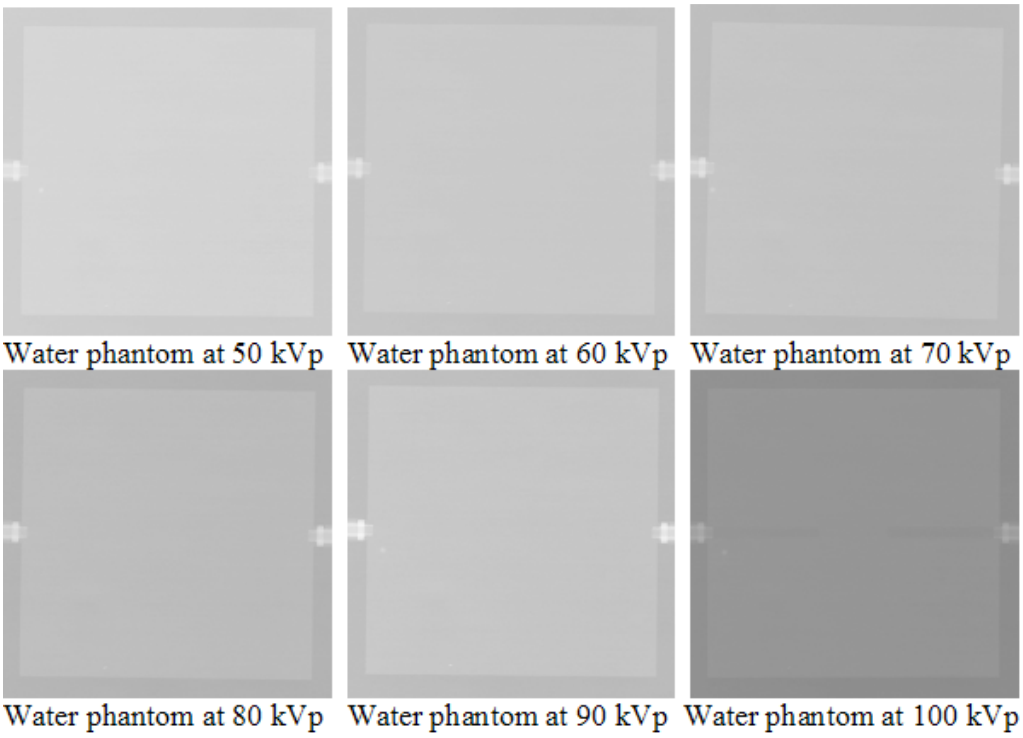

Figure 5.5 Images of the phantom filled with water taken at x-ray tube energies of 50, 60, 70, 80, 90 and 100kVp.

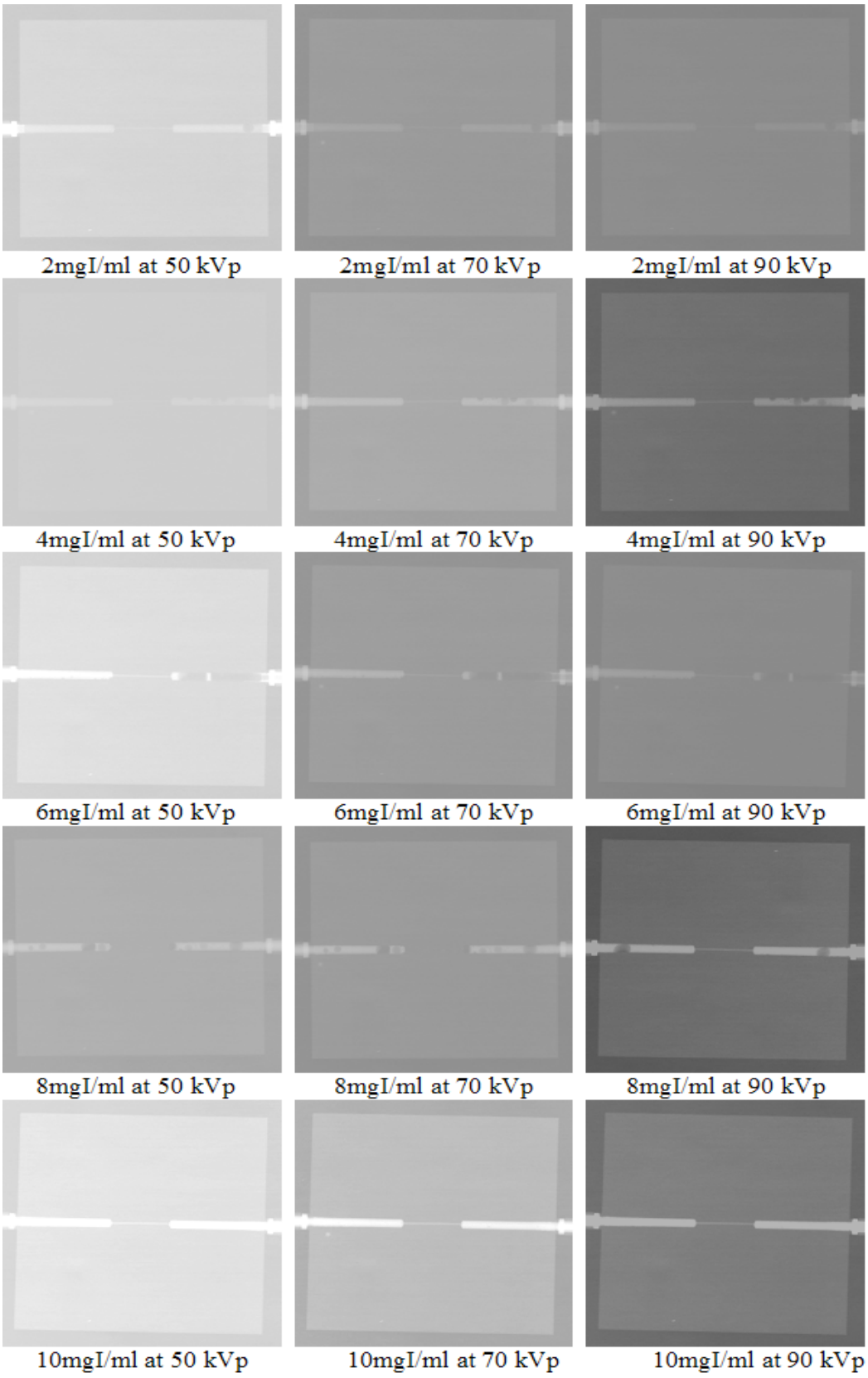

Figure 5.6 Images at different iodine concentrations and different energies.

5.3.3.2 Applying image subtraction

The images taken at the hospital are highlighted the use of contrast media. The image of the phantom filled with water was subtracted from the image having iodine contrast media, at different concentrations- from 2 mg/ml to 10 mg/ml of iodine at 50 kVp and 90 kVp as well (Figure 5.7 and Figure 5.8). The results showed that the images, taken at 50 kVp were much clearer than those at low energies. That is because the attenuation difference between the iodine and the water at high energy were too high compare to the difference at low energy.

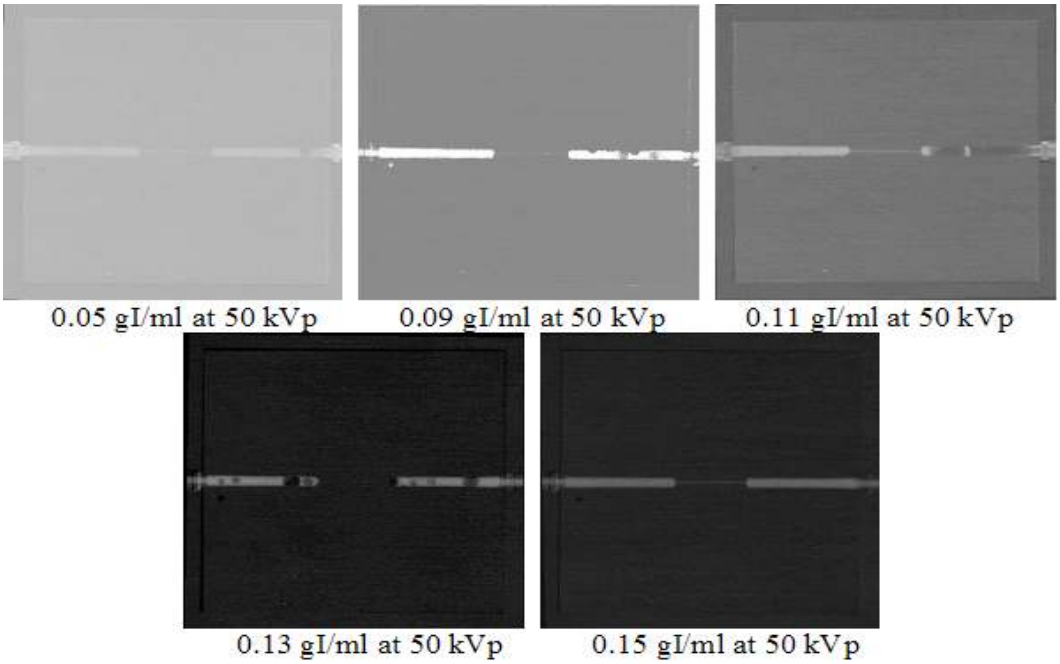

Figure 5.7 Images subtraction using different concentration of iodine contrast media subtracted from phantom filled with water at 50 kVp.

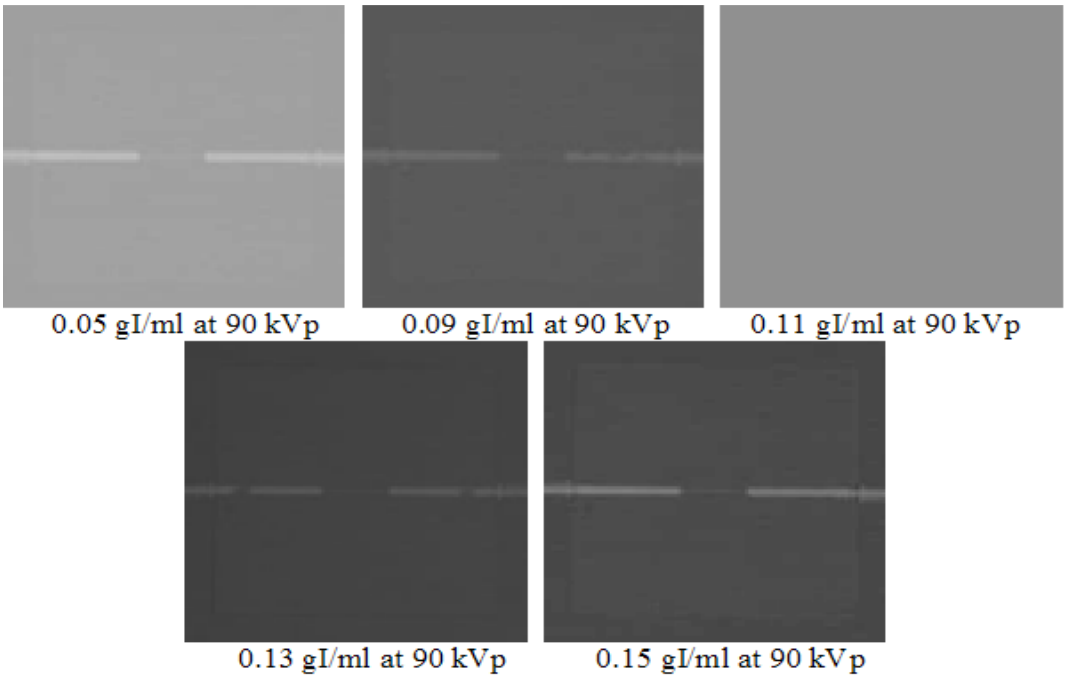

Figure 5.8 Images subtraction using different concentration of iodine contrast media subtracted from phantom filled with water at 90 kVp.

The experiment shows that the subtracted x-ray images acquired at low energy have better image contrast than the images taken in a single exposure without iodine. The contrast at low energy made between the phantom made of plexiglass and the air, showed that the difference between the attenuation is larger compared to the difference at high energy. When imaging the phantom filled with iodine, the difference in contrast was made between the iodine as a contrast medium and plexiglass. At low energy the difference between the attenuation between the phantom and iodine was small and the difference at high energy was notable. That was why we got better contrast (Figure 5.7)

5.3.3.3 Analysis

The linear attenuation coefficients μ of iodine at different energies calculated as in Table 5.2 ,p. 126. These data, cited from the National Institute of Standards and Technology 2004 (Farrell and Larter, 2006), were interpolated from mass

attenuation coefficients μ/ρ into linear attenuation coefficients after multiplying the mass by each component density, where the iodine density is 4.926 g/cm^3. The linear attenuation coefficient is the fraction of photons removed from a mono-energetic beam of x-rays per unit thickness of material (μ) cm^{-1}; whereas, the attenuation is caused by absorption and scattering of several interactions; Rayleigh scattering, photoelectric effect and Compton scattering. The values for the k-edges were not provided in the reference, and they were determined by interpolation.

Table 5.2 The Intensity calculated from linear attenuation coefficient of iodine, water and acrylic

Energy (keV)	μ/ρ (cm-1)	μI (cm-1)	XI (cm)	μI XI	μwater/ρ (cm-1)	μwater (cm-1)	Xwater (cm)	μwater X water	μAcrylic/ρ (cm-1)	μAcrylic (cm-1)	XAcrylic (cm)	μAcrylic XAcrylic	μI XI + μwater Xwater + μAcrylic XAcrylic	I/I0	-ln I/I0
50	1.23E+01	6.06E+01	0.0061	3.70E-01	2.27E-01	2.27E-01	0.094	2.13E-02	2.07E-01	2.90E-01	0.9	2.61E-01	6.52E-01	0.57	0.56
60	7.58E+00	3.73E+01	0.0061	2.28E-01	2.06E-01	2.06E-01	0.094	1.94E-02	1.92E-01	2.69E-01	0.9	2.42E-01	4.89E-01	0.67	0.40
70	5.55E+00	2.73E+01	0.0061	1.67E-01	1.95E-01	1.95E-01	0.094	1.83E-02	1.84E-01	2.57E-01	0.9	2.32E-01	4.16E-01	0.72	0.33
80	3.51E+00	1.73E+01	0.0061	1.06E-01	1.84E-01	1.84E-01	0.094	1.73E-02	1.75E-01	2.45E-01	0.9	2.21E-01	3.43E-01	0.77	0.26
90	2.73E+00	1.34E+01	0.0061	8.17E-02	1.77E-01	1.77E-01	0.094	1.67E-02	1.70E-01	2.37E-01	0.9	2.14E-01	3.12E-01	0.79	0.23
100	1.94E+00	9.55E+00	0.0061	5.83E-02	1.71E-01	1.71E-01	0.094	1.60E-02	1.64E-01	2.30E-01	0.9	2.07E-01	2.81E-01	0.81	0.21

The data in the table also shows the water mixed with the iodine contrast media and the plexiglass. The iodine contrast media used was Omnipaque, which has an iodine concentration of 300 mg/ml. The amount of 6.1 mg of iodine are calculated in volume of 1 mm^3, the intensities are calculated by knowing the density of the iodine in 1 mm^3 were the thickness of the plexiglass is 1cm (Figure 5.9). The calculation based on the values of the densities of iodine, water and acrylic is 4.92, 1 and 1.18 g/cm^3 respectfully.

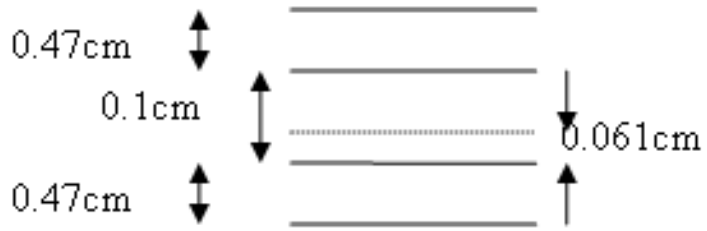

Figure 5.9 The dimension of the cubic cm of the blood vessel phantom filled with iodine contrast media with 300 mg/ml

The decrease in intensity I/I_0 was calculated from the optical density. The optical density is the measure of the transmittance of an optical element at a given wavelength λ. It is defined by taking the log of I/I_0. Later on we will use it to compare the data from the density of the images taken.

The intensity was plotted versus the energy. Figure 5.10 shows that as energy increases the intensity increases. The linear attenuation coefficient was plotted versus the energy for iodine, water and Plexiglas (Acrylic). The plot showed that the iodine absorption is higher than water and acrylic (Figure 5.11). The comparison of the calculated intensity for iodine, water and acrylic and the measured density from the blood vessel phantom at different energies and

concentrations was plotted, the intensity increases as the optical density decreases (Figure 5.12, p.129).

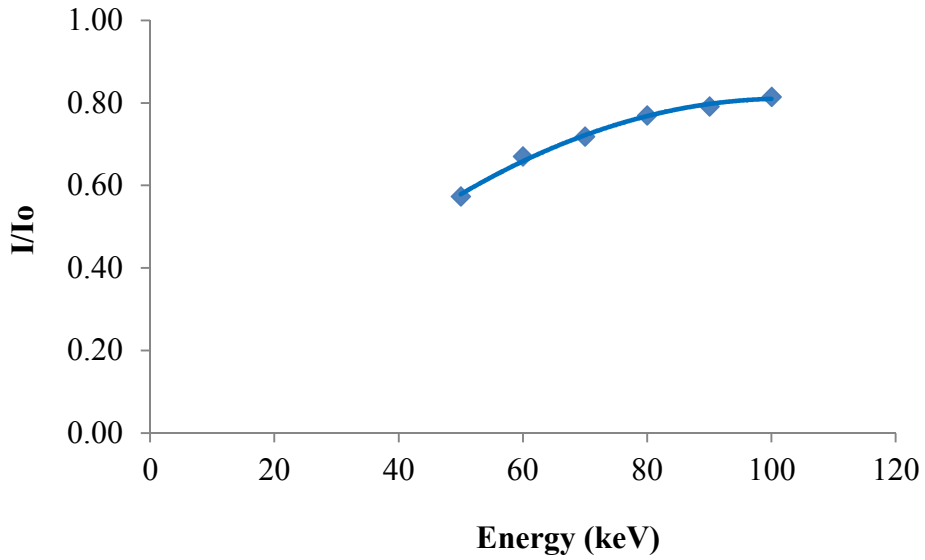

Figure 5.10 The intensity ratio I/I_0 for the phantom image filed with iodine contrast media

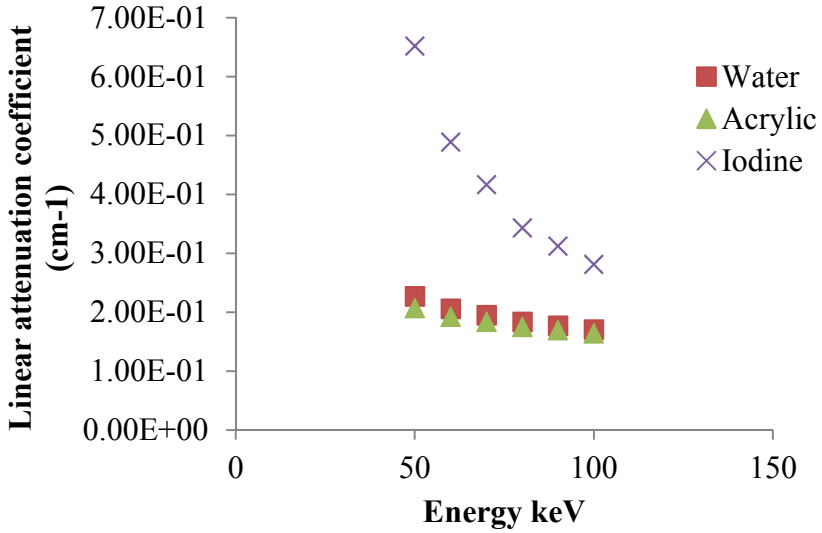

Figure 5.11 The comparison of linear attenuation coefficient of iodine, water and acrylic at different energies.

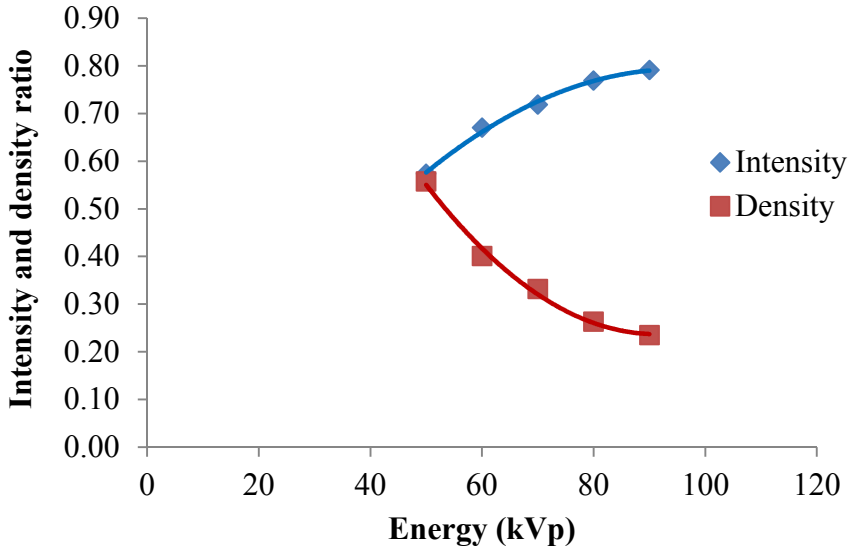

Figure 5.12 The calculated intensity and measured density comparison.

From the images taken at the hospital, and from the image viewer software used at the hospital the optical density was measured at each image. Initial optical densities were measured in an area outside the phantom. The optical density was measured at the centre of the blood vessel where the vessel size is 0.1 cm (Table 5.3, p.130), and at the ends where the blood vessel size is 0.4 cm (Table 5.4, p.131) the reading taken at different pixels and the average are taken.

Table 5.3 The densities of the phantom taken from the images at different energies and concentrations at 1 mm.

Energy (keV)	Concentration (g/ml)	Density at 1 mm phantom vessel thickness								
		D_{01}	D_{02}	D_{03}	$D_{0Average}$	D_1	D_2	D_3	$D_{Average}$	$D_{average}$-$D_{0Average}$
50	0.05	1.37	1.37	1.36	1.36	1.46	1.47	1.46	1.46	0.10
70	0.05	0.92	0.91	0.91	0.91	0.99	0.99	0.99	0.99	0.08
90	0.05	0.81	0.81	0.80	0.81	0.87	0.87	0.87	0.87	0.06
50	0.09	1.37	1.37	1.37	1.37	1.51	1.50	1.50	1.50	0.13
70	0.09	0.94	0.93	0.93	0.93	1.03	1.02	1.03	1.02	0.09
90	0.09	0.80	0.80	0.80	0.80	0.87	0.87	0.86	0.87	0.07
50	0.11	1.44	1.41	1.40	1.42	1.57	1.57	1.56	1.57	0.15
70	0.11	0.90	0.90	0.89	0.90	1.00	0.99	0.99	0.99	0.10
90	0.11	0.81	0.81	0.80	0.80	0.88	0.87	0.88	0.88	0.07
50	0.13	1.36	1.35	1.34	1.35	1.54	1.57	1.55	1.55	0.20
70	0.13	0.97	0.95	0.93	0.95	1.07	1.06	1.07	1.06	0.12
90	0.13	0.83	0.81	0.80	0.81	0.92	0.93	0.92	0.92	0.11
50	0.15	1.39	1.38	1.37	1.38	1.56	1.55	1.55	1.56	0.18
70	0.15	0.95	0.96	0.93	0.95	1.08	1.06	1.05	1.06	0.12
90	0.15	0.84	0.82	0.82	0.83	0.93	0.93	0.92	0.93	0.10

Table 5.4 The optical densities of the phantom taken from the images at different energies and concentrations at 4 mm.

Energy (keV)	Concentration (g/ml)	Density at 1mm phantom vessel thickness								
		D_{01}	D_{02}	D_{03}	$D_{0Average}$	D_1	D_2	D_3	$D_{Average}$	$D_{average}$-$D_{0Average}$
50	0.05	1.37	1.37	1.36	1.36	1.61	1.60	1.61	1.61	0.24
70	0.05	0.92	0.91	0.91	0.91	1.07	1.07	1.06	1.07	0.15
90	0.05	0.81	0.81	0.80	0.81	0.93	0.93	0.93	0.93	0.12
50	0.09	1.37	1.37	1.37	1.37	1.67	1.67	1.66	1.67	0.30
70	0.09	0.90	0.90	0.89	0.90	1.12	1.12	1.12	1.12	0.23
90	0.09	0.80	0.80	0.80	0.80	0.98	0.97	0.97	0.97	0.17
50	0.11	1.44	1.41	1.40	1.42	1.84	1.82	1.82	1.82	0.41
70	0.11	0.94	0.93	0.93	0.93	1.18	1.18	1.18	1.18	0.25
90	0.11	0.81	0.81	0.80	0.80	1.01	1.01	1.00	1.00	0.20
50	0.13	1.36	1.35	1.14	1.28	1.79	1.79	1.81	1.79	0.51
70	0.13	0.97	0.95	0.93	0.95	1.25	1.23	1.22	1.23	0.29
90	0.13	0.83	0.81	0.80	0.81	1.05	1.05	1.04	1.04	0.23
50	0.15	1.39	1.38	1.37	1.38	1.90	1.85	1.84	1.86	0.49
70	0.15	0.95	0.96	0.93	0.95	1.31	1.26	1.26	1.28	0.33
90	0.15	0.84	0.82	0.82	0.83	1.11	1.07	1.07	1.08	0.26

A mixture 2 ml of the omnipaque iodine contrast was diluted in 10 ml of water so the concentration equal 0.05 gI/ml. This mixture was injected in the phantom. The optical density was plotted against the energy at 1 mm thick of the blood vessel. It showed the expected curve: the curve increases as the iodine concentration increases see Figure 5.13.

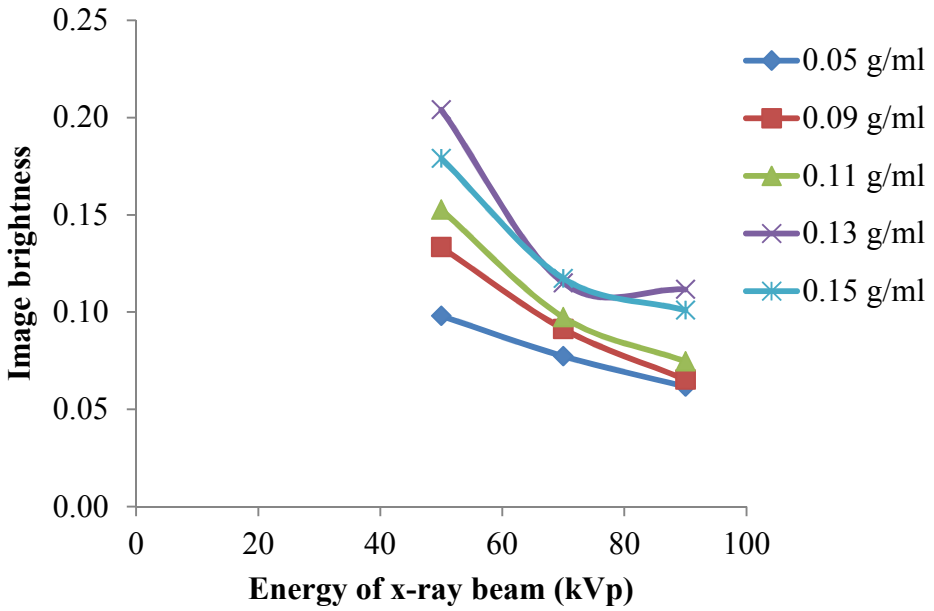

Figure 5.13 The optical density ratio taken at 1mm of the phantom filled with iodine at different beam energies and iodine concentrations.

The optical densities were also plotted for the 4 mm thick blood vessel. The results showed better fit of the different concentration of iodine and it also showed that by increasing the iodine concentration the curve increases (Figure 5.14).

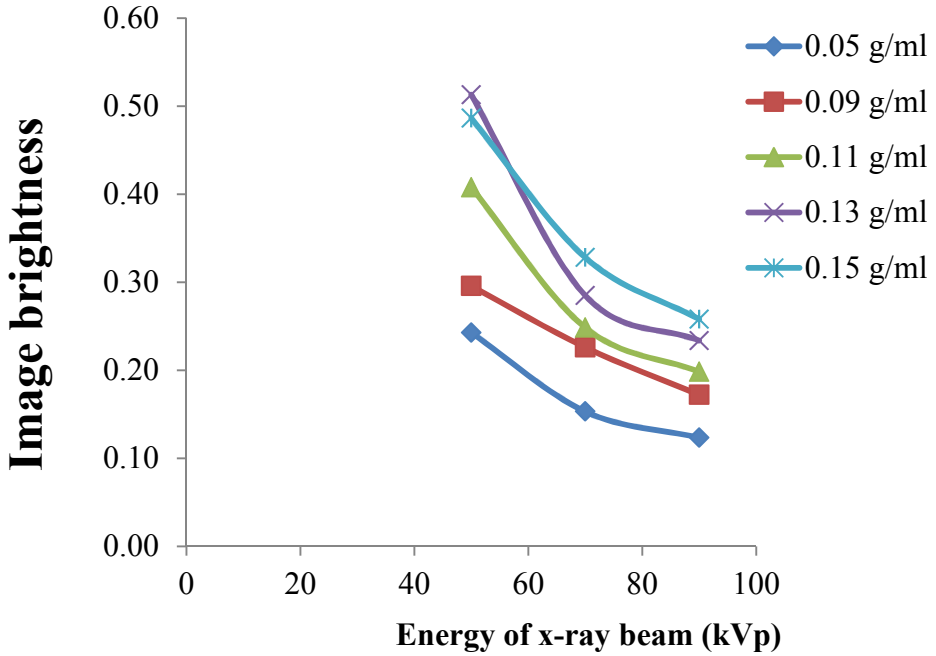

Figure 5.14 The optical density ratio taken at 4 mm of the phantom filled with iodine at different beam energies and iodine concentrations.

The optical density data obtained theoretically are compared with the density obtained from the images of blood vessel phantom at different iodine concentration and energies. The comparison shows acceptable fit. We can see that the calculated densities are match at concentrations of 0.15 and 0.13gI/ml and the remaining concentrations the curves are almost close as shown in Figure 5.15 .

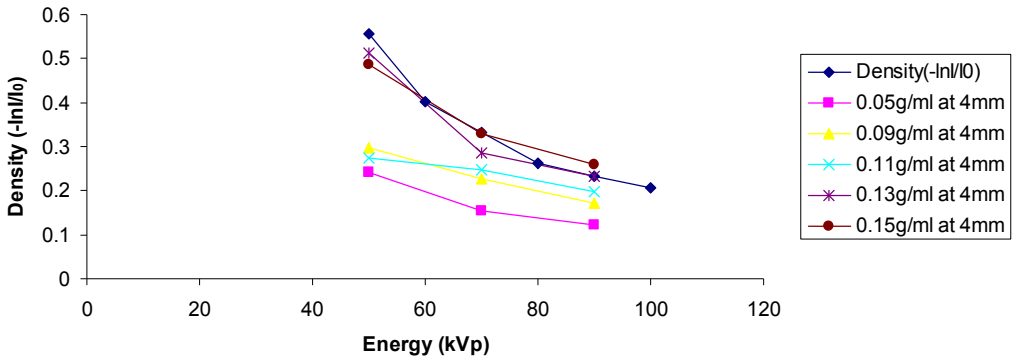

Figure 5.15 Comparison of the calculated density and the optical densities from the images at different concentrations taken from 4mm thick of the phantom.

5.4 Summary and conclusions

This chapter has described a software tool developed to perform dual energy image subtraction, which is used to improve the visualisation of blood vessels in the body. The program has been developed in such a way that it can take any type or size image and apply image registration techniques to the images so that the subtraction can be performed. After initial testing to check that the application could load and manipulate different types and sizes of images, x-ray images of a blood vessel phantom were taken at the Christchurch Hospital using different choices of parameters such as; iodine concentration: 5-8 g/ml, and x-ray energy: 50 - 100 keV. This software tool helps us to enhance the contrast of the subtracted images at the k-edge of iodine contrast media. This contrast improvement is clearly shown in Figure 5.3.

X-ray images of the blood vessel phantom were acquired and used to demonstrate that the program can be used to enhance image contrast by performing image subtraction between images acquired under different x-ray exposure conditions. The subtraction can be made, either by subtracting images from two exposures having different energies (as has been done in this chapter) or subtracting images from a single exposure, taken above and below the k-edge energy of the iodine contrast media.

Knowing the linear attenuation for iodine, water and plexiglass the optical densities were compared with those measured from the images taken using the blood vessel phantom. I have shown that the image brightness (contrast) increases with iodine concentration, and brightness is greater with lower x-ray beam energy in both the subtracted and original images.

The film processing of the x-ray images acquired varied from image to image. Consequently, the acquisition and processing of images should be repeated under more controlled conditions. In addition, while ideally the iodine contrast media should fill the phantom, the bubbles that can be seen in some images do not need to be removed as other areas of the image can be used by selecting a region of interest.

In future, the program could be developed further so that it can link directly to the x-ray machine detector or, in the case of Medipix2, another program code could be used to take into consideration the time of reading the data, which is useful in angiography. The software could apply spectral imaging techniques by using two images taken at different energies, one, at an energy below the k-edge of iodine, and the other at an energy just above the k-edge. The output image could be reconstructed on the screen in order to enhance the contrast, and the subtraction made to get the blood vessel image.

Chapter 6

6 An analysis of the fat contents in liver tissue

This chapter reviews the pilot study by (Berg et al., 2009) and extends this work by providing a statistical analysis of the experimental data. Based on this analysis the absorbance plot was modified uncertainty of estimated liver fat contents was reduced. The modified absorbance plot provides improved (Berg et al., 2009).

This analysis provides information useful for planning the next stage of experimental studies and for developing spectral analysis techniques to distinguish between Fat and Liver using the MARS-CT system.

6.1 Preliminary study to quantify fat, iron and calcium contents by spectroscopic-CT

This study was performed to quantify whether fat, iron and calcium could be distinguished using spectroscopic-CT acquired using the MARS2-CT scanner. An improved method for quantifying fatty liver was developed, using photon attenuation curves for fat and liver tissue measured using the MARS2-CT system

Sheep liver and fat tissue, were chosen to perform the initial studies as these tissues were readily available from the local supermarket. The tissue samples were prepared in forms with constant thickness and fit in the Perspex tube for the scanner. The samples were cut into cylinders, each having the same diameter, and placed in syringes, one for each tissue of either liver or fat. The other sample was prepared by combining equal weights of fat and liver tissue in a blender, which were pureed and then placed into a syringe.

6.2 Measuring and identifying the photon absorbance curve

The photon absorbance curves were constructed by acquiring photon counts for x-rays passed through a syringe of tissue, which were then normalized using the count from x-rays passed through an empty syringe. The syringes completely covered the area of the detector, so the transmission values obtained from these measurements should be specific to the tissue.

The Medipix2 detector was used to acquire the photon count data for energy bins with a width of 2.5 keV. Low energy thresholds of 17.5, 20, 22.5, 25, 27.5, 30, 32.5, 35, 37 and 40 keV (noise floor was currently 17 keV) were used. The exposure time for each energy, was set so that the counts through the empty syringe were about 3000 to compensate for differences in detector efficiency at each energy. Each measurement of count rate was repeated 10 times.

At the time this work was carried out it was common practise to operate the Medipix2 detector thresholds so that photons between the low threshold and the kVp energy of the x-ray tube are counted. This means that count data for each energy scanned must be normalised to a common exposure time using the acquisition times for each energy level (in this case to normalised units of counts/s). Following normalisation, the count data for adjacent energies are subtracted to get to count rate for each energy bin (e.g. counts for 20 keV are subtracted from the count for 17.5 keV to get the count rate for the 17.5-20 keV bin).

The counts of photons transmitted through the fat and liver syringes were normalized using the count of photons through the empty syringe. Finally, the negative logarithm was taken to get absorbance values (Figure 6.1).

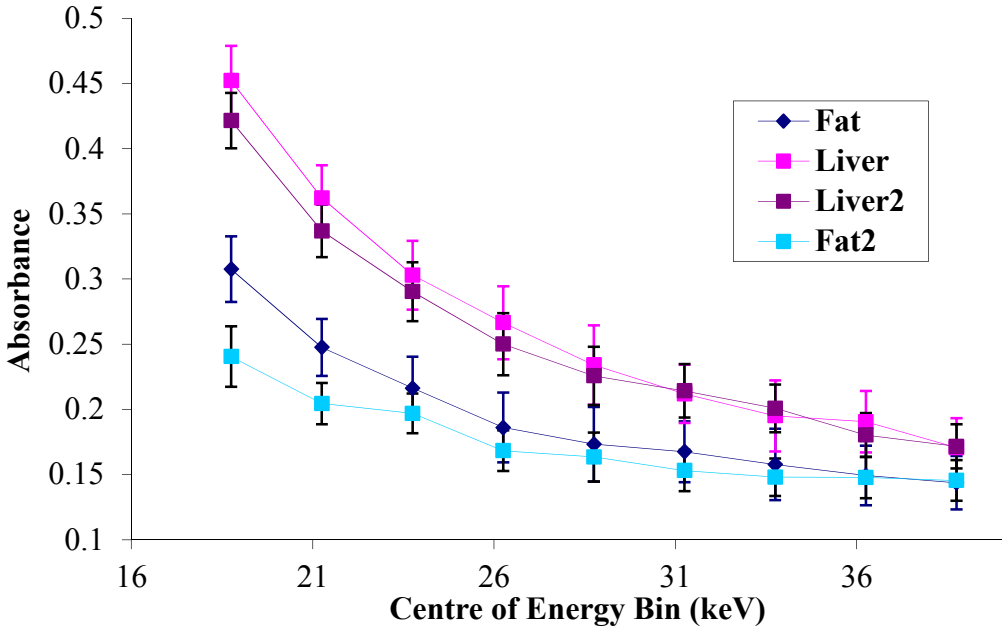

Figure 6.1 Absorbance curve for Sheep Fat and Liver using MARS2-CT

The photon absorbance curves for fat and liver obtained from the experimental measurements using the MARS2-CT have a similar shape to tabled data for fat and water found in. This is a promising result.

In order to distinguish liver and fat by their spectroscopic properties over this energy range, the ratio of liver to fat absorbance for any particular energy would need to be different across the energy range within the error of MARS2-CT. The data in Figure 6.1 suggests this is the case for low x-ray energies but that there is no significant difference at higher energies.

The liver to fat absorbance ratio decreased with increasing energy for all four possible liver/fat pairs. An estimate of the error in measurement was obtained by taking the standard deviation of the ten measurements and propagating the error through the calculations. Within this error, fat and liver had clearly different absorbance or attenuation for the same length of tissue, and displayed spectroscopic differences.

A second set of liver and fat samples were scanned to provide information about variation of liver and fat tissue absorbance between individuals (from sheep to sheep). The calculated absorbance curves are also shown in Figure 6.1, and show only minor differences between the first and second set of measurements.

The accuracy of measurements using sampled data is related to the standard deviation of the mean, which is related to the standard deviation of the sample distribution by:

$$\sigma_{\mathbf{mean}} = \frac{\sigma}{\sqrt{N}} \qquad (1.)$$

It is clear from (1) that the measurement error for a sample of 10 repeated measurements is $\frac{1}{\sqrt{10}}$ that of a single sample (a useful reduction is our case although requiring additional time and radiation exposure to acquire the data). The absorbance curves were recalculated using the 10 repeated measurements, and are shown in (Figure 6.2). The results show the (expected) significant reduction of the measurement error. In particular it can be noted that significant differences between the absorbance of fat and liver samples can be observed at higher energies than was the case when calculating absorbance using a single measurement. This is a promising result for spectral CT applications since each voxel in reconstructed image is formed using several hundred (or more) projections from different angles.

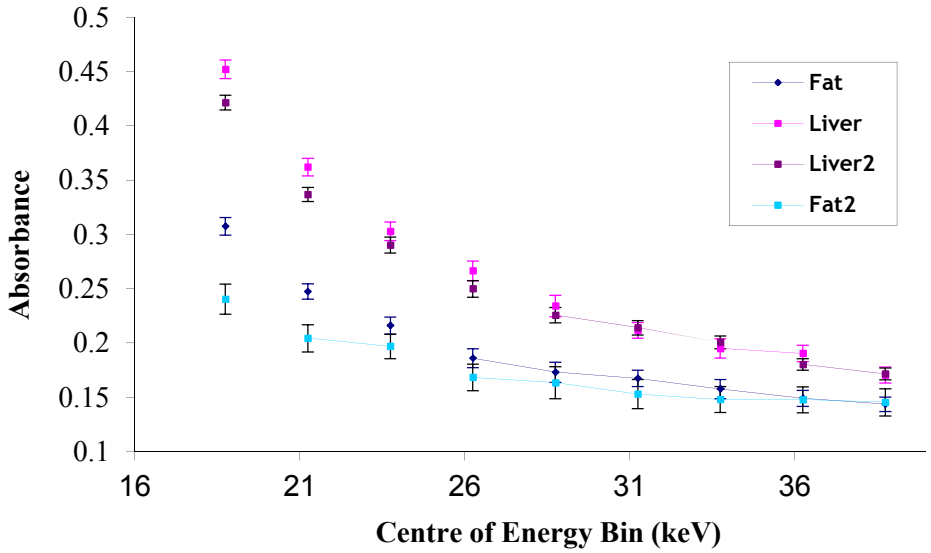

Figure 6.2 Modified absorbance curve for sheep fat and liver using MARS2-CT.

6.3 Summary and discussions

I performed studies on the potential of MARS-CT to quantify the fat content of liver tissue. Linear attenuation curves for fat and liver tissue were defined. I was able to develop a protocol for producing linear attenuation curves from projection images on MARS-CT with a very small error in measurement.

There are two potential avenues for improved quantification of fat in the liver. The first is that the difference in linear attenuation between fat and liver at low energies is large, and the blend shows an intermediate attenuation. Whereas traditional CT measures attenuation over a broad range of energies, use of a low energy bin and a calibration curve of liver/fat blends should allow development of a quantification method for fat in the liver. The second is that although the curves do not appear to differ spectroscopically within the energy range measured, we know they must differ at higher energies due to the dual CT studies (Raptopoulos *et al.*, 1991) and at lower energies where the k-edges of biological elements lie.

The analysis presented in this chapter shows that there is a significant difference in linear attenuation between fat and liver, due to the difference in density of the tissues. However over this energy range the spectra themselves are not largely different by inspection. This can be observed by noting that the attenuation value of liver seen in Figure 6.2 always roughly twice that of fat over the measured energy range. Although, this does not preclude significant differences between the spectra over the 10 keV to 100 keV range.

The difference in linear attenuation between fat and liver at low energies is quite large and, it is linear attenuation in this energy range that provides differentiation between fat and liver tissue in CT images. The analysis of this experimental data indicates that significant differences in the measured attenuation of liver and fat can be obtained by the use of narrow energy bins at low energies, as opposed to using traditional broad spectra CT techniques.

Consequently, this analysis has demonstrated that the information about the attenuation of fat and liver tissues at different energies obtained from projection images can in theory be used to distinguish these tissues in images. And, shows that the measurements of x-ray attenuation by fat and liver tissues using the MARS-CT scanner are sufficiently accurate to justify further investigation into developing practical imaging techniques based on the energy dependent differences in the x-ray attenuation of (soft) tissues.

Chapter 7

7 A method for performing flat field correction of images

This chapter reviews a previous study of artefacts in images acquired on MARS CT systems, how these artefacts affect image quality, and the solutions for reducing artefacts. The previous study geometry used open beam images have been acquired (without an attenuating specimen between the x-ray source and the detector), the images taken for one detector stop (Aamir *et al.*, 2011), while this chapter show how the code developed to correct the flatfield at three detector stops in order to cover large sample size where the code applicable to use for more than three detector stop.

7.1 Introduction

The Medipix detectors are single-photon counting detectors which convert x-rays into electron-hole pairs , these detectors are referred to as hybrid detectors because they have two layers connected via bump bonds (Mikulec, 2003). A bias voltage is applied to the sensor to transfer charge to the readout chip.

In Medipix detectors, the sensor and readout chip usually have pixels of the same size. Thus a photon impinging on one pixel of the sensor will be counted by the corresponding pixel of the readout chip, due to the influence of charge sharing between the adjacent pixels, very often the photon is recorded in several pixels (Giersch *et al.*, 2004).

The selection of the semiconductor sensor material depends on the application. Silicon is used due to the availability of high quality homogeneous material with few defects and high transport properties of the charge carriers around 1 cm^2/V.

However, for a 300-μm-thick sensor, its x-ray absorption efficiency is less than 30% for energies above 20 keV and less than 5% above 40 keV (Mikulec, 2000); this is due to the low atomic number of Si (Z=14), which make it good to study fatty liver. Other materials, such as GaAs and CdTe, have also been realized and tested. These show good detection efficiency for energies up to 100keV, making them suitable for medical imaging (Limousin, 2003, Zwerger *et al.*, 2007).

CdTe sensors have been processed with pixel contacts and passivation, and bump-bonded to Medipix2 readout chips. Open beam images have been acquired where the specimen placed between the x-ray source and the detector using the MARS-CT scanner system.

The aim is to review the preliminary analyse the behaviour of the individual pixels (55×55 μm^2) of the CdTe sensor as well as comparing their response to that of neighbouring pixels. The preliminary study used a broad spectra x-ray source and to apply the developed Matlab code to correct the flat field at one detector stops (Aamir *et al.*, 2011). This study will develop the Matlab code to correct the flat field at three detector positions or more to enable scanning large sample.

7.2 Set up Parameters

A 1-mm-thick CdTe sensor bump-bonded to a Medipix2 readout chip was used, operating at a -300 V bias voltage in electron collection mode. The detector was flood irradiated using a poly-energetic x-ray beam produced by a Thermo scientific Kevex PXST-150-75 x-ray tube, which has a tungsten (W) target and 0.5-mm Al equivalent filtration. The x-ray tube was operated at a voltage of 75 kVp and current of 150 μA. The source to detector distance was 115 mm.

The image readout from the Medipix2 detector was performed using the MUROS2 (San Segundo Bello et al., 2003). The threshold levels of the energy discriminator in each pixel were equalised with respect to the noise edge using the Pixelman software (Holy et al., 2006).

A three hundred and three flood frames for each stop (The scan was run for three stops) were obtained with the low threshold set to eight and an exposure time of each acquisition of 35 ms; the total scanning time was around 9 minutes, over which time the x-ray output is measured to be stable (see Table 7.1) and the same set up used to scan tube filled with sheep liver and fat (from supermarket), the aim of this scan is to compare the images after correct the flat field. The thresholds of the CdTe sensor layer has been calibrated by the MARS-CT group Table 7.2.

Table 7.1 Scanner parameters

Parameter	Value
Type	137
Fprintf	2010_12_02_Liver_fat_paper_CdTe_3 Stops\n
parameters.projections	303
parameters.energy	[465;490;515;540;565;590;615;640;665;690;715;740]
parameters.time	[21.58;23.56;27.51;29.49;31.47;33.45;35.42;37.40;39.38;41.36;43.34
parameters.stops	3
parameters.overlap	10
parameters.flatfields	100

Table 7.2 Energy calibration using CdTe Chip

THL Value	x-ray energy (keV)
465	21.58
490	23.56
515	25.53
540	27.51
565	29.49
590	31.47
615	33.45
640	35.42
665	37.4
690	39.38
715	41.36
740	43.34

7.3 Background

A typical image is shown in Figure 7.1, (Aamir *et al.*, 2011) analysed the sensitivity of a CdTe sensor using one hundred flood images, obtained using the parameters in Table 7.1 and Table 7.2. The study showed that the mean count rate of the detector is 3073±393 count/pixel across the hundred frames studied. And, reveals pixels with unexpected responses such as pixels that have zero count (dead pixels), pixels that have either low or high counts, and pixels that form a wrinkle pattern due to variations in the CdTe sensor layer. It is important to analyse the behaviour of pixels in the detector and to apply the knowledge gained to develop techniques for improving the quality of images.

The previous study by (Aamir *et al.*, 2011) has shown the inhomogeneity in the CdTe sensor and by knowing the behaviour of the pixels within the detector, thus we need to correct the flat field to improve the image. To correct the flat field I used to correct the detector and beam profile and apply both correction maps to

the image process to get the corrected image which should be clear compare to the uncorrected image.

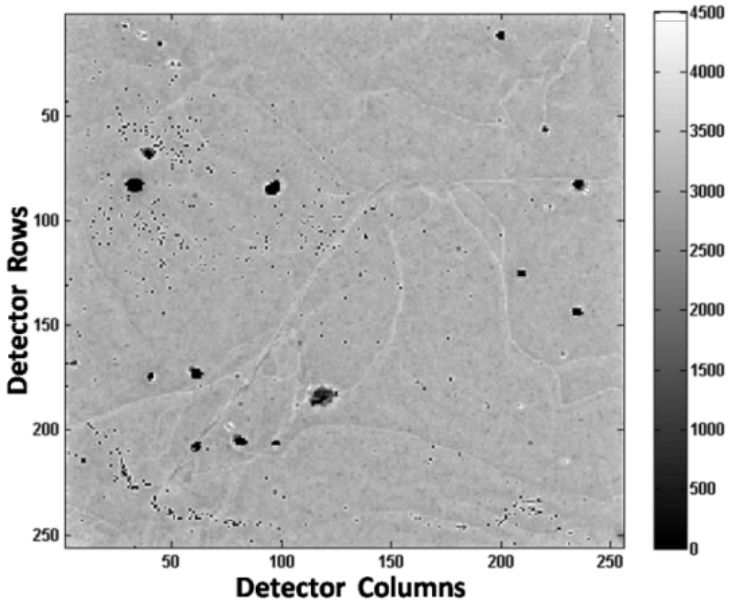

Figure 7.1 A flood image taken with CdTe, original flat field before applying the correction.

7.4 Detector correction

The correction map is obtained by taking the ratio of the median counts over 303 frames for each pixel to the median counts averaged over the whole detector. We use median rather than mean to remove outliers. The correction map consists of a coefficient for each individual pixel. By dividing the raw data by this correction map, counts for higher in the sensitivity pixels are reduced while the counts in the lower sensitivity pixels are increased. There are some regions where pixel sensitivity is so low that correction is difficult. Figure 7.2 shows the profile across column 114 for 303 frames before and after this flat field correction and the Matlab code written are shown in APPENDIX B.

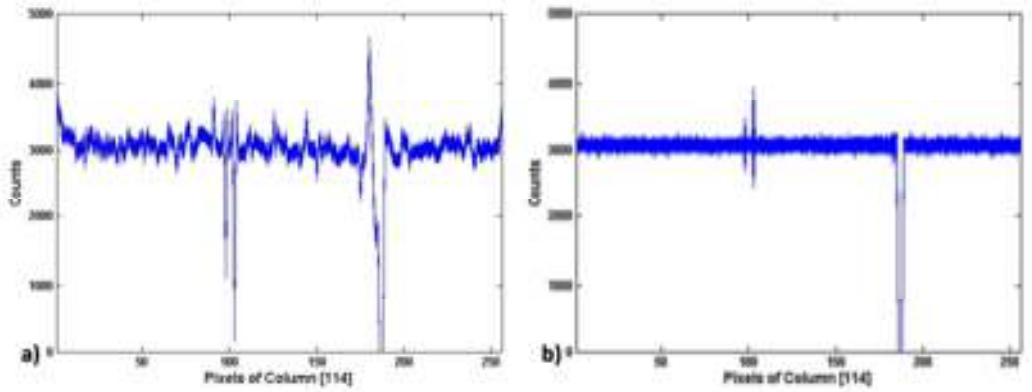

Figure 7.2 The profile across column 114 of the detector shows the sensitivity (a) before calibration, and (b) after sensor calibration.

7.5 Beam profile correction

The ideal position for the detector is face to the x-ray tube where the intensity is high at the centre this is the case when scanning small sample but for large sample the detector need to be moved to cover whole the sample. In this study I used three stops to cover the large sample and to correct the beam profile, where when the detector move up the detector behave are not the same, to correct the beam profile the Matlab code are wrote to apply polyfit. Figure 7.3 showed before and after correction of the beam profile which allows each corresponding pixel behave the same response.

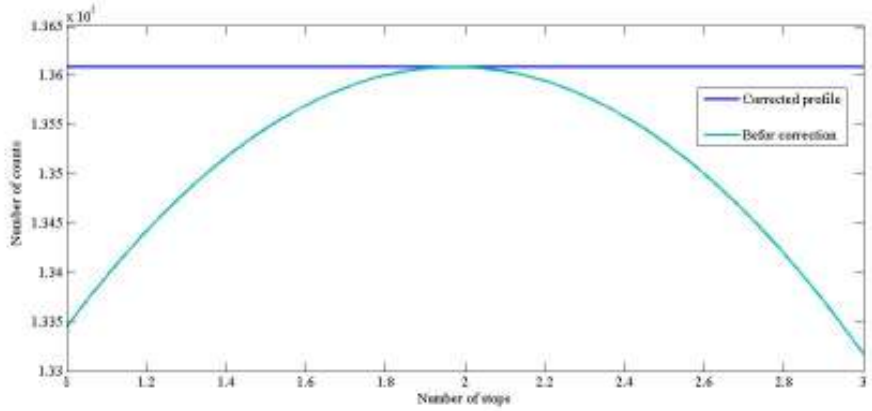

Figure 7.3 Beam profile correction map, before and after applying the correction code.

I apply the detector correction and beam profile correction to the original image. The image of tube filled with fat and liver where the fat warped with foil of paper to easy distinguish the fat from liver, the sample place between the x-ray source and the detector.

The average image was corrected by generating a correction map from an average image of 303 frames and three detector stops open beam images. The same parameters were used as previously described. Figure 7.4 shows (a) the image before applying the flat field correction and (b), the corrected image of the Fat and liver tube. This code is applied only when use three detector stop or more, not less as the polyfit function requires at least two points. The corrected image shows a clear improvement in image homogeneity with the wrinkle pattern removed. The modified Matlab code used to correct the detector and beam profile is provided in an APPENDIX B.

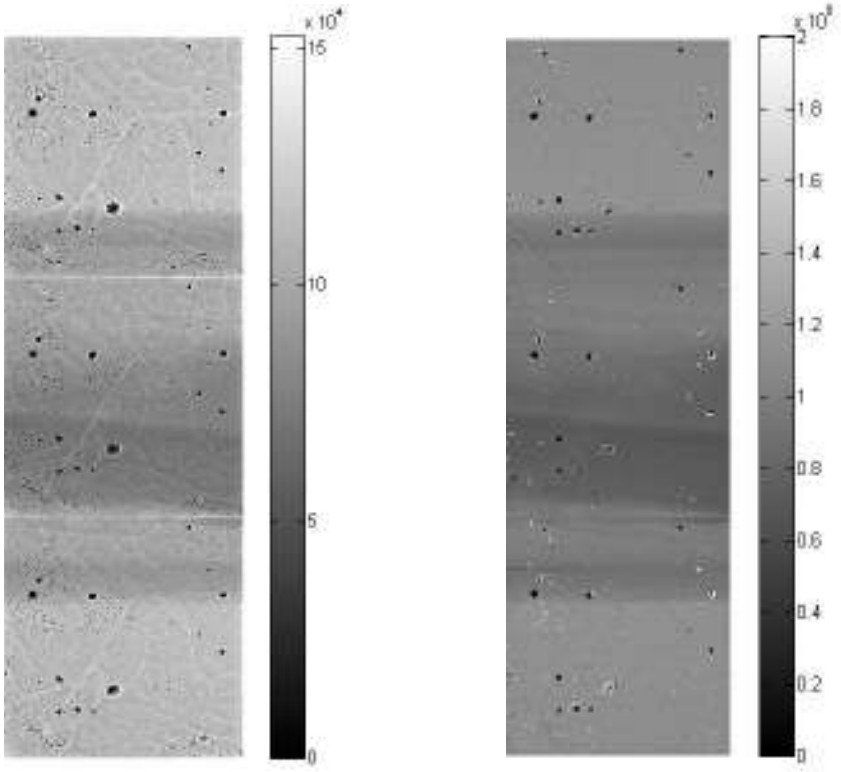

(a) Original image (b) Corrected image

Figure 7.4 Images of a fat and liver sample obtained (a) before correction for detector response and (b) after applying correction for detector response of individual pixels and x-ray beam profile.

7.6 Summary and discussions

This experimental study, has characterized a 1-mm-thick CdTe sensor bump bonded to a Medipix2 chip. To do this the sensitivity of 196608 pixels over three hundred frames and three detector positions was studied, showing a high degree of repeatability of pixel performance over one hundred consecutive exposures. Flat field corrections to images were performed these corrections were demonstrated to improve image quality. The correction code differs from previous code developed by (Aamir *et al.*, 2011) in that it allows correction of images combined from three detector stops and more (to cover a large field of view). However, dead regions still remain.

To use CdTe-Medipix assemblies for CT, where a volumetric reconstruction is obtained from a large number of projection images taken at different angles, correction strategies are based on the requirements of the reconstruction technique. For filtered back projection a complete projection without missing data is generally required. In this case it is possible to interpolate the missing data, e.g. by linear interpolation across the dead region. Real data of the object is then obtained with the detector at a different gantry angle or bed location. While the interpolation will introduce some noise or artifacts, the large number of projections minimizes these. For mathematical reconstruction techniques missing data from dead regions represent rays with no information. These few rays are simply removed from the large set of equations.

By using the improved image correction methods presented in this chapter I was able to remove some of the wrinkle patterns and other artefacts that are caused by inhomogeneity in the CdTe sensor, which can be seen in Figure 7.4 (p.149). The dark response of pixels was investigated, a few pixels are observed to give non-zero counts even with no photons hitting the detector (dark counting). These dark counting pixels are treated as missing, consequently for image reconstruction methods that require all pixels to have a valid value (such as filtered back projection), the value of dark counting pixels is obtained by interpolation over neighbouring pixels.

Chapter 8

8 Evaluation of the MARS-CT2 for measurements of fat in liver.

8.1 Introduction

This Chapter presents experiments performed to develop an improved method for quantifying fat content in liver, and investigates whether fat and liver tissue can be distinguished by spectroscopic-CT. Section 8.2 describes the MARS-CT2 system configuration used for these pre-clinical investigations, and presents the processing steps that are necessary to create a tomographic reconstruction from the raw data acquired on the MARS-CT2 scanner.

8.2 Materials and methods

8.2.1 Overview of scans performed

A series of three scans was performed. Each scan was of the same fat and liver tissue sample but was carried out using different versions of the Medipix2 detector over a range of energies compatible with the sensor material, which was either Si, GaAs, or CdTe. Where possible the scan parameters were kept common for all scans. However, the three different detectors utilise sensor materials that differ in quantum detection efficiency, and quality of manufacture and assembly. Consequently, some parameters were adjusted to achieve approximately 3000 counts per pixel for all scans, and to account for oversampling needed to compensate for bad pixels arising from manufacture.

8.2.2 The MARS-CT2 system

The sample was scanned on the MARS-CT2 system, which is comprised of a Medipix2 detector ASIC (application specific integrated circuit) bump bonded to

a semiconductor conversion layer. Three different versions of the detector were used each with a different conversion layer, which was either a 1 mm thick GaAs sensor layer, 300 μm Silicon or 1 mm CdTe. The x-ray tube was a Kevex PXS11-150-75, this x-ray tube, which has a tungsten anode target, and inherent beam filtration of 0.5 mm aluminium, was set to operate at a tube voltage of 75 kVp and tube current of 0.15 mA. Other components of the MARS-CT system included the power supply, x-ray controller, motor controller, MARS readout out system (MUROS) and unit processing computer (UPC) Figure 3.3. The Medipix2 detector exposure time was adjusted to read approximately 3000 counts per pixel for open beam conditions. To enlarge the field of view for each projection, the sensor was moved to three overlapping positions. In total, data for 303 projections was acquired. The focal spot of the x-ray tube was 40 mm, the magnification factor of MARS-CT2 system is 1.41 and an isotropic voxel size of 43 μm^3. The flat field correction for each detector positions was performed after sample scan without attenuating sample.

Sample preparation

A sheep liver and fat sample was sourced from the local supermarket and cut in to small pieces. For the first scan, which was performed using the GaAs Medipix2 detector, the sample was placed in a 1.4 cm diameter tube and a paper clip was placed between the fat and liver for visual separation as shown in Figure 3.3, p52. The metallic paper clip did not provided a particularly good means of visually identifying the separation between the fat and liver sample and introduced artefacts into the image, consequently the sample preparation method was

modified for the scans using the CdTe and Si detectors[3]. For these scans, the fat was wrapped by a thin layer of white paper and the liver wrapped with monofilament fishing line. Additionally, a plastic tube filled with water was placed between the fat and liver to provide a calibration reference point for converting the reconstructed images to Hounsfield units. The modified sample preparation is shown in Figure 8.2 (see following page).

Figure 8.1 The prepared sample, showing the tube holding the fat and liver, which are separated by a paper clip.

[3] The GaAs detector had been removed from the scanner system and was not available for the scan to be repeated with the revised sample preparation technique.

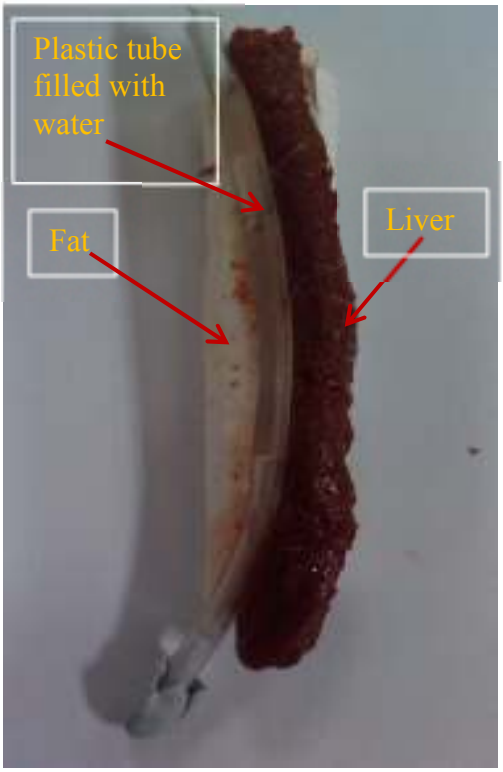

Figure 8.2 The prepared sample showing the fat wrapped with thin paper, the liver folded with fishing monofilament and the water filled plastic tube.

8.2.2.1 Acquisition of CT images using a Medipix2 detector with GaAs sensor

The system parameters used to acquire the scan using the GaAs Medipix2 detector are shown in Table 8.1, and Table 8.2.

Table 8.1 Parameters for the fat/liver scan using GaAs - Medipix2 detector

Parameter	Value
Total no. of projections	303
Stops	3
Overlap	66
No. of flatfield images	100

Table 8.2 Energy calibration data and exposure time for the GaAs - Medipix2 detector

THL Value	x-ray energy (keV)	Exposure time (ms)
560	14.45	200
580	18.0	250
600	21.5	300
620	25.0	350
640	28.6	500
660	32.0	700
680	35.6	800
700	39.2	1300

8.2.2.2 Acquisition of CT images using a Medipix2 detector with a Si sensor

The system parameters used to acquire the scan using the Si Medipix2 detector are shown in Table 8.3, and Table 8.4.

Table 8.3 Parameters for the fat/liver scan using Si - Medipix2 detector

Parameter	Value
Total no. of projections	303
Stops	2
Overlap	12
No. of flatfield images	100

Table 8.4 Energy calibration data and exposure time for the Si - Medipix2 detector

THL Value	x-ray energy (keV)	Exposure time (ms)
625	8	600
577	15	1000
530	22	2000

8.2.2.3 Acquisition of CT images using a Medipix2 detector with a CdTe sensor

The system parameters used to acquire the scan using the GaAs Medipix2 detector are shown in Table 8.5and Table 8.6.

Table 8.5 Parameters for the fat/liver scan using CdTe - Medipix2 detector

Parameter	Value
Total no. of projections	303
Stops	2
Overlap	10
No. of flatfield images	100

Table 8.6 Energy calibration data and exposure time for the CdTe - Medipix2 detector

THL Value	x-ray energy (keV)	Exposure time (ms)
465	21.58	33
490	23.56	43
515	25.53	55
540	27.51	75
565	29.49	104
590	31.47	146
615	33.45	210
640	35.42	290
665	37.4	392
690	39.38	570
715	41.36	804
740	43.34	1160

8.2.2.4 Measurement of ambient operating temperature in the MARS-2 CT scanner

Ambient temperatures inside the MARS-CT scanner during operation were measured due to concern about elevated temperatures resulting from heat dissipation by the x-ray tube, and the effect this could have on biological samples. Several thermocouples were placed into the scanner to measure temperature changes during operation, the first thermocouple was placed in front of the x-ray

tube and the second one placed inside on the base of the scanner as shown in Figure 8.3.

Figure 8.3 The thermocouple placed in the scanner to measure the temperature variation when the scanner at operation.

The scanner was operated for 50 minutes and temperature readings were taken every 5 minutes. The measurements show only a small increase in temperature that is unlikely to affect the sample during the scan (Table 8.7, and Figure 8.4).

Table 8.7 Temperatures inside the operating scanner measured times from 0 to 50 minutes from the start of scan operations. T_1: Temperature outside the tube (°C), T_2: Temperature inside the tube (°C)

Time (min)	T_1: outside the tube (°C)	T_2: inside the tube (°C)
0	23.5	22.9
5	23.5	22.9
10	23.7	23.1
15	23.9	23.2
20	24	23.5
25	24.2	23.6
30	24.4	23.8
35	24.6	24
40	24.7	24.1
45	24.8	24.3
50	25	24.4

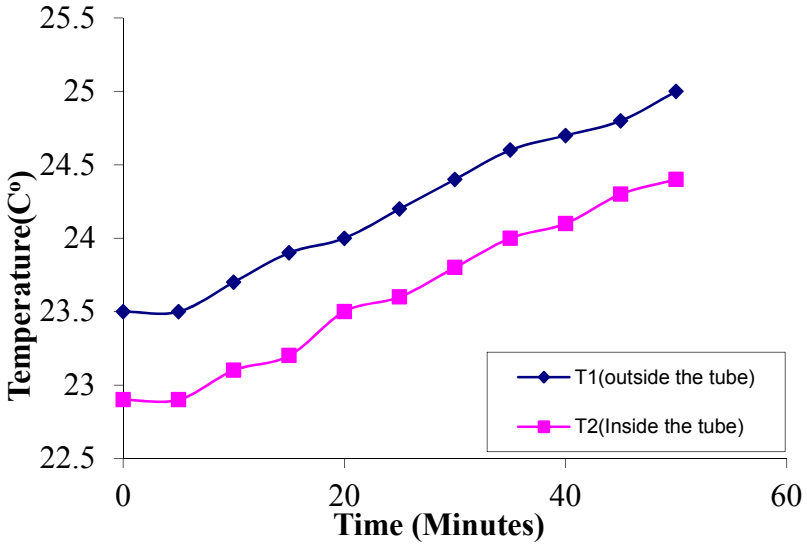

Figure 8.4 Temperature measurements over a 50 minute period of system operation.

8.2.3 CT image reconstruction and processing

To obtain reconstructed images of the volume scanned, the 2D projection images are first corrected to normalise the intensity response of each pixel and account for variation of the x-ray beam intensity at different positions on the detector. To make the corrections a flatfield correction (as described in chapter 7) has been applied to the image, which equalises the pixel intensity response and in turn improves the contrast detail of the image.

Figure 8.5 show the result of applying these corrections to a 2D projection image from the fat liver dataset. The image shows the plastic tube filled with water, fat and liver tissue and the layers of white paper.

Figure 8.5 Processed image using Matlab code, the image clearly shows the different tissues and white paper.

After these corrections have been made the set of 2D projection images at each angle are transformed to form a set of sinogram (Radon space) images for each detector row. These sinogram images are then supplied to the Octopus: 3D CT reconstruction software package, which uses a filtered back-projection algorithm to reconstruct a 3D volume of the scanned object from this dataset.

The parameters required (for Octopus) to perform the reconstruction procedure are provided in Table 8.8, other parameters describing the MARS-CT2 configuration for the scans are the source to object distance: 80 mm, and the distance between source and detector: 125 mm. The vertical centre where the central beam hits the detector was chosen to be at 125 pixels.

Reconstructed images from each of the three scans are shown in figures 8.6, 8.7 and Figure 8.8

Table 8.8 Image reconstruction parameters.

Parameter	Value
Pixel size	0.055 mm
COR	300.00 (for the GaAs, and CdTe detector); 223.27 (for the Si detector)
Offset angle	0.000000
BHC	not used
Noise filter level	not used
Vertical smoothing	not used
Back-projection filter	Ramp (Ram-Lak)
Tilt angle	0.000000
Base name	tiff_
Number of projections	303
Base name io	Io
Number of io	0
Base name di	Di
Number of di	0
Source detector distance	125.0
Vertical centre	20.0
Clip normalised data at	1.4
Direction of rotation	Counter clock wise
Voxel size	0.044 mm
Reconstruction quality	2
Local reconstruction	True
Last angle	360.0
Source object distance:	100.0
Cropping	Left=0, top=0, right=0, bottom=0
White spot filter level	-1.0

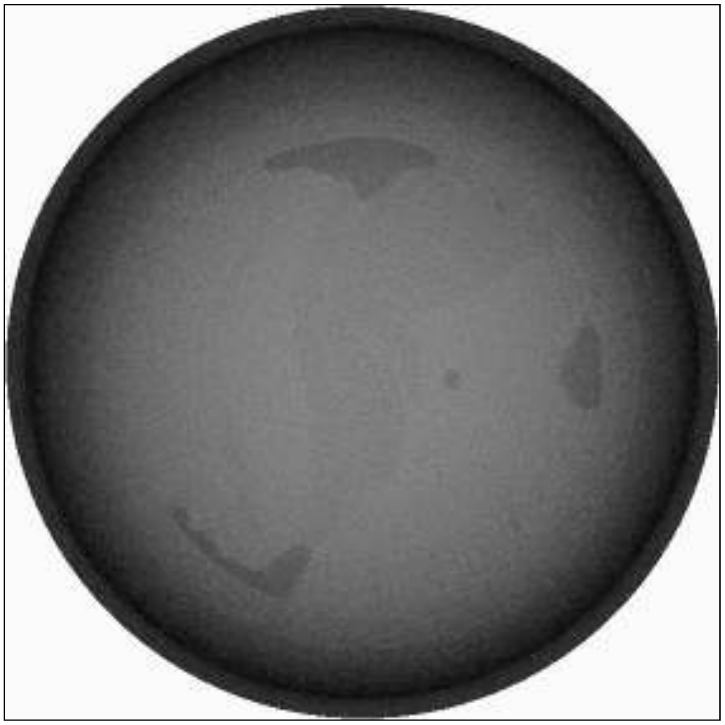

Figure 8.6 Reconstructed CT slices from the scan with the GaAs Medipix2 detector using a THL set for 14.45 keV. Reconstructions were performed using the Octopus software.

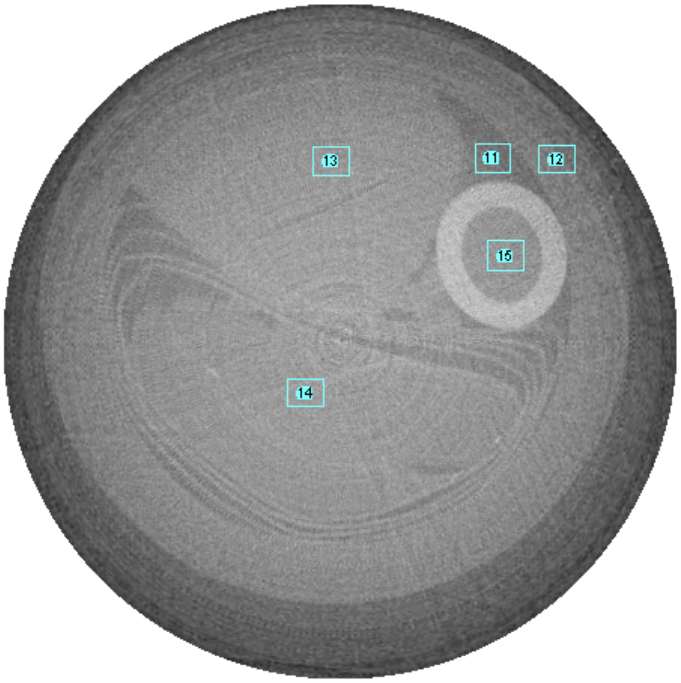

Figure 8.7 Image reconstructed from data acquired using the Si-Medipix2 detector showing selected regions of interest for (14) fat, (13) liver tissue, (11) air, and (15) water.

Figure 8.8 Image reconstructed from data acquired using the CdTe-Medipix2 detector.

8.2.3.1 Hounsfield unit calculation

The Hounsfield unit (also known as CT number) is commonly used for presentation of linear attenuation information in medical images and are used in this section to quantify the linear attenuation of fat and liver tissues measured in this chapter. A standard definition for the Hounsfield unit from (Brooks, 1977) is used to convert linear attenuation values from the reconstructed images to the Hounsfield scale by performing a simple calibration using air and water as follows:

$$CT = \frac{(\mu_x - \mu_{water})}{(\mu_{water} - \mu_{Air})} \times 1000HU \qquad 8.1$$

where μ_x is the effective attenuation coefficients for the voxel and μ_{water} and μ_{air} are effective attenuation coefficient for water and air respectively.

In this thesis the calibration of Hounsfield units in images is done for each energy range, so that the mean HU value for water is always zero and the mean HU value for air is always -1000.

8.2.3.2 Principle component analysis (PCA)

The principal component analysis (PCA) was derived in the beginning of the 20th century. But it wasn't until the 1990s that advances in personal computers made it possible to apply the method of PCA to the field of imaging and pattern recognition (Wold *et al.*, 1987). Since then it has been used in many fields ranging from voice recognition to medical imaging (Bones *et al.*, 2006); Butler, 2007). PCA is widely used in analysis of multi-spectral reflectance images obtained in the visible and near infrared spectral band. A good description of the application of PCA to multi-energy data acquired from different x-ray spectra is given in (Kalukin *et al.*, 2000).

In this chapter the PCA analysis is performed on acquisitions taken of the same object in different spectral bands. This is different to applications in pattern recognition where images of different objects are compared that vary in spatial configuration. The first dataset that we used for testing this technique was a series of radiographs of a fat and liver sample. They were obtained with a tungsten target x-ray tube with 2.5 mm Al filtration, operated at 75 kV. The detector was set to count photons in an energy bin of the fixed width of 3.5 keV. The lower energy threshold was shifted between 14.45 and 39.20 keV and 303 images have been acquired with a step size of approximately 0.75 keV and 150 μAs illumination.

Figure 8.9 shows two examples from the dataset. For the right image show the original image and for the left image, the energy bin was set between 13 keV and 16.1 keV, to the right image only photons with energy between 35.6 and 39.20 keV contributed. In the image from the high energy bin, the tube and the liver better visible. This is due to the fact that many of the high energy photons are transmitted through dense areas, while low energy photons are mostly absorbed, resulting in a hardening of the beam. In this case, detecting only high-energy photons leads to an improved contrast and better detail recognition.

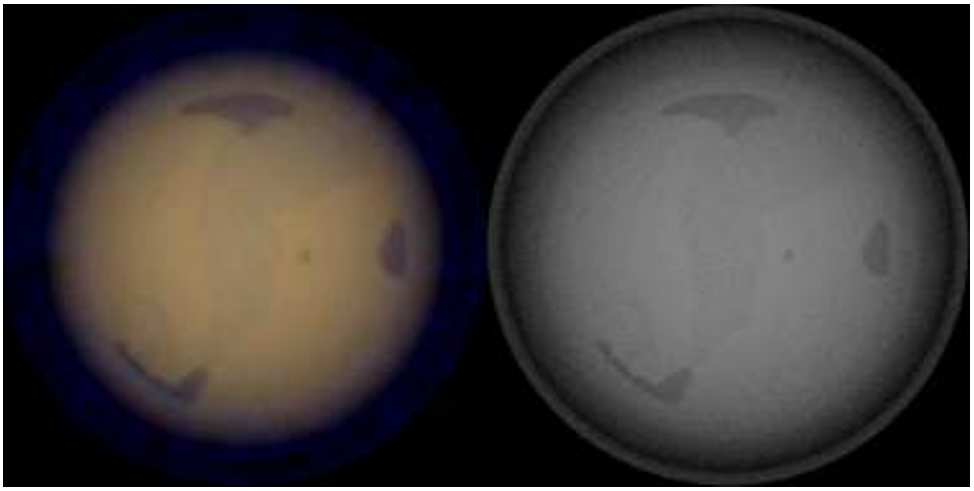

Figure 8.9 Material identification by applying PCA on the reconstructed images.

8.3 X-ray attenuation in fat and liver tissue

The reconstructed images of the fat and liver tissue samples were combined and averaged to represent a slice thickness of 1 mm. Regions in the averaged image corresponding to the fat sample, liver tissue, water, and air were selected and calibrated in HU using air and water as a references (Brooks, 1977) as in equation 8.1. This was repeated for each energy included in the scan and the data used to construct plots of x-ray attenuation (in HU) in the selected sample regions as a function of detector energy threshold. The attenuation of fat and liver in the image

acquired with the CdTe, GaAs, and Si Medipix2 detector are shown in Figures 8.10, 8.11 and 8.12 , respectively. The standard error of each selected sample region mean was calculated and is shown in Figure 8.13. The calculation of the attenuation and standard error was written using Matlab code shown in APPENDIX B.

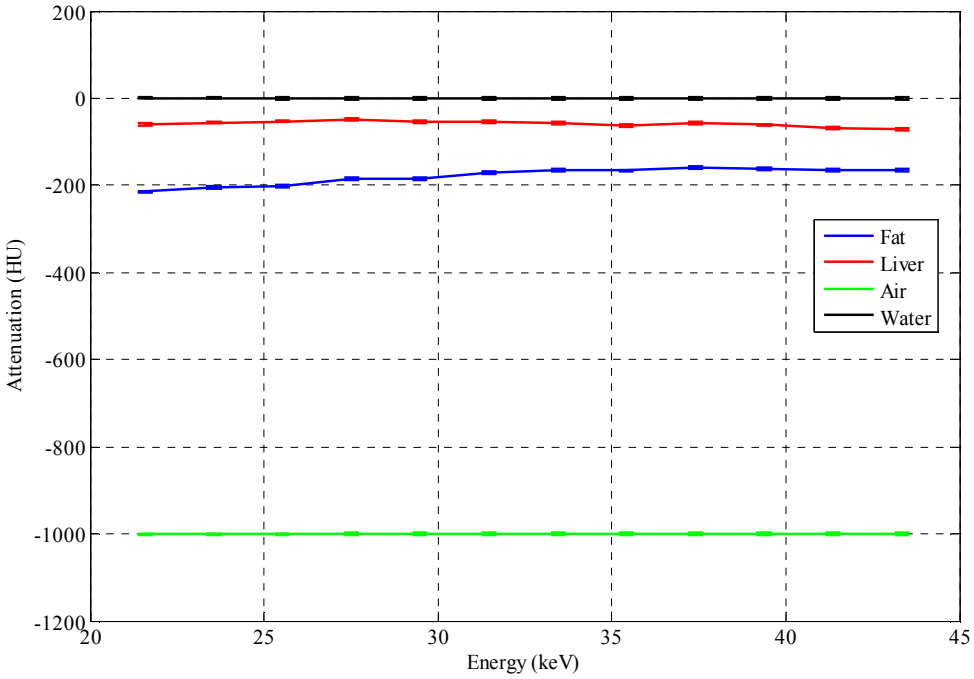

Figure 8.10 Attenuation of selected regions in a sheep fat and liver tissue sample acquired using a CdTe Medipix2 detector.

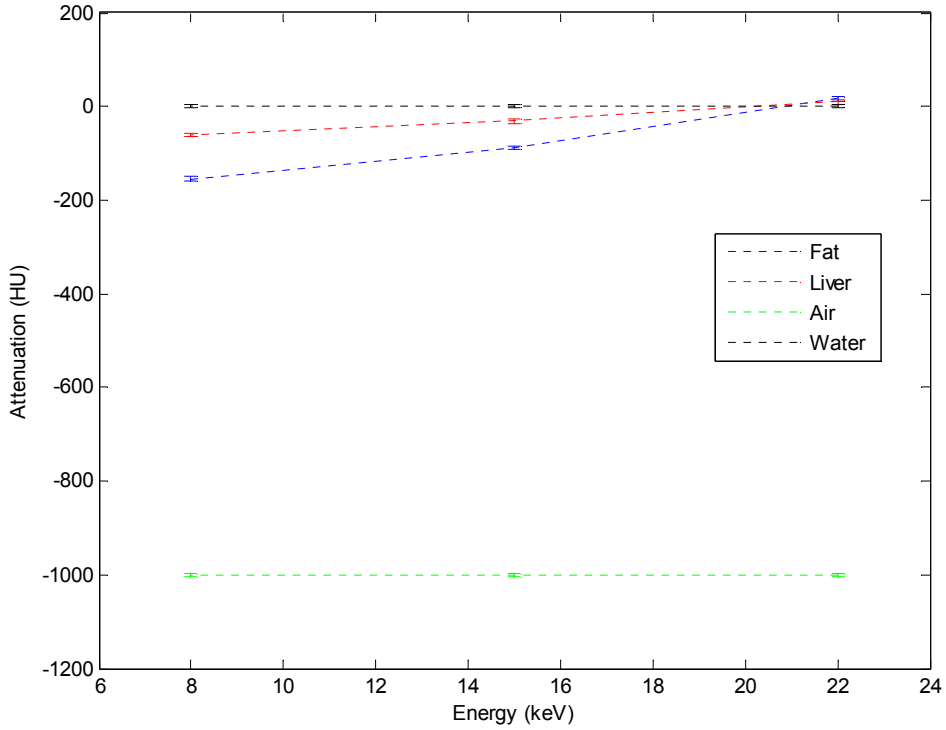

Figure 8.11 Attenuation of selected regions in a sheep fat and liver tissue sample acquired using a Si Medipix2 detector.

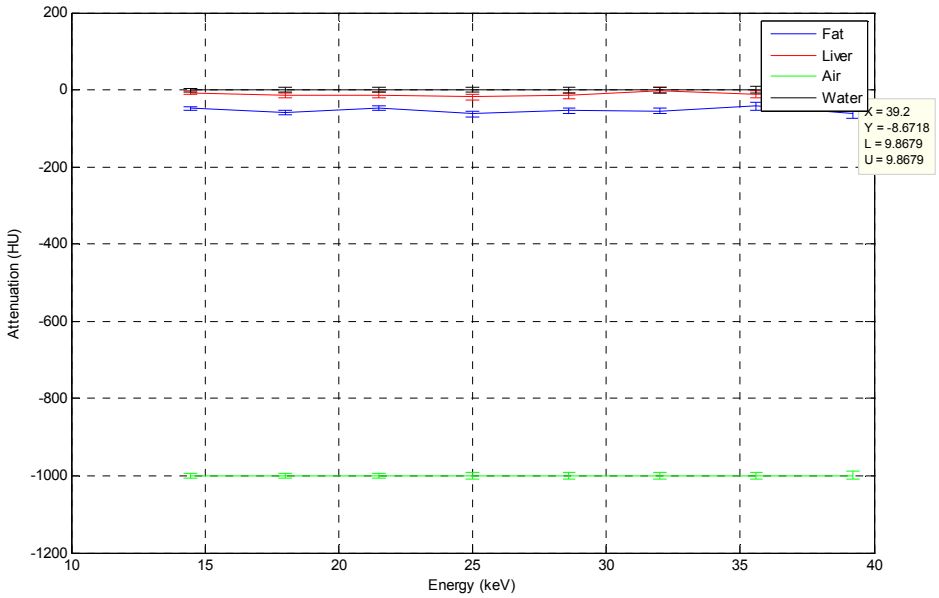

Figure 8.12 Attenuation of selected regions in a sheep fat and liver tissue sample acquired using a GaAs Medipix2 detector.

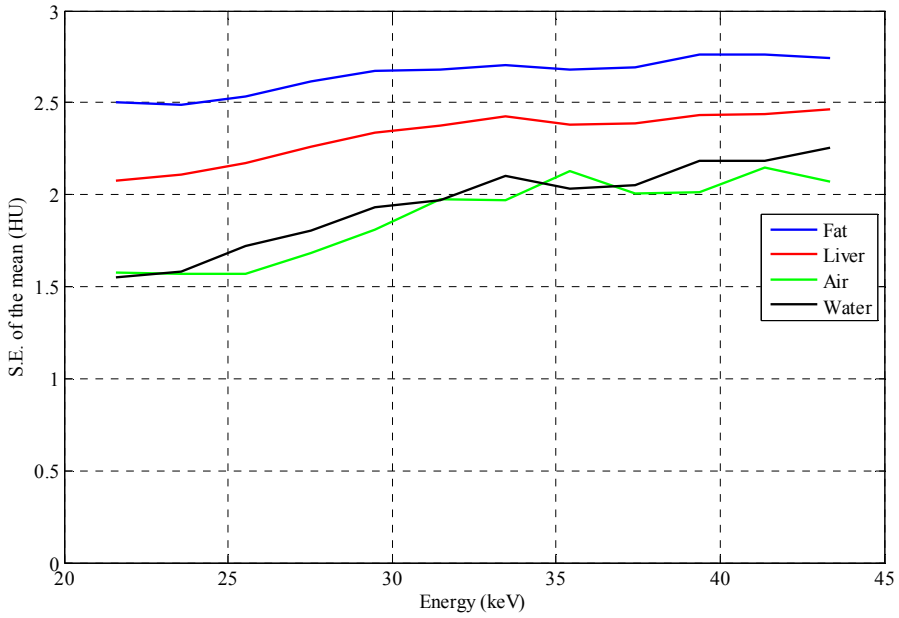

Figure 8.13 Standard error of the selected sample region mean attenuation for the image acquired with the CdTe Medipix2 detector.

8.4 Discussion and summary

The energy dependence of the attenuation (in Hounsfield units) for the selected regions in these experimental results are in general agreement with theoretical values and the experimental studies of (Ronaldson *et al.*, 2011). The calculated standard errors shown in Figure 8.12 demonstrate that precise measurements of attenuation can be made using the MARS-CT systems, which is supported by the previous measurements of attenuation presented in chapter 6.

However, it can be seen that the measured attenuation of the fat sample in figures 8.11 and 8.12 differs between the scans acquired with the CdTe and Si detectors. The reasons for this are not fully understood but could be due to factors such as, variations in the composition of the sample and the selection of the region of interest, and variations in attenuation across the images due to factors such as beam hardening and other reconstruction artefacts.

Taking into account the observations from chapter 4 that there is significant attenuation of low energy x-rays in water, combined with the inhomogeneity of the prepared sample, and the filtered back-projection reconstruction method, it seems likely that beam hardening effects may offer at least a partial explanation for the observed differences in attenuation of the fat and liver tissue in the different scans.

Chapter 9

9 Discussion and summary

Dual-energy CT has brought spectral x-ray imaging into clinical use (Lewin et al., 2003). Our goal was to apply Medipix, a spectroscopic photon-processing detector to biomedical applications. To do this, the 'Medipix All Resolution System scanner MARS-2 were used (Butler et al., 2008). Initial experiments with the MARS-2 setup have provided first results from a contrast agent study. Improvements to the MARS-2 setup have been made by developing improved image correction techniques. These are important, as they correct for some of the weaknesses of the MARS-1 equipment setup.

Monte Carlo simulations of an x-ray system for imaging a simple blood vessel phantom have been performed (using BEAMnrc) to identify the effect of the energy of the x-ray beam on the contrast to noise in images. In the first series of simulations, the spectrum of an x-ray beam after passing through iron was simulated under different conditions. The results from these simulations showed that although iron fluorescence x-rays can be detected this requires iron to be present in large quantities that are not normally found in the human body. In a subsequent simulation where water was included in the x-ray beam path, the transmitted x-ray beam had been strongly attenuated at the energies where the iron fluorescence occurs. This prevented detection of the iron fluorescence x-rays and suggests there is a practical lower energy limit for clinical spectral imaging applications.

The second series of simulations was performed to identify combinations of scan parameters such as x-ray tube voltage, imaging geometry, and detector energy thresholds that can be used to obtain high contrast images in applications where iodine contrasts agents are used. The optimum x-ray tube energy was found to be 50 kVp (see section 4.3.5), and at this x-ray tube energy, the minimum concentration of iodine was found to be 6 to 8 mg/ml (see section 4.3.6).

These simulations provide a useful guide for determining suitable system parameters for acquiring images, but in situations where parameters may need to be known to a higher accuracy (such as in human imaging), a more detailed simulation model is required. The iodine used in this simulation is considered to be metal, but in the real situations the iodine is diluted with other chemicals. Consequently, the simulation medium should be representative of the chemical compounds and actual concentrations used.

In this work a slab of air represented the detector. Future work requires the use of the geometry that represents the Medipix detector that is used in the experimental setup. This includes accounting for the geometry of the detector (primarily thickness and position), and the differences in x-ray attenuation properties of the detector at different energies.

The project takes the advantage of using the Medipix2 detector, which is intended for pre-clinical medical imaging use. The Medipix-2 detector, was found to be reliable and easy to use, and can acquire images with useful soft tissue contrast characteristics. Image artefacts caused by inhomogeneity in the semiconductor sensor layer and abnormally functioning pixels have been reduced by making post-acquisition corrections to images.

An application to perform (dual energy) image subtraction was developed. Following initial tests of the software x-ray images of a blood-vessel phantom were acquired and used to investigate the effect of x-ray beam energy on image contrast. This work is a first step towards applying the spectroscopic capabilities of the new MedipixRX detectors (which are not yet available) to perform image enhancement by using image data acquired over different energy ranges above and below the iodine k-edge that are acquired in a single exposure.

It can be inferred (although somewhat speculatively) from the experimental measurements made using the blood-vessel phantom in Chapter 5, and the simulated measurements of x-ray transmission spectra for different measured x-ray beam energies (in Chapter 4), that proposed image enhancement techniques using image data acquired over different energy ranges above and below the iodine k-edge in a single exposure, will work in practice. Provided, that technical constraints such as the detector energy resolution are satisfactory for a given application.

Chapters 6 and 8 have investigated the use of Medipix2 detectors in the MARS-CT scanner to quantify the fat content of liver tissue. The calculated standard error of attenuation in selected regions of images is less than 4 HU corresponding to a standard uncertainty of ~ 10 HU. Since at low energies the attenuation of fat is -200 HU and water (by definition) is 0 HU, the calculated standard uncertainty suggests it will be possible to reliably differentiate between fat and liver tissue. However, large sources of error not accounted for by the calculated standard error were observed to be present.

The sensitivity of several current techniques for quantifying fat content in liver reviewed in section 1.5 is relatively poor.

I was able to develop a protocol for producing linear attenuation curves from reconstructed images and projection images after processing. It is necessary to adapt the existing reconstruction programs for spectral information. The liver and fat data showed that although these materials display large differences in linear attenuation, over the energy range I measured the attenuation curves are not spectroscopically different within error.

REFERENCES

AAMIR, R., LANSLEY, S. P., ZAINON, R., FIEDERLE, M., FAULER, A., GREIFFENBERG, D., BUTLER, P. H. & BUTLER, A. P. H. 2011. Pixel sensitivity variations in a CdTe-Medipix2 detector using poly-energetic x-rays. *Journal of Instrumentation,* 6**,** C01059.

ALESSANDRA, T., ANGELO, T., BALDAZZI, G., DANTE, B., MIRCO, G., RAMELLO, L. & MAURO, G. Novel x-ray source for dual-energy subtraction angiography. *In:* LARRY, E. A. & MARTIN, J. Y., eds., 2002. SPIE, 311-319.

ALVAREZ, R. E. & MACOVSKI, A. 1976. Energy-selective reconstructions in X-ray computerised tomography. *Physics in Medicine and Biology,* 21**,** 733.

AMBROSE, J. & HOUNSFIELD, G. 1973. Computerized transverse axial tomography. *Br J Radiol,* 46**,** 148-9.

ANDERSON, N., BUTLER, A., SCOTT, N., COOK, N., BUTZER, J., SCHLEICH, N., FIRSCHING, M., GRASSET, R., DE RUITER, N., CAMPBELL, M. & BUTLER, P. 2010. Spectroscopic (Multi-Energy) CT Distinguishes Iodine and Barium Contrast Material in MICE. *European Radiology***,** 2126-2134.

ARCHER, B. R., THORNBY, J. I., BUSHONG, S. C. & HARRIS COUNTY HOSPITAL DISTRICT, R. S. O. H. T. X. 1983. Diagnostic X-ray shielding design based on an empirical model of photon attenuation. *Health Phys.,* 44:5**,** 507-517.

BAE, K. T. 2010. Intravenous Contrast Medium Administration and Scan Timing at CT: Considerations and Approaches1. *Radiology,* 256**,** 32-61.

BALDAZZI, G., BOLLINI, D., CELESTI, E., GAMBACCINI, M., GOMBIA, M., LABANTI, C., TAIBI, A. & TUFFANELLI, A. 2001a. First results with a novel X-ray source for dual energy angiography. *Nuclear Science Symposium Conference Record.* Italy: IEEE.

BALDAZZI, G., BOLLINI, D., CELESTI, E., GAMBACCINI, M., GOMBIA, M., LABANTI, C., TAIBI, A., TUFFANELLI, A. & DIPT. DI FISICA BOLOGNA UNIV. ITALY 2001b. First results with a novel X-ray source for dual energy angiography. *Nuclear Science Symposium Conference Record, 2001 IEEE,* 3**,** 1615-1619.

BATES, R. H. T. & PETERS, T. M. 1971. Towards improvements in tomography. *New Zealand Journal of Science,* 14**,** 883-896.

BELL, S. 2011. A virtual CT system. *Special topic report.* New Zealand: University of Canterbury.

BERG, K. B., CARR, J. M., CLARK, M. J., COOK, N. J., ANDERSON, N. G., SCOTT, N. J., BUTLER, A. P., BUTLER, P. H. & BUTLER, A. P. 2009. Pilot Study to Confirm that Fat and Liver can be Distinguished by Spectroscopic Tissue Response on a Medipix-All-Resolution System-CT (MARS-CT). *AIP Conference Proceedings,* 1151**,** 106-109.

BONES, P. J., BUTLER, A. P. H. & HURRELL, M. Enhancement of chest radiographs using eigenimage processing. *In:* BONES, P. J., FIDDY, M. A. & MILLANE, R. P., eds., 2006 San Diego, CA, USA. SPIE, 63160C-12.

BORJESSON, J., ISAKSSON, M. & MATTSSON, S. 2003. X-ray fluorescence analysis in medical sciences: a review. *Acta Diabetologica,* 40**,** S39-S44.

BORNEFALK, H., LEWIN, J. M., DANIELSSON, M. & LUNDQVIST, M. 2006. Single-shot dual-energy subtraction mammography with electronic spectrum splitting: Feasibility. *European Journal of Radiology,* 60**,** 275-278.

BROOKS, R. A. 1977. A quantitative theory of the Hounsfield unit and its application to dual energy scanning. *J Comput Assist Tomogr,* 1**,** 487-93.

BUSHBERG, J. T. 1998. The AAPM/RSNA physics tutorial for residents. X-ray interactions. *Radiographics,* 18**,** 457-468.

BUTLER, A. P. H., ANDERSON, N. G., TIPPLES, R., COOK, N., WATTS, R., MEYER, J., BELL, A. J., MELZER, T. R. & BUTLER, P. H. 2008. Bio-medical X-ray imaging with spectroscopic pixel detectors. *Nuclear Inst. and Methods in Physics Research, A,* 591**,** 141-146.

BUTZER, J. S., BUTLER, A. P. H., COOK, N. J., BUTLER, P. H., ROSS, F., SCHLEICH, N., SELKIRK, J., WATTS, R., MEYER, J., SCOTT, N., BONES, P. J., VAN LEEUWEN, D., HEMMINGSEN, S., MELZER, T. P., ANDERSON, N. & TEAM, M.-C. 2008. MARS: a 3D Spectroscopic X-Ray Imaging Device Based on Medipix. *IEEE Nuclear Science Symposium and Medical Imaging Conference.* Dresden, Germany: University of Canterbury. Electrical and Computer Engineering and Physics and Astronomy.

CAMPBELL, M., HEIJNE, E. H. M., MEDDELER, G., PERNIGOTTI, E. & SNOEYS, W. 1998. A readout chip for a 64 x 64 pixel matrix with 15-bit single photon counting. *Journal Name: IEEE Transactions on Nuclear Science; Journal Volume: 45; Journal Issue: 3Pt1; Conference: Institute of Electrical and Electronic Engineers (IEEE) nuclear science symposium and medical imaging conference, Albuquerque, NM (United States), 11-13*

Nov 1997; Other Information: PBD: Jun 1998, Medium: X; Size: pp. 751-753.

CARROLL, B. W. & OSTLIE, D. A. 2007. *An Introduction to Modern Astrophysics*, Pearson Addison-Wesley.

CERN. 1991. *Medipix home page* [Online]. Geneva: CERN. Available: http://medipix.web.cern.ch/MEDIPIX/ [Accessed 06 November 2008].

CHEZMAR, J. L., NELSON, R. C., MALKO, J. A. & BERNARDINO, M. E. 1990. Hepatic iron overload: diagnosis and quantification by noninvasive imaging. *Gastrointest Radiol,* 15**,** 27-31.

DE KEMP, R. A., EPSTEIN, F. H., CATANA, C., TSUI, B. M. W. & RITMAN, E. L. 2010. Small-Animal Molecular Imaging Methods. *Journal of Nuclear Medicine,* 51**,** 18S-32S.

FANTI, V., MARZEDDU, R. & RANDACCIO, P. 2003. MPRS: Medipix parallel readout system for angiography digital imaging. *Ieee Transactions on Nuclear Science,* 50**,** 1664-1666.

FARRELL, G. C. & LARTER, C. Z. 2006. *Nonalcoholic fatty liver disease : From steatosis to cirrhosis,* Hoboken, NJ, ETATS-UNIS, Wiley.

FORNARO, J., LESCHKA, S., HIBBELN, D., BUTLER, A., ANDERSON, N., PACHE, G., SCHEFFEL, H., WILDERMUTH, S., ALKADHI, H. & STOLZMANN, P. 2011. Dual- and multi-energy CT: approach to functional imaging. *Insights Imaging,* 2**,** 149-159.

GIERSCH, J. 2005. Medical quantum X-ray imaging with 2D detectors. *Nuclear Instruments and Methods in Physics Research Section A: Accelerators, Spectrometers, Detectors and Associated Equipment,* 551**,** 125-138.

GIERSCH, J., NIEDERLOHNER, D. & ANTON, G. 2004. The influence of energy weighting on X-ray imaging quality. *Nuclear Instruments and Methods in Physics Research Section A: Accelerators, Spectrometers, Detectors and Associated Equipment,* 531**,** 68-74.

GROBERG T, S. S., ALMEN T, GOLMAN K, MATTSSON S 1983. Noninvasive estimation of kidney function by X-ray fluorescence analysis. *Invest Radiology,* 18**,** 445-452.

HASEGAWA, B. 1987. *Physics of Medical X-Ray Imaging* Medical Physics Pub Corp.

HOLLEMAN, A. F. & WIBERG, E. 2001. *Inorganic Chemistry* [Online]. San Diego, CA Academic Press.

HOLY, T., JAKUBEK, J., POSPISIL, S., UHER, J., VAVRIK, D. & VYKYDAL, Z. 2006. Data acquisition and processing software package for Medipix2.

Nuclear Instruments and Methods in Physics Research Section A: Accelerators, Spectrometers, Detectors and Associated Equipment, 563**,** 254-258.

HOUNSFIELD, G. N. 1973. Computerised transverse axial scanning. (tomography): Part 1. *British Journal of Radiology,* 46**,** 1016-22.

HOUNSFIELD, G. N. 1980. Nobel Award address. Computed medical imaging. *Med Phys,* 7**,** 283-90.

HUBBELL, J. H. 1994. Tables of X-Ray Mass Attenuation Coefficients and Mass Energy-Absorption Coefficients from 1 keV to 20 MeV for Elements Z = 1 to 92 and 48 Additional Substances of Dosimetric Interest. *Radiation and Biomolecular Physics Division, PML, NIST,* 5437**,** 1907-1993.

ICRU. 1984. Stopping powers for electrons and positrons. *In:* 37, R. (ed.). Washington D.C.: ICRU.

KALUKIN, A. R., VAN GEET, M. & SWENNEN, R. 2000. Principal components analysis of multienergy X-ray computed tomography of mineral samples *IEEE Transactions on Nuclear Science,* 47**,** 1729 - 1736.

KAMEL, I. R., KRUSKAL, J. B., POMFRET, E. A., KEOGAN, M. T., WARMBRAND, G. & RAPTOPOULOS, V. 2001. Impact of Multidetector CT on Donor Selection and Surgical Planning Before Living Adult Right Lobe Liver Transplantation. *American Journal of Roentgenology,* 176**,** 193-200.

KARCAALTINCABA, M. & AKHAN, O. 2007. Imaging of hepatic steatosis and fatty sparing. *Eur J Radiol,* 61**,** 33-43.

KAWRAKOW, I. & ROGERS, D. W. O. 2000. The EGSnrc Code System: Monte Carlo simulation of electron and photon transport. *In:* PIRS-701, R. (ed.). Ottawa Canada,: National Research Council of Canada.

KAWRAKOW, I. & ROGERS, D. W. O. 2001. The EGSnrc System a status report in Advanced Monte Carlo for Radiation Physics Particle Transport Simulation and Applications. *Proc. of.* Springer, Berlin.

KENNETH, R. H., JACEK, D., DARYL, P. N., LASZLO, M., BALAZS, N., ANANT, G., ZHOU, W., STEPHEN, R. & DANIEL, R. B. 2003. Vessel size measurements in angiograms: Manual measurements. *Medical Physics,* 30**,** 681-688.

KOBAYASHI, S. 1998. Advantage of appropriate K-edge filters for one-shot dual-energy subtraction sialography. *Dentomaxillofac Radiol,* 27**,** 151-162.

LALL, C. G., AISEN, A. M., BANSAL, N. & SANDRASEGARAN, K. 2008. Nonalcoholic Fatty liver disease. *AJR Am J Roentgenol,* 190**,** 993-1002.

LEWIN, J. M., ISAACS, P. K., VANCE, V. & LARKE, F. J. 2003. Dual-Energy Contrast-enhanced Digital Subtraction Mammography: Feasibility. *Radiology,* 229**,** 261-268.

LIMOUSIN, O. 2003. New trends in CdTe and CdZnTe detectors for X- and gamma-ray applications. *Nuclear Instruments and Methods in Physics Research Section A: Accelerators, Spectrometers, Detectors and Associated Equipment,* 504**,** 24-37.

LLOPART, X., CAMPBELL, M., SAN SEGUNDO, D., PERNIGOTTI, E. & DINAPOLI, R. Medipix2, a 64k pixel read out chip with 55 μm square elements working in single photon counting mode. Nuclear Science Symposium Conference Record, 2001 IEEE, 4-10 Nov. 2001 2001. 1484-1488

MARSHALL, W., HALL, E., DOOST-HOSEINI, A., ALVAREZ, R., MACOVSKI, A. & CASSEL, D. 1984. An Implementation of Dual Energy CT Scanning. *Journal of Computer Assisted Tomography,* 8**,** 745-749.

MARSHALL, W. H., JR., ALVAREZ, R. E. & MACOVSKI, A. 1981. Initial results with prereconstruction dual-energy computed tomography (PREDECT). *Radiology,* 140**,** 421-30.

MIA, S., MARTIN, J. Y., AILI, K. B., DAN, R., SERGE, M., ANDREAS, R. & FANNY, J. 2002. Development of contrast digital mammography. *Medical Physics,* 29**,** 2419-2426.

MIKULEC, B. 2000. *Single Photon Detection with Semiconductor Pixel Arrays for Medical Imaging Applications.* PhD Thesis, University of Vienna.

MIKULEC, B. 2003. Development of segmented semiconductor arrays for quantum imaging. *Nuclear Instruments and Methods in Physics Research Section A: Accelerators, Spectrometers, Detectors and Associated Equipment,* 510**,** 1-23.

MORANNE O, F.-W., SERGE, WILLOTEAUX S, F.-P., DOMINIQUE, PAGNIEZ D, F.-D., PHILIPPE, DEQUIEDT P, F.-B., ERIC & BOULANGER, E. 2006. Effect of iodinated contrast agents on residual renal function in PD patients.

NELSON, W. R., HIRAYAMA, H. & ROGERS, D. W. O. 1985. The EGS4 Code System. . *In:* SLAC-265 (ed.). Stanford California,: Stanford Linear Accelerator Center.

NOLTE-ERNSTING, C., ADAM, G., BUCKER, A., BERGES, S., BJORNERUD, A. & GUNTHER, R. 1998. Abdominal MR angiography performed using blood pool contrast agents: comparison of a new

superparamagnetic iron oxide nanoparticle and a linear gadolinium polymer. *AJR Am J Roentgenol,* 171**,** 107-113.

NOLTE-ERNSTING C, A. G., BUCKER A, BERGES S, BJORNERUD A, GUNTHER RW 1998. Abdominal MR angiography performed using blood pool contrast agents: comparison of a new superparamagnetic iron oxide nanoparticle and a linear gadolinium polymer. *AJR Am J Roentgenol,* 171**,** 107-113.

PADEZNIK, G. J., ARCON, I., DE PANFILIS, S. & KODRE, A. 2008. X-ray absorption coefficient of iodine in the K edge region. *Journal of Physics B: Atomic, Molecular and Optical Physics,* 41**,** 025003.

PARRA, L. C. 2003. BME I5000: Biomedical Imaging. US: City College of New York.

PFEIFFER, K. F. G., GIERSCH, J., ANTON, G., BATZ, L. & HOHEISEL, M. 2003. Large-scale images taken with the Medipix1 chip. *Nuclear Instruments and Methods in Physics Research Section A: Accelerators, Spectrometers, Detectors and Associated Equipment,* 509**,** 340-345.

PLLANA & SABRI. 2003. *History of Monte Carlo method.* [Online]. Available: http://www.geocities.com/CollegePark/Quad/2435/index.html, [Accessed 15 September 2008 2008].

PRINO, F., CEBALLOS, C., CABAL, A., SARNELLI, A., GAMBACCINI, M. & RAMELLO, L. 2008. Effect of x-ray energy dispersion in digital subtraction imaging at the iodine K-edge--a Monte Carlo study. *Medical Physics,* 35**,** 13-24.

PTY.LTD. 2000-2008. *Excitation model* [Online]. United State: The A to Z of Materials and AZojomo. Available: http://www.azom.com/details.asp?ArticleID=3928 [Accessed 2nd July 2008].

QUARATI, F., O'SHEA, V. & SMITH, K. M. 2005. Image quality of Medipix2 assemblies with silicon detectors of two different thicknesses. *Nuclear Instruments and Methods in Physics Research Section A: Accelerators, Spectrometers, Detectors and Associated Equipment,* 546**,** 42-45.

RAPTOPOULOS, V., KARELLAS, A., BERNSTEIN, J., REALE, F. R., CONSTANTINOU, C. & ZAWACKI, J. K. 1991. Value of dual-energy CT in differentiating focal fatty infiltration of the liver from low-density masses. *AJR Am J Roentgenol,* 157**,** 721-5.

ROENTGEN, W. 1895. physikalisch-medizinisechen geseeschaft zu wurzburg. *uber eine neue art von strahlen***,** 9:132.

RONALDSON, J., ZAINON, R., SEDAYO, A., SCOTT, N., BUTLER, A., BUTLER, P. & ANDERSON, N. 2011. Towards Quantifying the

Composition of Soft-tissues by Spectral CT Imaging with Medipix3. *Radiological Society of North America.* Chicago, USA: Scientific Assembly and Annual Meeting.

SAN SEGUNDO BELLO, D., VAN BEUZEKOM, M., JANSWEIJER, P., VERKOOIJEN, H. & VISSCHERS, J. 2003. An interface board for the control and data acquisition of the Medipix2 chip. *Nuclear Instruments and Methods in Physics Research Section A: Accelerators, Spectrometers, Detectors and Associated Equipment,* 509**,** 164-170.

SANTOS, A. C., SCH., M. S. P. U. & FURUIE, S. S. 2001. Estimation of coronary blood flow by contrast propagation using X-ray cineangiographic images *IEEE xplore.*

SCHENA, G., DREOSSI, D., MONTANARI, F., OLIVO, A. & PANI, S. 2003. Multiple-energy X-ray radiography and digital subtraction for a particle-composition sensor. *Minerals Engineering,* 16**,** 609-617.

SKUCASM, J. 1989. Radiographic Contrast Agents. *In:* 2ND (ed.) *ASIN: 0834200066.* Rockville Maryland,: Aspen.

STANEV, T. 2010. *High Energy Cosmic Rays,* UK, Jointly published with Praxis Publishing Ltd.

STANTON, A. 1896. Wilhelm Conrad Röntgen On a New Kind of Rays: translation of a paper read before the Würzburg Physical and Medical Society. *Nature,* 55**,** 274-276.

STRUTT, J. W. 1899. On the transmission of light through an atmosphere containing small particles in suspension, and on the origin of the blue of the sky. *Philosophical Magazine,* 47**,** 375-394.

ULLMAN, G., SANDBORG, M., DANCE, D. R., YAFFE, M. & CARLSSON, G. A. 2005. A search for optimal x-ray spectra in iodine contrast media mammography. *Physics in Medicine and Biology,* 50**,** 3143-3152.

WANG, X., MEIER, D., TAGUCHI, K., WAGENAAR, D. J., PATT, B. E. & FREY, E. C. 2011. Material separation in x-ray CT with energy resolved photon-counting detectors. *Med Phys,* 38**,** 1534-46.

WOLD, S., ESBENSEN, K. & GELADI, P. 1987. Principal component analysis. *Chemometrics and Intelligent Laboratory Systems,* 2**,** 37-52.

WRIGHT, V. A., DAVIDSON, W. D., MELONE, J. J., O'SHEA, V., SMITH, K. M., DONOHUE, L., LEA, L., ROBB, K., NENONEN, S. & SIPILA, H. 2005. Three-dimensional medipix - A new generation of X-ray detectors. *IEEE Transactions on Nuclear Science,* 52**,** 1873-1876.

ZAINON, R., COOK, N. J., BUTLER, A. P., GIESEG, S., ANDERSON, N., BUCKENHAM, T., SHELKOV, G., TLUSTOS, L. J., ROAKE, A. &

BUTLER, P. H. 2010. High resolution multi-energy CT imaging of atherosclerotic plaque. *New Zealand Medical Journal,* 123**,** 97.

ZWERGER, A., FAULER, A., FIEDERLE, M. & JAKOBS, K. 2007. Medipix2: Processing and measurements of GaAs pixel detectors. *Nuclear Instruments and Methods in Physics Research Section A: Accelerators, Spectrometers, Detectors and Associated Equipment,* 576**,** 23-26.

APPENDIX A: Matlab code for image subtraction

```
clear
 % read the images in
 [filename, pathname] = uigetfile({'*.txt';'*.jpg';'*.dcm';...
 '*.tif';'*.*'},'File Selector');
    if isequal(filename,0)
      disp('User selected Cancel')
    else
      % disp(['User selected',...
      % fullfile(pathname, filename)])
    end
    size(filename);
    [R C]=size(filename); W = filename(1,C);
if isequal(W,'t')
         S1=load(filename);
         plot(S1(:,1),S1(:,2));
else
         if isequal(W,'g')
            S1=imread(filename); I=S1;
         elseif isequal(W,'f')
            S1=imread(filename); I=S1;
         else
            S1=dicomread(filename);I=S1;
         end
LEN = filename(1,C-2:C);

      ButtonName=questdlg('Load the Second file','Second Image
Type', ...
                          LEN, LEN);
              if isequal (LEN,'jpg')
         [filename, pathname] = uigetfile({'*.jpg'},'File
Selector');
          if isequal(filename,0)
            disp('User selected Cancel')
          else
          % disp(['User selected',...
          % fullfile(pathname, filename)])
          end
        S2=imread(filename);I2=S2;
      elseif  isequal(LEN,'tif')
       [filename, pathname] = uigetfile({'*.tif'},'File
Selector');
         if isequal(filename,0)
            disp('User selected Cancel')
         else
            % disp(['User selected',...
            % fullfile(pathname, filename)])
         end
       S2=imread(filename); I2=S2;
     else isequal(LEN,'dcm')
      [filename, pathname] = uigetfile({'*.dcm'},'File Selector');
       if isequal(filename,0)
         disp('User selected Cancel')
       else
         % disp(['User selected',...
         % fullfile(pathname, filename)])
       end
```

```
    S2=dicomread(filename); I2=S2;
  end % if load ipg, tif or decom type files
 % convert to single channel, range 0->1H=double(I(:,:,1))/255;
 H=double(I(:,:,1))/255;
 H2=double(I2(:,:,1))/255;
  iptsetpref('ImshowAxesVisible','on')
  %generate x,y data for H
 x=1:size(H,2);
 y=1:size(H,1);
  %load the control points
 cpselect(H,H2);
 %%%warndlg('please select the control points and hit OK.');
 input('please select the control points and hit enter. ');
 %this return input_points and base_points
 %input_points
 %base_points
 %%%
 T=cp2tform(input_points,base_points,'linear conformal');
  %do transform
 Hfixed=imtransform(H,T,'udata',[1 size(H,2)],'vdata',[1
size(H,1)],'xdata',[1 size(H,2)],'ydata',[1 size(H,1)]);
 figure, imshow(Hfixed,[0, 1])
 end % ends the first if condition of line 15
figure, imshow(H2,[0, 1])
X = Hfixed - H2 ;
figure, imshow(X,[0, 1])
%X = 0.5 * (Hfixed - H2) ;
%figure, imshow(X,[])
```

APPENDIX B: Matlab code for image processing

```
home
clear all
delete L.mat J.mat
load('parameters.mat');
load('scanner.mat');
load('flatfield.mat');
 % Change the directory from 'D:\MARS\trunk' &
'D:/MARS_data_archive/'
% current directory
scanner.paths.base = pwd;
scanner.paths.data = pwd;
%============================================================
 %% Set all the scan constants
datapath      =   fullfile(scanner.paths.data,parameters.name);
windows       =   size(parameters.THL,1); % number of energy
windows
stops         =   parameters.stops;
projections   =   parameters.projections;
sensor_pixels =
parameters.scanner.pixelman.mpxInfo.sensor_pixels;
time          =   parameters.time;

%% Files...
frame_dir        = 'frames';
frame_file       = 'frame_%03d_%1d.mat';
projection_dir   = '1_projections';
projection_file  = 'projection_%03d.mat';

%% Ensure directories exists
warning off MATLAB:MKDIR:DirectoryExists
    mkdir(datapath);
    mkdir(datapath,projection_dir);
warning on MATLAB:MKDIR:DirectoryExists


%% Reorganise the projection images
for i = 1:projections
    I = zeros(stops* sensor_pixels , sensor_pixels , windows); %
allocate some memory

outfile=fullfile(datapath,projection_dir,sprintf(projection_file,i
));
    fprintf('Producing file: %s   ',sprintf(projection_file,i));

    if exist(outfile,'file')
        fprintf(' ...already processed\n');
        continue;
    end
       for j = 1:stops

        P =
load(fullfile(datapath,frame_dir,sprintf(frame_file,i,j)));
        columns = 1:sensor_pixels;
        rows    = (1:sensor_pixels) + ((stops-j)*(sensor_pixels));
```

```
        % Correcting for aqquisition time
        for k=1:windows
        P.I(:,:,k)=P.I(:,:,k)/time(k);
        end
               I(rows,columns,:) = P.I(:,:,1:windows);
    end
        rot = P.rot;
    save(outfile,'I','rot');
    fprintf('   ...done\n')
end
 success = 1; % return 1 if it works

%% Start ApplyFF
%% Files locations and names
flatfield_file  = fullfile(datapath,'flatfield.mat');
projections_dir = '1_projections';  %input dir
projection_file = 'projection_%03d.mat';
FF_dir   = '2_post_FF'; %output dir
FF_file  = 'post_FF_%03d.mat';

%% Ensure directories exists
warning off MATLAB:MKDIR:DirectoryExists
mkdir(datapath);
mkdir(datapath,FF_dir);
warning on MATLAB:MKDIR:DirectoryExists

%% Load the flatfield
% Load flatfield
% % % S = load(flatfield_file);
% % % F = S.F;

%%normalise the FF
for i=1:size(F,3)
    q=F(:,:,i); q=q(:); %turn it into a vector
    m=sum(q) / sum(q~=0); %sum up all non-zero elements
    F(:,:,i) = F(:,:,i) / m;
end

%% Process each projection one at a time
%
%   1) apply flat field
%   2) save to FF_dir

for i = 1:1 % projections % loop over all projections
    infile  =
fullfile(datapath,projections_dir,sprintf(projection_file,i)); %
where to load for each projection
    outfile = fullfile(datapath,FF_dir,sprintf(FF_file,i));    %
Where to save for each proejction
    fprintf('Producing file: %s   ',sprintf(FF_file,i));
        if exist(outfile,'file') % else it will say already
processed if file exists
      fprintf(' ...already processed\n'); % if the file already
exists
    else
  %?????????????????????????????????????????????????????????
```

```
    end
 %%==============================
            % New code
         S = load(infile); % load structure with I the projeciton
in it and some other vars
        I=S.I; rot=S.rot;
                          My_F=I;
% % %             My_F=My_F*0.035; % Get the counts
 for energy = 1:size(F,3);
       My_F(:,:,energy)=My_F(:,:,energy).*
parameters.time(energy,:);
end

            %+++++++++++++++++ Number of Steps

%if size(F,1) == 768         % Three Steps Flatfiled and
Projections (Images)
            % Find the median of the detector through hundred
frames.
    My_F_Step_1 = My_F(1:256,:,:); % The FIRST 256 x 256 x energy
levels
                         q=median(median(My_F_Step_1));
            p=q(:);
            M_D=median(p);
             % Get the median for each pixel through hundred
frames and finf the
            % correction map
                 M_P=median(My_F_Step_1,3);
                F_CM = M_P / M_D;
             % Do the flat field
             for j=1:size(My_F_Step_1,3);
                F_N(:,:,j) = My_F_Step_1(:,:,j)./F_CM(:,:,:);
            end
             J1 = F_N;
    My_F_Step_2 = My_F(257:512,:,:); % The SECOND 256 x 256 x
energy levels
                          q=median(median(My_F_Step_2));
            p=q(:);
            M_D=median(p);

            % Get the median for each pixel through hundred frames
and finf the
            % correction map
                 M_P=median(My_F_Step_2,3);
                F_CM= M_P / M_D;

             % Do the flat field
             for j=1:size(My_F_Step_2,3);
                F_N(:,:,j) = My_F_Step_2(:,:,j)./F_CM(:,:,:);
            end

            J2 = F_N;
    My_F_Step_3 = My_F(513:768,:,:); % The THIRD 256 x 256 x
energy levels
                          q=median(median(My_F_Step_3));
            p=q(:);
            M_D=median(p);
```

```
            % Get the median for each pixel through hundred frames
and finf the
            % correction map
                 M_P=median(My_F_Step_3,3);
                F_CM= M_P / M_D;

            % Do the flat field
             for j=1:size(My_F_Step_3,3);
                F_N(:,:,j) = My_F_Step_3(:,:,j)./F_CM(:,:,:);
            end

            J3 = F_N;

          J = [J1;J2;J3];
           save J J
end

%XXXXXXXXXXXXXXXXXXXXXXXXXXXXXXXXXXXXXXXXXXXXXXXXXXXXXXXXXXXXXXXXX%
% Flatfield correction (Anas Sedayo)
%XXXXXXXXXXXXXXXXXXXXXXXXXXXXXXXXXXXXXXXXXXXXXXXXXXXXXXXXXXXXXXXXX%


%% convert the flat field image to counts values
for energy = 1:size(F,3);
       F_counts (:,:,energy)=F(:,:,energy).*
parameters.time(energy,:);
end

L = J; % F_counts;
save L L
%  CALL TESTING_POLYFIT
testing_Polyfit
load Y2;
CF_xray= Y2;

load('parameters.mat');
load('scanner.mat');
%load('flatfield.mat');

scanner.paths.base = pwd;
scanner.paths.data = pwd;

success=1;

% find correction factor for X-ray source

% % % A = 28;
% for i = 1:256;%% to plot the flat field befroe and after the
correction factor
% % % % plot(F(A:256:768,A,1)) % Befor eapplying the correction
% % % % hold on;
F = L./CF_xray; %Devid the flat field by the correction factor
% % % % plot(new(A:256:768,A,1)) %Plot the flat field after
correction
% end
```

```
% % % new=F./CF_xray; %Devid the flat field by the correction
factor
% % % % flatfield.F_new = F;
% % % % save flatfield flatfield
% =============== End ApplyFF ======================%

%             Start Stitch                            %

                crop=[0 0 4 16]; %top bottom left right

datapath      =   fullfile(scanner.paths.data,parameters.name);
windows       =   size(parameters.THL,1); % number of energy
windows
stops         =   parameters.stops;
projections   =   parameters.projections;
sensor_pixels =
parameters.scanner.pixelman.mpxInfo.sensor_pixels;
time          =   parameters.time;
overlap       =   parameters.overlap;
%% Files locations and names
FF_dir    = '2_post_FF'; %input dir
FF_file   = 'post_FF_%03d.mat'; %output dir
stitch_dir = '3_stitched';
stitch_file = 'stitched_%03d.mat';


%% Specify any truncation of the data in the Z-axis
% % % % % % % % % % % % % % % % % % % % % % % % % % % % % % % % % % if nargin <3
% % % % % % % % % % % % % % % % % % % % % % % % % % % % % % % % % %   crop=[0 0 0
0];
% % % % % % % % % % % % % % % % % % % % % % % % % % % % % % % % % % end

%% Ensure directories exists
warning off MATLAB:MKDIR:DirectoryExists
mkdir(datapath);
mkdir(datapath,stitch_dir);
warning on MATLAB:MKDIR:DirectoryExists

%% Process each projection one at a time
%
%   1) stitch

for i = 1:projections% loop over all projections
    infile  = fullfile(datapath,FF_dir,sprintf(FF_file,i)); %
where to load for each projection
    outfile =
fullfile(datapath,stitch_dir,sprintf(stitch_file,i));    % Where
to save for each proejction
    fprintf('Producing file: %s   ',sprintf(stitch_file,i));

    if exist(outfile,'file') % else it will say already processed
if ifle exists
      fprintf(' ...already processed\n'); % if the file already
exists
    else
```

```
        S = load(infile); % load structure with I the projeciton
in it and some other vars
        J=S.J; rot=S.rot;

        %% FIX DEAD ROWS
        % make dead row row1 interpolated unless first row (no row
above to
        % compare)
        J(1,:,:) = J(2,:,:); % first row of first frame = copy
data from second row
        %J(257:256:size(J,1),:,:) = (J(190:256:size(J,1)-
100,:,:)+J(258:256:size(J,1),:,:))/2; % interp first row of other
frames
        J(257:256:size(J,1),:,:) = J(258:256:size(J,1),:,:);
        % interpolate over dead row 20 by mkaing it the average of
rows 19 and
        % 21
        J(20:256:size(J,1),:,:) = (J(19:256:size(J,1),:,:) +
J(21:256:size(J,1),:,:))/2;

        % interpolate over dead row 161 by mkaing it the average
of rows 19 and
        % 21
        J(161:256:size(J,1),:,:) = (J(160:256:size(J,1),:,:) +
J(162:256:size(J,1),:,:))/2;

        %% stitch
        rows=(sensor_pixels * stops) - ((stops-1) * overlap);
%rows in stitched image
        K = zeros(rows, size(J,2), size(J,3) )  ; % allocate some
memory

        %top and bottom dont change
        K(1:overlap,:,:) = J(1:overlap,:,:);
        K((end-overlap+1):end,:,:) =  J((end-overlap+1):end,:,:);

        %non overlapping parts don't change
        for frame=1:stops
          source_rows      = ((overlap+1) : (sensor_pixels-
overlap)) + (frame-1)*sensor_pixels;
          destination_rows = ((overlap+1) : (sensor_pixels-
overlap)) + (frame-1)*(sensor_pixels-overlap);
          K(destination_rows,:,:)=  J(source_rows,:,:) ;
        end

        %find the overlap parts and blend accross
        if stops > 1
          for frame=1:(stops-1)
            stop = frame;
            topframe_rows    = ((sensor_pixels-
overlap+1):sensor_pixels) + ((frame-1)*sensor_pixels); % bad data
            bottomframe_rows = (1:overlap) +
(frame*sensor_pixels); % good data
            destination_rows = (1:overlap) +
(frame*(sensor_pixels-overlap));

            %top_slab = J(topframe_rows,:,:); %bad
```

```
            top_line = J(sensor_pixels-overlap+(frame-
1)*sensor_pixels,:,:);
            top_good = isfinite(top_line);

            bottom_line = J(1+frame*sensor_pixels,:,:);
            bottom_good = isfinite(bottom_line);

            for energy = 1:size(J,3)
              top_median = median(top_line(top_good(:,:,energy)));
              %top_std = std(top_line(top_good));
              bottom_median =
median(bottom_line(bottom_good(:,:,energy)));
              %bottom_std = std(bottom_line(bottom_good));

              %top_bad = (top_line >= top_mean + 0.01 * top_std) |
(top_line <= top_mean - 0.01 * top_std) | ~isfinite(top_line);
              %top_mean = mean (top_line(~top_bad))

              bottom_slab  = J(bottomframe_rows,:,:); %good

              L=length(destination_rows);
              for i=1:L
                prop= i/L; %relative contribution of each for this
row.
                dest_slab(i,:,energy) = bottom_slab(i,:,energy) -
bottom_slab(i,:,energy) ...
                    *(1-top_median/bottom_median)*(1-prop);
              end

            end

%             dest_slab(top_bad) = bottom_slab(top_bad); %if we
have a bad pixel in the top, use the bottom data
%             dest_slab(bottom_bad) = top_slab(bottom_bad);

            K(destination_rows,:,:) = dest_slab;

          end
        end

        %% truncate, it speeds up processing ot get rid of it now
        Kcrop=K( (1+crop(1)):(end-crop(2)),  (1+crop(3)):(end-
crop(4)), :);
        K=Kcrop;

        % * Subtract energy bins* % Note last bin in not
subtracted
        % subtract energy lower threholds to get energy bins.
        % MikeC COMMENT OR DELETE if you dont want your
projections binned!
%         K(:,:,1:(size(K,3)-1))=K(:,:,1:(size(K,3)-1))-
K(:,:,2:(size(K,3)));

        % save matlab file
        save(outfile,'K','rot');
        fprintf(' ...done\n');
```

```
    end
end

%%%%%%%%%%% ==========     END Stitch     %%%%%%%%%% ==========
%


%%%%%%%%%%% ===== Start of interpolate bad pixels fillbad
====%%%%%%%%
%% Files locations and names
stitch_dir   = '3_stitched';
stitch_file  = 'stitched_%03d.mat';
filled_dir   = '4_interpolated';
filled_file  = 'interpolated_%03d.mat';

%% Ensure directories exists
warning off MATLAB:MKDIR:DirectoryExists
mkdir(datapath);
mkdir(datapath,filled_dir);
warning on MATLAB:MKDIR:DirectoryExists

%% Process each projection one at a time
%
%   1) interpolate

for i = 1:projections % loop over all projections
    infile  =
fullfile(datapath,stitch_dir,sprintf(stitch_file,i)); % where to
load for each projection
    outfile =
fullfile(datapath,filled_dir,sprintf(filled_file,i));    % Where
to save for each proejction
    fprintf('Producing file: %s   ',sprintf(filled_file,i));

    if exist(outfile,'file') % else it will say already processed
if ifle exists
      fprintf(' ...already processed\n'); % if the file already
exists
    else

        S = load(infile); % load structure with I the projeciton
in it and some other vars
        K=S.K; rot=S.rot;


        % loops through energy bins interpolating the bad pixels.
        for energy = 1: size(K,3)
            %sprintf('energy = %d' , energy)
            F=K(:,:,energy);

            % mask NaNs and replace them with medians of
surrounding pixels
            N = zeros(size(F)); N = ~isfinite(F);  %N=true for bad
pixels
            F(N) = 0;
```

```
            N = logical(N + logical(F < 0));
            F(N) = 0;
            Mf = image_fillmissing_make_fast(N); % locations of
masked pixels
            masked_pixels = size(Mf,1);
            F_fixed = image_fillmissing_Median(F, Mf, 0);

            % specify # st devs allowed for each region (R =
resin, S = sample)
            std_allowed_R = 3;
            std_allowed_S = 3;

%% Find mean and std.
% Data from open beam are ignored when calculating statistics for
resin and
% sample regions. Sum across colums are calculated for each row.
% Edges of resin and sample are identified as the rows that have
75%
% and 45% of the count from open beam, respectively. These can
(should?) be
% changed for different samples.

            % mask unsensible values
            sum_col = sum(F,2);          %sum across columns
            a = logical(F < min(sum_col));
            F(~a) = 0;

            sum_col_F = sum(F,2);
%            figure; plot(sum_col_F); mean(sum_col_F(1:20)) %
uncomment to see plot and mean (for determining edges of resin and
sample)
            b = logical(sum_col <= 0.2*mean(sum_col_F(1:100)));  %
define edges of resin here
            edge_R1 = find(b == 1,1,'first');
            edge_R2 = find(b == 1,1,'last');
            R = F(edge_R1:edge_R2,:);                % resin region

            center_R = median(R(:));
            dist_R   = std(R(:));
            top_R    = center_R + dist_R * std_allowed_R;
            bottom_R = center_R - dist_R * std_allowed_R;


            sum_col_R = sum(R,2);
%              figure; plot(sum_col_R);
            c = logical(sum_col_R <= 0.1*mean(sum_col_F(1:100)));
% define edges of sample here
            edge_S1 = find(c == 1,1,'first') + edge_R1;
            edge_S2 = edge_R2;
            %edge_S2 = find(c == 1,1,'last') + edge_R1;
            S = F(edge_S1:edge_S2,:);                          %
sample region

            center_S = median(S(:));
            dist_S   = std(S(:));
            top_S    = center_S + dist_S * std_allowed_S;
            bottom_S = center_S - dist_S * std_allowed_S;
```

```
%% Mask & interpolate
            while masked_pixels >= 10;

                % mask out-of-range pixels
                M_new = make_mask_std
(F_fixed,top_R,bottom_R,top_S,bottom_S,edge_R1,edge_R2,edge_S1,edg
e_S2,parameters);
                M_F = (F_fixed == 0);

                M = M_F + M_new; M = logical (M >=1);

                F = F_fixed; F(M) = 0;
% update image
                Mf_new = image_fillmissing_make_fast(M); Mf =
Mf_new;  % update mask
                F_fixed = image_fillmissing_Median(F, Mf, 0);
                masked_pixels_new = size(Mf_new,1);
% number of pixels masked

                if abs(masked_pixels_new - masked_pixels) >= 3;
                    F_fixed = image_fillmissing_Median(F, Mf, 1);
                    masked_pixels_new = size(Mf_new,1);
                end

                if masked_pixels_new == masked_pixels;
                    break
                end

                masked_pixels = masked_pixels_new;


            end
            fprintf('.');

            % update mask before passing it to denoise
            M = make_mask_std
(F_fixed,top_R,bottom_R,top_S,bottom_S,edge_R1,edge_R2,edge_S1,edg
e_S2,parameters);


           %fprintf('.');
           L(:,:,energy)=F_fixed;
           bad_pixels_mask(:,:,energy)= M;
        end

        % save matlab file
        save(outfile,'L','rot','bad_pixels_mask');
        fprintf(' done\n');


    end
end

success = true;
```

```
%%%%  END of FILLBED & Start of remove salt-n-pepper noise denoise
%%%%

crop=[0 0 0 0];
max_value=[1 1 1 1 1 1 1 1]*(0.3*10^5);

%% Get all the scan constants
    % paths come from the scanner structure. ie the local
environment
    % every thing else comes from parameters or
parameters.scanner. ie How
    % the data was actuall acquired.
% % % % % datapath        =
fullfile(scanner.paths.data,parameters.name);
% % % % % stops           =   parameters.stops;
% % % % % projections     =   parameters.projections;
% % % % % windows         =   size(parameters.THL,1);

%% Files locations and names
denoise_dir   = '5_denoise';
denoise_file  = 'denoise_%03d.mat';
export_dir    = '6_tiffs';
export_subdir = 'energy_%03d';
export_file   = 'tiff_%03d.tif';

%% Ensure directories exists
warning off MATLAB:MKDIR:DirectoryExists
mkdir(datapath);
mkdir(datapath,export_dir);
for i=1:windows
    mkdir(fullfile(datapath,export_dir),sprintf(export_subdir,i));
end
warning on MATLAB:MKDIR:DirectoryExists



%% Process each projection one at a time
%
%   1) export tiff

for i = 1:projections % loop over all projections

    infile =
fullfile(datapath,denoise_dir,sprintf(denoise_file,i));    % where
to load each data
    fprintf('Producing tiff files from: %s
',sprintf(denoise_file,i));

    S = load(infile); % load structure with I the projeciton in it
and some other vars
    L=S.N; rot=S.rot;


    %% loops through energy bins interpolating the bad pixels.
    for energy = 1:size(L,3) %loop over energy bins
```

```
outfile=fullfile(datapath,export_dir,sprintf(export_subdir,energy)
,sprintf(export_file,i));
        if exist(outfile,'file')
            fprintf('*')
            continue
        end

        %get just one energy
        I=L(:,:,energy);

        %crop
        I=I( (1+crop(1)):(end-crop(2)),  (1+crop(3)):(end-
crop(4)), :);

        %scale
        I=I/ max_value(energy) * 2^16 ; %scale 0-> 2^16;

        %write the file
        imwrite(uint16(I'),outfile,'TIFF','Compression','none');
%write a 16 bit tif.

        fprintf('.');
    end
    fprintf(' done\n');
end

success = true;
```

APPENDIX C: Matlab code for finding ROI and plot Hounsfield Unit (HU)

```
%%This code can be use to analyse the images by finding the RIO
for defferent region
%%on the image to define the number of voxel accociated with it
and then calculating the mean,
%%standard deviation, Hounsfield unit and plot the error bar.

%%code modefied by: Anas Sedayo
%%Written date:19-03-2010

%%Modefied date:24-03-2010, (I have managed to plot the error
using the standard
%%deviation as the percentage error of the mean of the each
parameters (Fat, Liver, Air and Water).

clear
home
close

% %which cross sectional image are we studying?, select the image
number
% you would like to study.
image=018;

% %Scanning time (The scanning time can be found from the protocol
data file)

sct = [2.0,1.0,0.6 ]; %2009_10_21_Liver_Fat_Paper
% % sct =
[0.033,0.0434,0.0554,0.0755,0.104,0.146,0.21,0.29,0.392,0.57,0.804
,1.010]; %2009_10_21_Liver_Fat_Paper

% The energy range can be selected depending on the energy range
used in the images

THL = [530;577;625];  %2009_10_21_Liver_Fat_Paper
Energy = [22;15;08];
% % THL = [465;490;515;540;565;590;615;640;665;690;715;740];
%2009_10_21_Liver_Fat_Paper

energies = 3;  %number of energy can be change based on the number
of energy used

%load all the energies
infiles(1).name='C:\\aas44_Ddrive_UC_PHYS_215\\2009_10_21_Liver_Fa
t_Paper\\6_tiffs\\530\\reconstructed\\tiff_%03d.tif';  %
2009_10_21_Liver_Fat_Paper
infiles(2).name='C:\\aas44_Ddrive_UC_PHYS_215\\2009_10_21_Liver_Fa
t_Paper\\6_tiffs\\577\\reconstructed\\tiff_%03d.tif';
infiles(3).name='C:\\aas44_Ddrive_UC_PHYS_215\\2009_10_21_Liver_Fa
t_Paper\\6_tiffs\\625\\reconstructed\\tiff_%03d.tif';
```

```
for j=1:energies
    file=sprintf(infiles(j).name,image); %transfere the image from
the character to double.
    I(:,:,j)=double(imread(file))/255;   %65535
end

% %Identify fat region (allow the user to select the ROI and
export the data)

fprintf('Please select ROI for FAT and hit return\n\n\n')
FAT   = roipoly(I(:,:,1));
pause
close


% % Identify liver region (allow the user to select the ROI and
export the data)
fprintf('Please select ROI for Liver and hit return\n\n\n')
Liver = roipoly(I(:,:,1));
pause
close


% %Identify air region(allow the user to select the ROI and export
the data)
fprintf('Please select ROI for air and hit return\n\n\n')
Air   = roipoly(I(:,:,1));
pause
close

% %Identify water region(allow the user to select the ROI and
export the data)
fprintf('Please select ROI for water and hit return\n\n\n')
Water = roipoly(I(:,:,1));
pause
close


% %example of finding the actual parts been selected


% figure(1)
% imshow(FAT .* I(:,:,1)); % to plot the selected ROI

% figure(2)
% imshow(Liver .* I(:,:,1)); % to plot the selected ROI

% figure(3)
% imshow(Air .* I(:,:,1)); % to plot the selected ROI

% figure(4)
% imshow(Water .* I(:,:,1)); % to plot the selected ROI
```

```
% %identify the voxels values for selected ROI

for i=1:energies
 FAT_image          = I(:,:,i);
%  %Changing I(:,:,:)from a square matrix (492x492) to an array
(getting rid
%  %of zeros using the logic FAT matrix, the code also used to
find the
%  %mean of the selected ROI.

 FAT_voxels(:,i)    = FAT_image(FAT);
 FAT_mean(i)        = mean(FAT_voxels(:,i));
 FAT_std(i)        = std(FAT_voxels(:,i));

 Liver_image        = I(:,:,i);
 Liver_voxels(:,i) = Liver_image(Liver);
 Liver_mean(i)      = mean(Liver_voxels(:,i));

 Air_image          = I(:,:,i);
 Air_voxels(:,i)    = Air_image(Air);
 Air_mean(i)        = mean(Air_voxels(:,i));

 Water_image        = I(:,:,i);
 Water_voxels(:,i) = Water_image(Water);
 Water_mean(i)      = mean(Water_voxels(:,i));
end


% % To find the total number of voxel for ROI

% FAT_num_voxel=size(FAT_voxels,1)

% Liver_num_voxel=size(Liver_voxels,1)

% Air_num_voxel=size(Air_voxels,1)

% Water_num_voxel=size(Water_voxels,1)


% %plot the mean of the FAT(ROI) virsus the energy (THL)


% figure(10)
% plot(THL,FAT_mean,THL,Liver_mean,THL,Air_mean,THL,Water_mean);
% legend('FAT','Liver','Air','Water')
% title('THL vs mean')
% xlabel('THL')
% ylabel('Composition')
% grid on

% % To calculate the HU for Fat and Liver
HU_FAT   = ((FAT_mean-Water_mean)./(Water_mean-Air_mean))*1000;
HU_Liver = ((Liver_mean-Water_mean)./(Water_mean-Air_mean))*1000;
HU_Water = ((Water_mean-Water_mean)./(Water_mean-Air_mean))*1000;
```

```
HU_Air = ((Air_mean-Water_mean)./(Water_mean-Air_mean))*1000;


% %plot the HU vs the energy(THL)

% figure(11)
% plot(THL,HU_FAT,THL,HU_Liver,THL,HU_Air,THL,HU_Water);
% %%errorbar (
% legend('FAT','Liver','Air','Water')
% title('THL vs HU')
% xlabel('THL')
% ylabel('HU')
% grid on

%% to plot the mean and the HU in the same figure
% figure(4)
% subplot(1,2,1)
% plot(THL,FAT_mean,THL,Liver_mean,THL,Air_mean,THL,Water_mean);
% legend('FAT','Liver','Air','Water')
% title('THL vs mean')
% xlabel('THL')
% ylabel('Composition')
% grid on
% % To calculate the HU for FAt
% HU_FAT   = ((FAT_mean-Water_mean)./(Water_mean-Air_mean))*1000;
% HU_Liver = ((Liver_mean-Water_mean)./(Water_mean-
Air_mean))*1000;
%
% %plot the HU vs the energy
% subplot(1,2,2)
% plot(THL,HU_FAT,THL,HU_Liver);
% legend('FAT','Liver')
% title('THL vs HU')
% xlabel('THL')
% ylabel('HU')
% grid on

% plot(THL,FAT_mean);
%
% figure(3)
% % subplot(2,2,1)
% plot(THL,Liver_mean);
%
% figure(4)
% % subplot(2,2,1)
% plot(THL,Air_mean);
%
% figure(5)
% % subplot(2,2,1)
% plot(THL,Water_mean);


% %to calculate the standard division

for i = 1:energies
    FAT_image         = I(:,:,i);
    FAT_voxels(:,i)   = FAT_image(FAT);
```

```
    FAT_std(i)        = std(FAT_voxels(:,i));

    Liver_image       = I(:,:,i);
    Liver_voxels(:,i) = Liver_image(Liver);
    Liver_std(i)      = std(Liver_voxels(:,i));

    Air_image         = I(:,:,i);
    Air_voxels(:,i)   = Air_image(Air);
    Air_std(i)        = std(Air_voxels(:,i));

    Water_image       = I(:,:,i);
    Water_voxels(:,i) = Water_image(Water);
    Water_std(i)      = std(Water_voxels(:,i));
end

% % HU1_FAT_plusE   = ((FAT_mean+SE_FAT_mean-
Water_mean)./(Water_mean-Air_mean))*1000;
% % HU1_SE_FAT   = HU1_FAT_plusE-HU1_FAT;
% % errorbar(THL',HU_FAT,std(HU_FAT))


% %plot the Standard deviation

% figure(12)
% plot(THL,FAT_std,THL,Liver_std,THL,Air_std,THL,Water_std);
% legend('FAT','Liver','Air','Water')
% title('THL vs std')
% xlabel('THL')
% ylabel('std')
% grid on

% %calculate the scanning aqusetion time for the mean
(sc.mean=mean/sct)

scan_mean_FAT = FAT_mean./sct;
scan_mean_Liver = Liver_mean./sct;
scan_mean_Air = Air_mean./sct;
scan_mean_Water = Water_mean./sct;

scan_std_Fat=FAT_std./sct;
scan_std_Liver=Liver_std./sct;
scan_std_Air=Air_std./sct;
scan_std_Water=Water_std./sct;
sz=size(FAT_voxels(:,1))
N=sz(1)
scan_se_FAT=scan_std_Fat/sqrt(N)
HU1_FAT_plusE   = ((scan_mean_FAT+scan_se_FAT-
scan_mean_Water)./(scan_mean_Water-scan_mean_Air))*1000;
HU1_SE_FAT   = HU1_FAT_plusE-HU_FAT;

scan_se_Liver=scan_std_Liver/sqrt(N)
HU1_Liver_plusE   = ((scan_mean_Liver+scan_se_Liver-
scan_mean_Water)./(scan_mean_Water-scan_mean_Air))*1000;
HU1_SE_Liver   = HU1_Liver_plusE-HU_Liver;

scan_se_Air=scan_std_Air/sqrt(N)
```

```
HU1_Air_plusE   = ((scan_mean_Air+scan_se_Air-
scan_mean_Water)./(scan_mean_Water-scan_mean_Air))*1000;
HU1_SE_Air   = HU1_Air_plusE-HU_Air;

scan_se_Water=scan_std_Water/sqrt(N)
HU1_Water_plusE   = ((scan_mean_Water+scan_se_Water-
scan_mean_Water)./(scan_mean_Water-scan_mean_Air))*1000;
HU1_SE_Water   = HU1_Water_plusE-HU_Water


% %plot the Sc_mean
% figure(13)
% plot(THL,scan_mean_FAT,...
%      THL,scan_mean_Liver,...
%      THL,scan_mean_Air,...
%      THL,scan_mean_Water);
% legend('FAT','Liver','Air','Water')
% title('THL vs sct_mean')
% xlabel('THL')
% ylabel('sct_mean')
% grid on

% %calculate the scan standard deviation (sc_std=std/sct)

scan_std_FAT   = FAT_std./sct;
scan_std_Liver = Liver_std./sct;
scan_std_Air   = Air_std./sct;
scan_std_Water = Water_std./sct;

% %plot the Sc.std

% figure(14)
% plot(THL,scan_std_FAT,...
%      THL,scan_std_Liver,...
%      THL,scan_std_Air,...
%      THL,scan_std_Water);
% legend('FAT','Liver','Air','Water')
% title('THL vs sc_std')
% xlabel('THL')
% ylabel('sc_std')
% grid on


%% plot the errorbar using the stndard deviation as the percentage
error of the mean

figure(15)

% errorbar(THL,FAT_mean,FAT_std);
% errorbar(THL,HU_FAT,HU1_SE_FAT);
errorbar(Energy,HU_FAT,HU1_SE_FAT);



hold on
```

```
% % errorbar(THL,Liver_mean,Liver_std,'r');
% errorbar(THL,HU_Liver,HU1_SE_Liver,'r');
errorbar(Energy,HU_Liver,HU1_SE_Liver,'r');

hold off

hold on

% % % errorbar(THL,Air_mean,Air_std,'g');
% errorbar(THL,HU_Air,HU1_SE_Air,'g');
errorbar(Energy,HU_Air,HU1_SE_Air,'g');



hold off

hold on

% % errorbar(THL,Water_mean,Water_std,'k');
% errorbar(THL,HU_Water,HU1_SE_Water,'k');
errorbar(Energy,HU_Water,HU1_SE_Water,'k');

hold off

legend('Fat','Liver','Air','Water')
% title('THL vs mean, error(std)')
xlabel('Energy (keV)')
% % ylabel('Mean')
ylabel('Attenuation (HU)')


grid on

figure(16)
% plot(THL,HU1_SE_FAT);
plot(Energy,HU1_SE_FAT);

hold off

hold on

% plot(THL,HU1_SE_Liver,'r');
plot(Energy,HU1_SE_Liver,'r');

hold off

hold on

% plot(THL,HU1_SE_Air,'g');
plot(Energy,HU1_SE_Air,'g');

hold off

hold on
```

```
% plot(THL,HU1_SE_Water,'k');
plot(Energy,HU1_SE_Water,'k');


hold off

legend('Fat','Liver','Air','Water')
% title('THL vs s.e. of the mean, error(std)')
% xlabel('THL')
xlabel('Energy (keV)')
% % ylabel('Mean')
ylabel('S.E. of the mean (HU)')
YLim([0 4])

% colorbar
```